A Fault-tolerant Triple Three-Phase Induction Machine

Fangbo Liu

B.Eng., MSc.

A thesis submitted for the degree of

Doctor of Philosophy

October 2019

School of Engineering

Newcastle University

Abstract

This thesis focuses on the development of a fault tolerant induction motor which is capable of continued operation with winding and power converter short-circuits. The motor takes advantage of a segmented stator to function under extreme circumstance. When splitting a motor stator into separate segments of power, there is still coupling between segments, which is minimised by partitioning the motor into a series of circumferentially separated arcs. In this way, each segment of the stator is electrically, thermally, physically independent and each arc can be viewed as a linear motor; however, it has been found that the motor cannot be functional as a normal motor at all speeds. The reason of that phenomenon will be studied and concluded to be the large asynchronous space harmonics produced by each arc, which prevents the system from functioning successfully. According to the reason, a modified rotor is introduced which overcomes this problem and allows operation with not only open circuit, but also in short circuits for what is believed to be the first time.

Keywords— Fault tolerant, induction machine, harmonic elimination, segmented stator

Acknowledgment

Studying for a Ph.D. degree is like sailing a boat into an uncharted sea, there will be storms and billows but occasionally there are beautiful sceneries. During a hard time, I received great help from the people around me. I would like to show my deepest gratitude to my supervisors, Professor Barrie Mecrow and Dr. Kristofer Smith without their help I probably have already been swallowed by the ruthless sea. Their efforts, patient, support, and guidance help me to find out the path and hold on to the truth. It's them that makes today's achievement possible.

Besides that, I like to say thank you to Dr. Yang Lu for his help when I first start my Ph.D. I was lost and unfamiliar with everything, he helps me not just in the academic field but in life and being my friend. I also like to show my appreciation to Dr. Richard Martin, Dr. Sichao Yang. They selflessly shared their scripts with me, which saves me a lot of time in creating the conventional induction motor and study the behavior of the rotor. I would like to show my gratitude to Dr. Haimeng Wu and Dr. Xu Deng. They are not my supervisors but relentlessly share their insights and help me in whatever situations. I also like to say thank you to Dr. Bernardo Alveranga for his previous work in the induction machine, and Professor Alexander C. Smith for his help in commenting on my work.

I am also grateful to Chris Manning, James Richardson, Gorden Marshall, and all the technicians and mechanics in the workshop and UG lab. For their help in assembling the motor and test rig.

I would like to express my gratitude to the people I met in my daily life, my church friends, my flatmates, and my colleagues in the UG lab for a wonderful life experience with them.

In the end, I like to say thank you to my parents. It's them that encourage me to pursue a Ph.D. degree. It's also them that support me emotionally and financially. A simple 'thank you' can not even express a thousandth of my gratitude. I can only hope that you are proud of me which is the start of the 'thank you' I need to say for the rest of my life.

Content

Content

Content

Content

List of Tables

List of Figures

CHAPTER 4

List of Figures

List of Acronyms and Symbols

List of Symbols

X_1	Stator inductance
R_1	Stator resistance
R_2	Rotor resistance referred to the stator side
X_2	Rotor inductance referred to the stator side
Z_M	The mutual inductance between the rotor and stator
s	Slip
P_t	Power transferred across the air gap
P_m	Mechanical power
T	Electromagnetic torque
m_1	Number of stator phases
I_2	Branch current in the rotor
I_1	Current in the stator
P_R	Total rotor loss
$MMF_{original}$	MMF under the healthy condition
N	The number of the conductor in the slots
θ	The electrical displacement between the slots
I_p	The magnitude of the eight-phase current under the fault condition
r_p	The circle perimeter of all middle points of slots
r_r	The radius of the rotor
r_{AG}	Air gap length
H_S	The height of the slot
R	The resistance of the conductive material
ρ	The resistivity of the material
S	The cross-sectional area
L	The length of the material
X_l	The end winding leakage reactance
f_1	The stator voltage frequency
N_1	The number of series connected conductors per phase
p	The number of pole pair

List of Acronyms and Symbols

I_E, l_w	The average length of the end winding
τ	The stator coil pitch
Q	The number of slots
a	The number of the paralleled path
q	The number of slot per phase per pole
μ_0	The vacuum permeability
λ_w	The permeance factor
$\hat{I}$	The peak value of the current
k_p	The pitch factor
k_d	The distribution factor
P	The number of pole pair
r	The rotor radius
$\hat{H}$	The peak value of the magnet field strength
$\hat{I}$	The peak current in the stator winding at rated condition
L_s	The stack length
α	The skew angle of the whole machine
ω	The synchronous speed
P_{in}	The power input the stator
m_r	The phase number of the rotor
b	The number of space harmonic
$|Z_k|$	The absolute value of the total impedance in the equivalent circuit
R_k	The total resistance in the equivalent circuit
N_r	The number of coils per phase of the rotor
k_{ws}	The winding factor of the stator
k_{wr}	The winding factor of the rotor

List of Acronyms and Symbols

List of Acronyms

MIM	Multiphase Induction Machine
PMSM	Permanent Magnet Synchronous Machine
FEA	Finite Element Analysis
UPS	Uninterrupted Power Supply
PM	Permanent Magnet
EMF	Electromagnetic Force
MMF	Magnetomotive Force
2-D	Two dimensions
SRM	Switch Reluctance Machine
RMS	Root Mean Square
IEEE	Institution of Electrical and Electronic Engineering
MATLAB	Matrix Laboratory

List of Acronyms

Chapter 1 Introduction

This thesis presents the triple three-phase segmented induction machine which was researched and constructed during the doctoral degree of the author. In this chapter, the motivation and objectives for developing the induction machine are demonstrated. The induction machine's novelty and publications based on its development will be presented to show the contribution to knowledge. To offer an integral understanding of the thesis, its structure and content will be described in the last part of this chapter.

1.1 Motivations and objectives

As one of the most common types of electrical machines, induction machines have been serving humanity for almost two centuries. The advantages include high reliability (physically), high-cost efficiency, a simple control structure, and high torque at low speed. In addition, they are widely used in industry and the marine business. The limitations are also obvious: relatively low efficiency and electrical reliability. As a result, Newcastle University proposed a new type of induction machine which is a triple three-phase segmented induction machine. This machine utilizes the redundancy of two extra sets of three-phase machines to enhance the reliability of the stator, allowing the machine a certain level of functioning under fault conditions.

This Ph.D. thesis is dedicated to demonstrating the work for designing the triple three-phase induction machine. The objectives are:

a) To model an induction machine with higher reliability.

b) To understand the essential reason for the poorer performance of the conventional three-phase induction machine.

c) To design a stator that is physically, thermally, and electrically isolated from each part to tolerate the fault condition.

d) Based on the reason for poor performance, optimize the rotor to accomplish the fault-tolerant ability, including the open circuit and short circuit conditions.

e) To build the demonstrator for testing.

1.2 Statement of Novelty

The novelty of this thesis is arising from the design and construction of the segmented triple three-phase induction machine. Although the fault-tolerant machine is a heated topic in machine

design, this is the first time that a functional triple three-phase under open circuit and short circuit conditions has been introduced to the induction machine.

- With the help of MATLAB and FEA software, this thesis will demonstrate the method of understanding each harmonics' contribution to torque under different conditions.
- Optimized the induction machine stator to achieve fault-tolerant ability.
- Optimized the rotor to avoid side-effects when the triple three-phase induction machine operated under a fault condition.

1.3 Publication Arising from this Work

Fangbo Liu, Barrie Mecrow, Alexander C. Smith, B. Alvarenga, and Xu Deng, "A Fault-Tolerant Induction Motor Drive," in The Eleventh Annual Energy Conversion Congress and Exposition of the IEEE, accepted.

1.4 Thesis overview

An outline of the thesis has been presented here.

➢ **Chapter 1 and 2 The Introduction and Literature Review**

These two chapters cover the basics and the context of the thesis. In Chapter 1, the objectives, the contribution to knowledge, and the publication arising from this work will be introduced. The literature review covers the development of the multi-phase induction machine. Besides that, the advantages for the applications in the aerospace and marine field will also be included. Furthermore, some basic principles of the induction machine and the fault types will be discussed as well.

➢ **Chapter 3 Conventional Cage Rotor Three-phase Induction Machine Design**

In Chapter 3, the conventional induction machine with a standard cage rotor will be designed, and the simulation was made according to an existing motor. The simulation conditions and parameters of the motor will be shown in this chapter. In this chapter, the simulation is using a finite element analysis (FEA) software called MagNet. The winding configuration of the stator will be discussed and the simulation results will be compared with the manufacturing data to confirm the accuracy of the model. This chapter will also discuss the methods to obtain the value of the end winding resistance and inductance leakage to set the baseline for further study.

➢ **Chapter 4 Triple Three-phase Induction Machine**

Chapter 1 Introduction

This chapter will focus on the performance of the triple three-phase induction machine and optimization. It will start with the basic model of the triple three-phase induction motor with a cage rotor, including the winding configuration, the slot geometry, and the principle of a multi-phase induction machine. By obtaining the torque-slip curve from the simulation, a series of steps of optimization will be done. However, before the optimization, the phenomenon has to be studied and understood, which will be included in this chapter as well. To further improve the performance of the motor a new rotor will be proposed, and the detail of the new rotor will be enclosed in this chapter as well. At the end of the chapter, the performance of the proposed motor under different conditions including the open circuit, short circuit, and healthy condition will be compared with the performance without optimization and come to the conclusion that the optimization improves the performance and enhances reliability.

➢ **Chapter 5 The Prototype Establishment**

In this chapter, more attention will be paid to machine manufacturing and test rig assembly. This chapter will start with stator and rotor manufacturing. The 3D model and the casting model will be shown in this part. It will also include the techniques for manufacturing the stator and rotor. Then, it will follow with winding configurations of the stator and rotor and by assembling them, the motor is complete. The next part discusses the detail of the components of a test rig. The function of each part of the test rig will be demonstrated and the operation methods will be also discussed.

➢ **Chapter 6 Experimental Test Results**

In this chapter, the simulation results obtained in the previous chapters including the healthy condition and short circuit condition are verified. By comparing the results, it shows the fundamental principle of the previous simulation will be proved to be correct. The locked rotor and no-load test will be carried out to calculate the parameters of the single-phase induction machine equivalent circuit. In the same chapter, the torque slip curve prediction according to the equivalent circuit will be presented as well. The simulation results, the equivalent circuit prediction, and the test results will be compared together to illustrate the accuracy of the simulation.

➢ **Chapter 7 Conclusion and Future Work**

This chapter gives the conclusion of the contribution to the knowledge of the entire thesis, and recommendations of future work to further improve the fault-tolerant induction machine.

Chapter 2 Literature Review

2.0 Introduction

Currently, the induction machine is the most common electrical machine used in industry. Low cost, high reliability and robustness, maintenance-free operation, and excellent torque performance despite rough environments are among the many reasons it replaces the DC control system.[1] As the speed variety issue has been resolved with the development of signal processing and the converter, eliminating the primary difficulty of induction machine control, the popularity of the induction machine is increasing day by day.

2.1 History and applications of the induction machine

In recent years, as technology rapidly improved, stability became a vital problem for the electrical machine. As is the case currently, in the 1920s a small malfunction in the electrical machine may have resulted in a substantial financial loss.[2] As such, the fault-tolerant machine was first introduced in the 1920s. It was implemented, however, for an entirely different function. It was applied to improve the total power capability of the permanent magnet machine.[3] The exploration of the fault-tolerant machine has not stopped. Subsequently, the same idea was applied to the synchronous machine with both AC and DC output[4], which have a similar function of uninterrupted power supplies (UPSs).[5] In that case, a multiphase induction machine (MIM) made it possible to expend the power range based on the conventional inverter and gave the electrical machine a broad space for development.[6]

The MIM has all the merits of the induction machine, with the further advantage of providing a certain degree of fault-tolerance, providing extra security to safety-critical applications. Some studies[7-10] show that the MIM is suitable for marine applications. Those studies have shown the performance of MIM under a one-phase open circuit condition and the strategy for compensating for a single-phase open-circuited condition.

a) The advantages in efficiency, torque pulsation reduction, and enhanced reliability
Many papers have introduced the advantages of MIM. In[11], the author has tested the experimental performance of the conventional induction machine and a dual three-phase induction machine with asymmetrical winding configuration. During the experiment, it was found that motor efficiency is about 5% and 3% greater than the conventional three-phase induction machine with a 150Hz and 300Hz source. The converter efficiency is approximately 3% greater than the three-phase with a 150Hz source, while they are nearly equivalent for the

300Hz voltage source. In[12], the author utilizes a 48 stator slot motor where all the winding coils are brought out to a connection unit to achieve a 1,2,3,4,6,8, and 12 phase model. The rotor is a standard cage rotor connected to a DC motor to control the speed. The test results find that to achieve the same load, comparing to the three-phase induction machine, the 4,6,8, and 12-phase rotors produce less stator current by 0.6%, 0.7%, 0.7%, and 0.8%. In the meantime, the pulsating torque is displayed for different connections, and the author concludes that with the increasing number of phases, the pulsating torque decreases. In[13], the author has derived the general expression of the harmonics distributed in the air gap and mathematically proves that the essence of the MIM improved efficiency is due to the reduced stator copper loss. According to the same paper, the copper loss of the rotor is also believed to be smaller. The pulsating torque is less in the MIM, but at the same time, the penetration effect also causes the pulsating torque. If possible, the $2Nm \pm 1$ order harmonic shall be avoided to reduce the pulsating torque, where N is a natural number and m is the phase number.

The most apparent advantage of the MIM is enhanced reliability. In[14], the author tests the six-phase induction machine with a one-phase open circuit and finds that with one-phase loss, the power of the stator lost about 17%, however, the average torque lost is less than 10%. The author believes that the type of power source and slip are critical to explaining this phenomenon and indicates that there is great potential for MIMs.

b) Marine, automobile, and aerospace applications

Many kinds of literature have studied the possibility of utilizing the feature of the high reliability of the fault-tolerant induction machine in marine, automobile, and aerospace settings. In[15], the author reviews the development of the MIM in recent years and notes that during the fault of the one-phase open circuit condition, the currents of other healthy phases inevitably increase by a factor of $ak/(ak - 1)$, where a is the sub-phase number and k is the natural number. In this case, the semi-conductors in the converter shall withstand a higher current, which should be considered during the model of the MIM. The author also notes that the multiphase induction machine may be the answer for direct-driven applications in wind power generation. In[16], the author discussed the criteria for designing an electrical motor for aircraft; one of the essential criteria is reliability and performance under the fault operation condition. The author also proposes two types of control methods for the dual three-phase PM machine to apply to aircraft. The first method is based on the required torque and instantaneous back EMF to determine the required current and optimizing the current in the stator. The test results suggest that the torque ripple reduced significantly. The second method is focusing on the fault that occurs to the motor while the aircraft is decelerating, but one subsystem of the motor is

failing. Under this circumstance, the remaining three-phase subsystem increases the current to reach the required speed. Compared to the first method, the second method doesn't require reshaping the current because both half subsystems are providing smooth torque. As it is widely known that high efficiency, reliability, and low mass is required for a solar aircraft, in[17], the author discusses the advantages of different motors and different types of drive systems and demonstrates a novel design of drive and motor to be implemented on a solar aircraft. In this paper, by applying a large number of poles and very low loss lamination, the proposed motor pushed the world record from constantly flying 30 hours to 84 hours. In this test, a three-phase 32 pole PM machine was used for high efficiency and high torque density. Most importantly, the slot shape in the stator was formed in a semi-closed shape and verified that a semi-closed slot is the best choice for improving the torque density in the airgap.

c) The permanent magnet synchronous machine drive

Due to similarities the induction machine shares with the permanent magnet synchronous machine (PMSM), the drive for the fault-tolerant PMSM shall be studied, analyzing its advantages and disadvantages. In[18], the author has proposed a permanent magnet assisted synchronous reluctance machine. In this machine, there is a triple three-phase 36 slotted fully pitched stator, with a magnet assisted reluctance rotor. The experiment focuses on the open circuit and short circuit of a one-phase open circuit if one considers the triple three-phase machine as a nine-phase machine. Under the open circuit fault, phase A is disconnected from the power source and the torque reduces by 40%. As seen in Figure 2-1, however, the phase of all three phases of flux linkage is distorted. Due to the direct link between the flux linkage and the back EMF, it can be known that the back EMF is distorted in both the phase and amplitude, which is the most significant disadvantage for the fault-tolerant PMSM. Compared to an induction machine, under fault condition, the current increases significantly along with the less distorted back EMF due to no polarity for the cage rotor (under the voltage control method), which shows the potential to operate under fault condition.
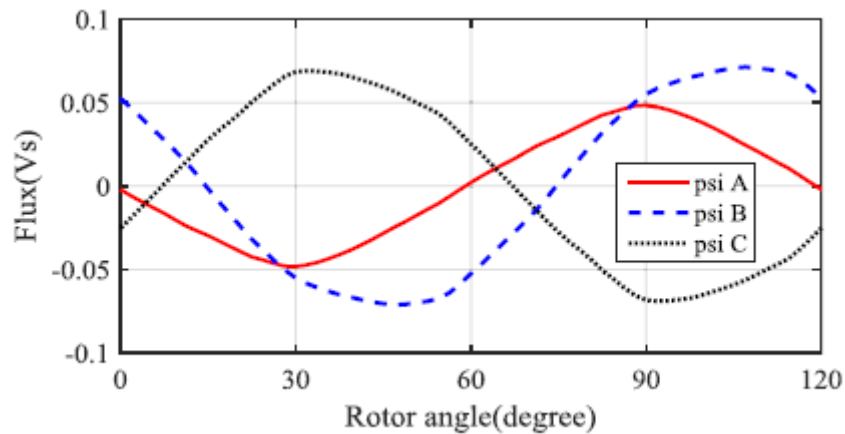
Figure 2 -1 The flux distribution under the one phase open circuit[18]

Other literature[19] raised a new model that is a five-phase PMSM motor with an outer rotor. This model shows good torque density for low-speed operation with less magnetic material. Most significantly, this paper utilized the teeth parameters to optimize the torque ripple of the proposed motor. It has been reported that the current of the proposed motor in this literature under short circuit conditions is reduced to 75% of the original. Although the literature fails to demonstrate the specifics for this one-phase short circuit condition, it can be an inter-turn short circuit and ground short circuit. However, judging from the flux density, as seen in Figure 2 - 2, the EMF is significantly reduced, as is the torque.
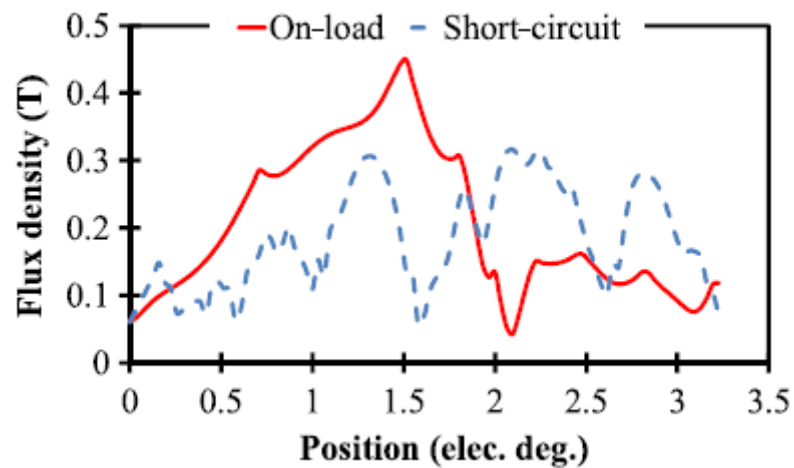
Figure 2 -2: The flux density around the rotor[19]

d) Multiphase machine study

In the previous research upon the multiphase machine, most efforts have focused on adjusting the drive system to achieve balanced operation. In[20], the author raised a new mathematical model in deriving the torque performance of a dual three-phase induction machine under a one-

phase open circuit condition. In the meantime, the author suggests two new methods of controlling the model under the fault condition. The first method is that by keeping the neutral point of the motor isolated from the source, the drive increases the current in the stator and optimizes the current to achieve the same torque standard as that in the healthy operation. In this method, it has been proved that the torque ripple has been reduced compared to the conventional control method under the same fault condition. The other is by maintaining the α and β current, which is the current component in the newly raised mathematic model and calculating the I_m. The I_α and I_β are propotional. Acording to the author, this method is simple to implement and helps to reduce the oscillation in torque and speed. In[21], the author compared two control method performances under a one-phase open circuit condition, which are field orientation control and direct torque control. The tests are operated on a six-phase induction motor. The test results suggest that the field orientation control is not able to keep the director quadrate stator current stable. On the contrary, the direct torque control manages to maintain the same current in each phase, reducing the pulsating torque by optimizing the phase current, and keeping the angular speed under the one-phase open circuit condition. In[22], the author mentioned a method to control a five-phase PM machine under the one-phase open circuit condition by maintaining the post fault MMF with the MMF in the healthy condition. This method requires no further hardware during the fault condition and achieves excellent post fault performance by compensating the operational speed and eliminating the pulsating torque. To study the performance of the motor under fault conditions, in[23], the author raised a model for calculating the dual three-phase induction machine torque under an unbalanced voltage feed. This calculation uses the vector space decomposition method. Since the stator of the motor is symmetrical and both three-phase subsystems are identical, the single-phase equivalent circuit can be used for the classic equavilant circuit. By decomposing the equivilant circuit into the positive, negative and zero sequence circuits, the performance can be predicted as a normal three-phase induction machine. The obtained result, however, is half of the motor performance and needs to be multiplied with a factor. The factor depends on the extent of voltage unbalance and the load condition. [24] has suggested a new method which applies the spectrogram and Fast Fourier transform (FFT) analysis to the stator current signal to analyze the rotor speed ripple to detect whether or not the AC machine is under the fault operation.

2.2 Fundamental principles of the induction machine

2.2.1 Typical induction machine topology

The induction machine is one of the electrical machines that does not rely on the permanent magnet, which made the induction machine the most commonly used electrical machine currently. Figure 2 -3 demonstrates the typical induction machine topologies.

Figure 2 -3 (a) demonstrates the squirrel cage rotor, which utilizes aluminum (occasionally copper) as the conductor in the rotor; both sides are short-circuited. This type of rotor can be operated under a different type of stator and is not limited by the pole number of the stator. It also has a simple and highly stable structure, in which the open circuit and short circuit fault conditions are not likely to occur.

Figure 2 -3 (b) introduces the wound rotor. The most vital advantages for the winding rotor are that the starting current can be adjusted within a specific range and the starting torque will not reduce because of the current reduction, as with the squirrel cage rotor. In this way, the winding rotor can keep the starting torque at the same level with a small starting current, which highly reduces the manufacturing cost for other parts, such as transformers, electrical components, and connecting wire.

(a)   (b)
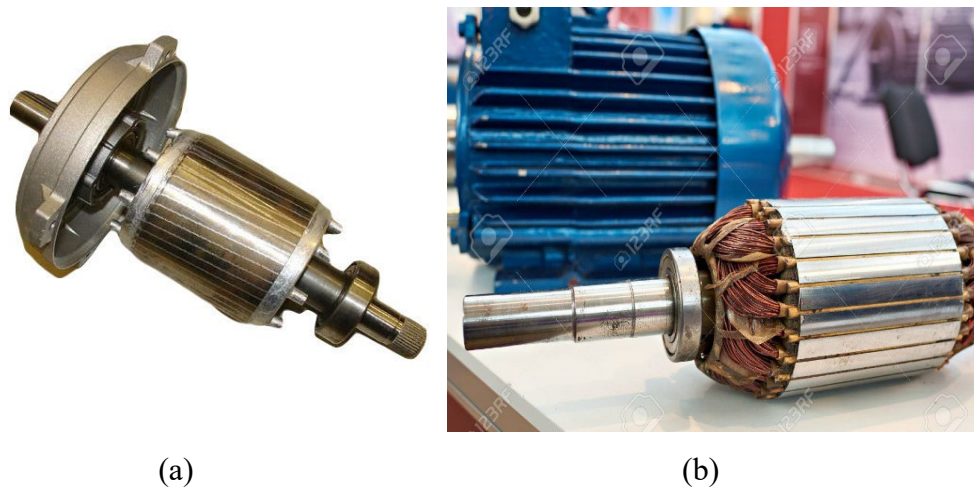
Figure 2 -3: Two typical rotors for induction machine

2.2.2 Mathematics Model

The equivalent circuit of the induction machine with all the parameters marked. Figure 2 -4 shows, the single-phase equivalent circuit for standard induction machine, where X_1 is the stator inductance, R_1 is the stator resistance, R_2 is the rotor resistance referred to the stator side,

X_2 is the inductance referred to the stator side, Z_M is the mutual inductance between the rotor and stator, $R_2/s\,(1-s)$ is the dynamic resistance that represents the load of the rotor.
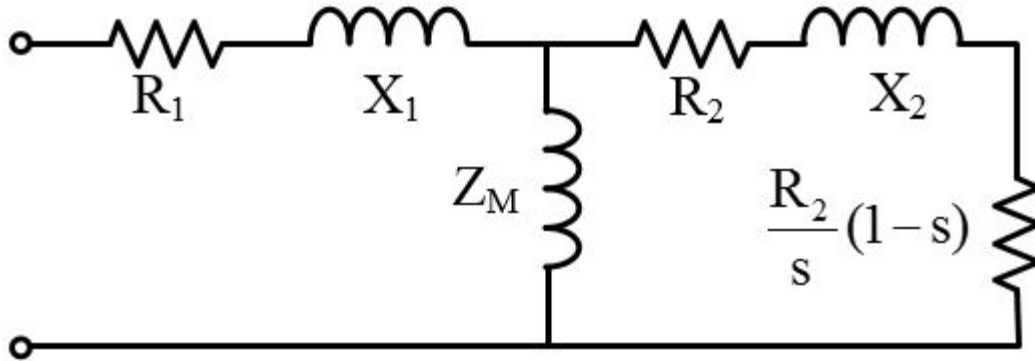
Figure 2 -4: The single-phase equivalent circuit for standard induction machine

For the induction machine, most of the vital characteristics in the steady-state can be calculated from the equivalent circuit, such as current, speed, and losses, as well as maximum torque and start torque. The power transferred across the air gap is P_t,

$$P_t = m_s I_2{}^2 \frac{R_2}{s} \tag{2 - 1}$$

Where m_s is the number of the stator phases, I_2 is the current in R_2. The total rotor loss is evidently

$$P_R = m_s I_2{}^2 R_2 \tag{2 - 2}$$

The internal mechanical power P_m can be calculated as

$$P_m = P_t - P_R = m_s I_2{}^2 \frac{R_2}{s} - m_s I_2{}^2 R_2 = m_s I_2{}^2 R_2 \frac{1-s}{s} \tag{2 - 3}$$

Or

$$P_m = (1-s)P_t \tag{2 - 4}$$

From this equation, it can be understood that the $(1-s)$ is the fraction of total transferred power that has been converted into mechanical power. The other 's' fraction of the total transferred power has dissipated into heat as rotor loss. Hence, the slip determines the efficiency of the induction machine; a high slip induction machine should be considered as an inefficient device [25].

The internal electromagnetic torque T corresponding to the internal power P can be obtained by recalling

$$P_t = \omega_s T \tag{2 - 5}$$

As a result,

$$P_m = (1 - s)\omega_s T \tag{2-6}$$

Where ω_s is the speed of the rotor in mechanical radians per second and T in Newton-meters.

With the equation (2-1) the Torque can be calculated as

$$T = \frac{1}{\omega_s} m_s I_2{}^2 \frac{R_2}{s} \tag{2-7}$$

Moreover, the synchronous speed is given by

$$\omega_s = \frac{4\pi f}{pole\ number} \tag{2-8}$$

However, the internal power and the internal torque are not the power and torque obtained at the output, due to the stay losses, friction, and windage affect.

To further illustrate some parameters that will be used to deduce the torque of a standard induction machine, Figure 2 -5, has been introduced.
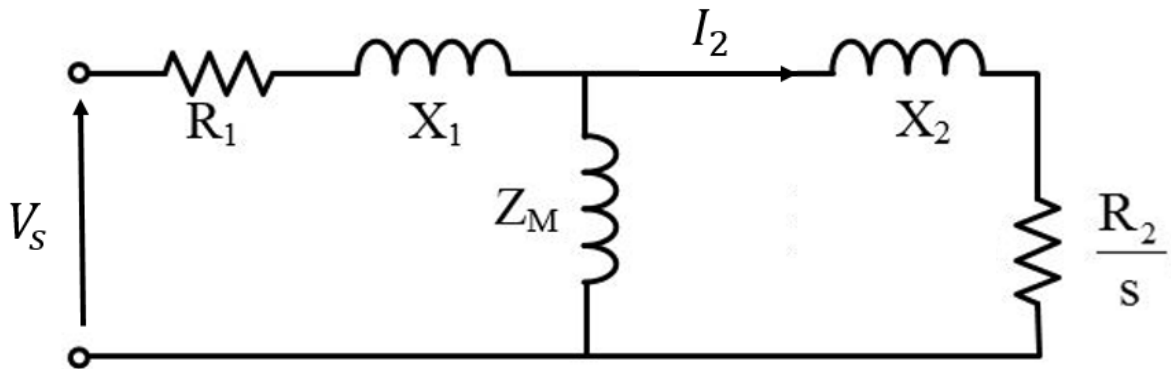
Figure 2 -5: The single-phase equivalent circuit with simplified rotor side

As shown in Figure 2 - 5, from the terminal of where the arrows point, according to [25], the I_2 can be calculated as

$$I_2 = \frac{V_s}{\sqrt{\left(R_1 + c\frac{R_2'}{s}\right)^2 + (X_1 + cX_2')^2}} \tag{2-9}$$

, where I_2 is the current in the rotor side, V_s is the stator voltage, R_2' is the rotor side of resistance without converting to the stator side, X_2' is the inductance of the rotor without converting to the stator side. For R_2' and X_2', there is

$$R'_2 = \frac{m_s}{m_r}\left(\frac{N_s k_{ws}}{N_r k_{wr}}\right)^2 R_2 \qquad (2 - 10)$$

$$X'_2 = \frac{m_s}{m_r}\left(\frac{N_s k_{ws}}{N_r k_{wr}}\right)^2 X_2 \qquad (2 - 11)$$

$$c = 1 + \frac{X_1}{X_m} \qquad (2 - 12)$$

Where m_s, m_r is the phase number of the stator and rotor, the N_s and N_r are the number of coils per phase of the stator and rotor, and k_{ws} and k_{wr} are the winding factor of the rotor and stator respectively.

Substituting (2 - 9) to (2 - 7), there will be

$$T = \frac{1}{\omega_s} m_s \frac{R_2}{s} \left(\frac{V_s}{\sqrt{\left(R_1 + c\frac{R'_2}{s}\right)^2 + (X_1 + cX'_2)^2}}\right)^2 \qquad (2 - 13)$$

$$T = \frac{m_s}{\omega_s} \frac{V_s^2 \frac{R_2}{s}}{\left(R_1 + c\frac{R'_2}{s}\right)^2 + (X_1 + cX'_2)^2} \qquad (2 - 14)$$

As it can be seen in (2 - 14), the obtained torque formula contains only the parameters in the single-phase induction machine equivalent circuit, which would help the further study and predicting the torque performance of the proposed induction machine.

In addition, for the induction machine modeling which will be shown later, the difference between the aluminum bars and copper bars shall have the effect of changing the maximum torque slip but not the maximum torque itself. From the maximum torque, it can be seen that the resistance and the inductance of the stator coil are inversely proportional to the maximum torque and proportional to the square of the voltage source. As seen in Figure 2 -6, the induction machine is made with a copper rotor bar, the resistance of which is less than that of aluminum. It is easy to observe that the speed of reaching the maximum torque exceeds the manufacture data, which show the same results as the literature.
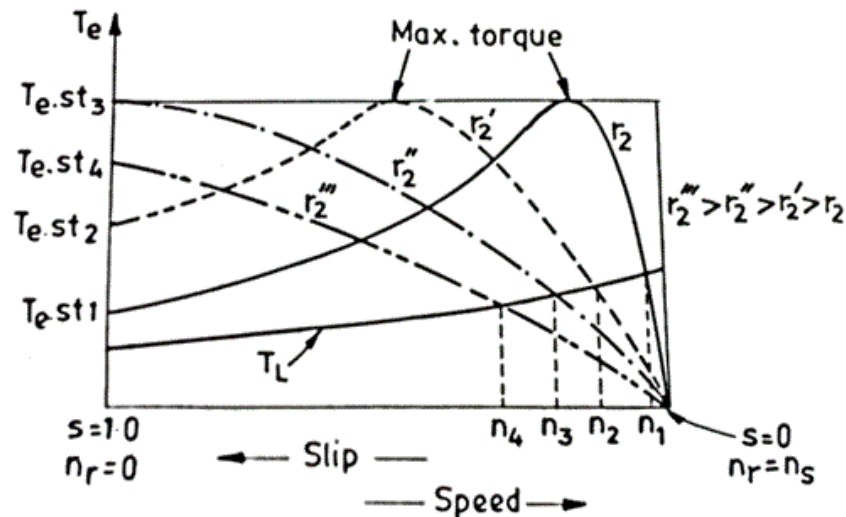
Figure 2 -6: The torque-speed curve for variety rotor resistance[26]

2.3 Typical fault analyzation

Induction machines are generally reliable, with the bearings being the most common source of failure [27]. Electrical faults include open circuits in stator windings, broken end rings, inter-turn short circuits in the stator winding, and broken rotor bars. However, when the induction machine is used in a drive, then the drive power electronics are generally judged to be far less reliable than the machine. The effect of these faults is to cause short-circuits or open circuits that are equivalent to such faults occurring in the winding. With appropriate post-fault control strategies, these can be made to appear as a symmetric open circuit and short-circuits at the winding terminals.

This project will predominantly focus on faults that correspond to open circuit at the terminal and short-circuits in the stator windings.

The inter-turn short circuit can be caused by a number of faults. Here some typical faults will be discussed, such as short circuits in stator windings occurring between turns of one-phase, two-phase or all-phase. Also, a short circuit between the stator core and winding conductor which can be seen in Figure 2 -8 Short circuit in the inter-turns in the one-phase.

a) Winding short circuit due to the lack of insulation.

b) End of the stator core short circuit with the winding.

c) Middle of the stator core short circuit with the winding.

d) Short circuit at the leads.

e) Short circuit between the phases.

(a)   (b)   (c)

(a)   (b)   (c)
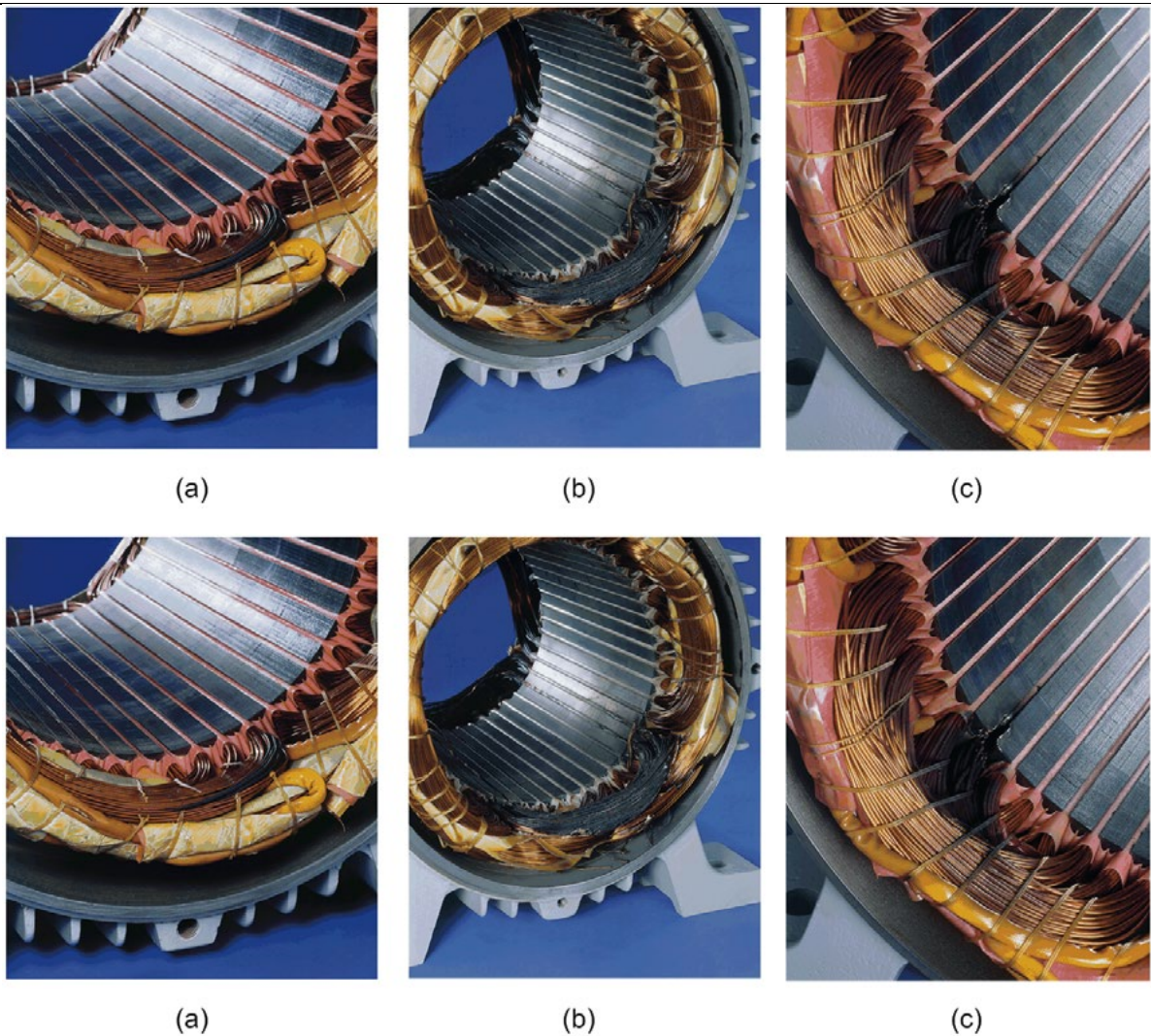
Figure 2 -7: Schematic diagram of the possible faults in induction machine[27]

Figure 2 -8 shows some faults may occur to the stator. However, due to the winding configuration and the fact that copper has excellent thermal conductivity, in the conventional induction machine, the fault will spread quickly around the stator and will cause a complete breakdown. Figure 2 - 9 demonstrates more severe fault conditions. They may be induced by running the faulted machine for an extremely long time or from the risk of doing the short circuit test.

- a) and b) show two types of the short circuit among all three phases which may be caused by the overload of the motor and rotor blocking as well as stator energization by sub-rated voltage and overrated voltage power supplies. Also, it may be caused by frequent start and rotation reversals.

- c) is an inter-turn short circuit which is similar to b); it is also due to the transient of the voltage, which may be caused by the successive reflection of the transient voltage. This kind of fault often happens on the cable side of the machine. For example, "some AC drives

may produce extra press on the stator windings due to the inherent pulse width modulation of the voltage applied to the stator winding." Also, this kind of fault can be caused by a long cable between the motor and the AC drive.

- d) and e) show a complete short circuit in one or more phases. If the short circuit occurs in more than one-phase, there will be a phase loss which can also be caused by open fuse, contactor, or breaker failure.

- f) shows an unbalanced stator voltage which is another kind of short circuit in one-phase. This kind of fault may be caused by the poor connection of the motor terminal, an unbalanced load in the power line, or a poor connection of the power line. In addition, one or more phases of the three-phase voltage are over or under the value of the other phase in this scenario.
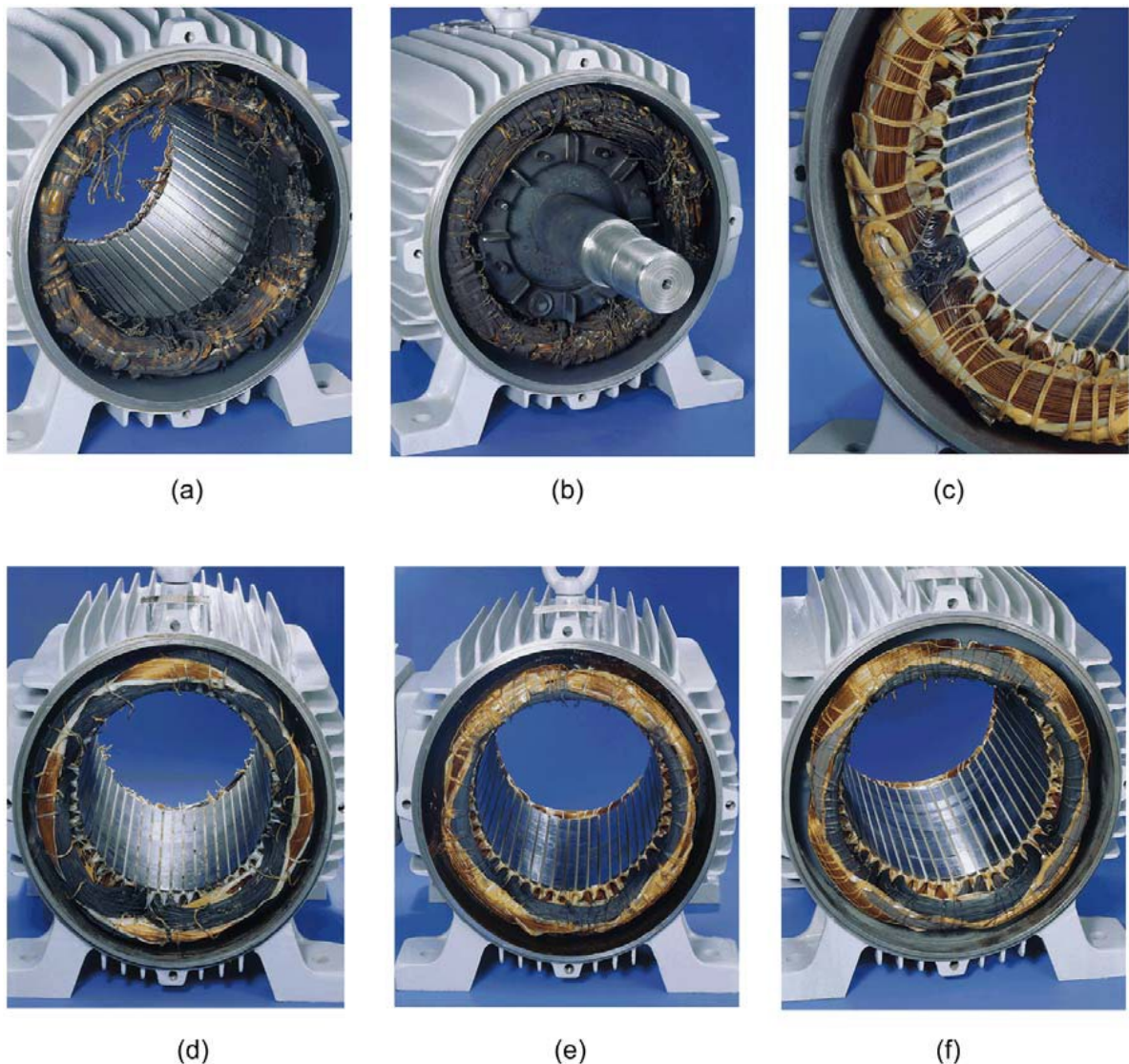
Figure 2 -8: Schematic diagram of the possible faults in induction [27]

It can be seen that the types of fault condition for an induction machine are various. In this project, not all types of fault condition are considered. However, the rotor side of the induction machine is simple in physical structure and electrical character. As a result, more fault happens to the stator side rather than the rotor side. Hence, in this thesis the fault condition only focuses on the stator fault. Additionally, the stator configuration of the triple three-phase induction machine further prevents the fault condition spreading to other segments, which leave fewer options for the fault conditions. As a result, in this project only the fault in the stator with the open circuit and short circuit condition in one or two segments will be studied and discussed.

2.3 Typical fault-tolerant induction machine topology

2.3.1 Fault-tolerant induction machine

The dual three-phase induction machines are one type of basic fault-tolerant induction machine. The advantages of employing the dual three-phase induction machine have been widely discussed, such as high efficiency [28], small torque ripple [29], and high reliability [30].

2.3.1.1 Typical dual three-phase winding connections and a comparison of their performance

In Figure 2 -10, a 48 slots eight poles double-layer induction machine stator has been shown, and the winding configuration has been displayed.
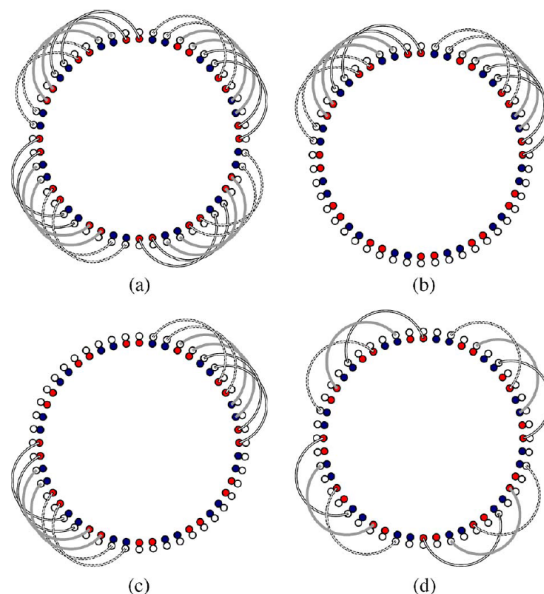
Figure 2 -9: Winding configuration of an eight poles 48 slots dual three-phase induction machine [30]

To test the fault-tolerant ability of the model, in [30], the author provides four different winding connections under the fault condition, as the dual three-phase stator is a double-layer winding. (a) is under the healthy condition, (b)-(c) are under half of the machine open circuit condition but with different winding connections. The performance of those connections varies because the different mutual coupling between the healthy and faulty parts is different.

To test the accuracy of the MMF harmonic analysation, the author first analyses the spatial harmonic component of the three-phase IM and the six-phase IM under the same power condition. Comparing (a) and (b) in Figure 2 -11, it is evident that the six-phase IM contains less low order harmonics, which is a well-known advantage for multiphase electrical machines.
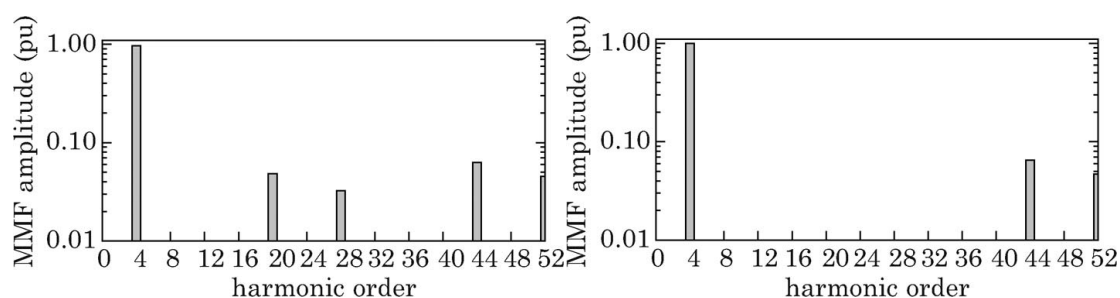
Figure 2 -10: The MMF harmonic spectrum of three-phase (left) and six-phase (right) IM [29]

As the author established that the accuracy of the MMF harmonic and the performance of the induction machine is solely depending on it, the harmonic content of the IM under fault configurations are presented and compared.
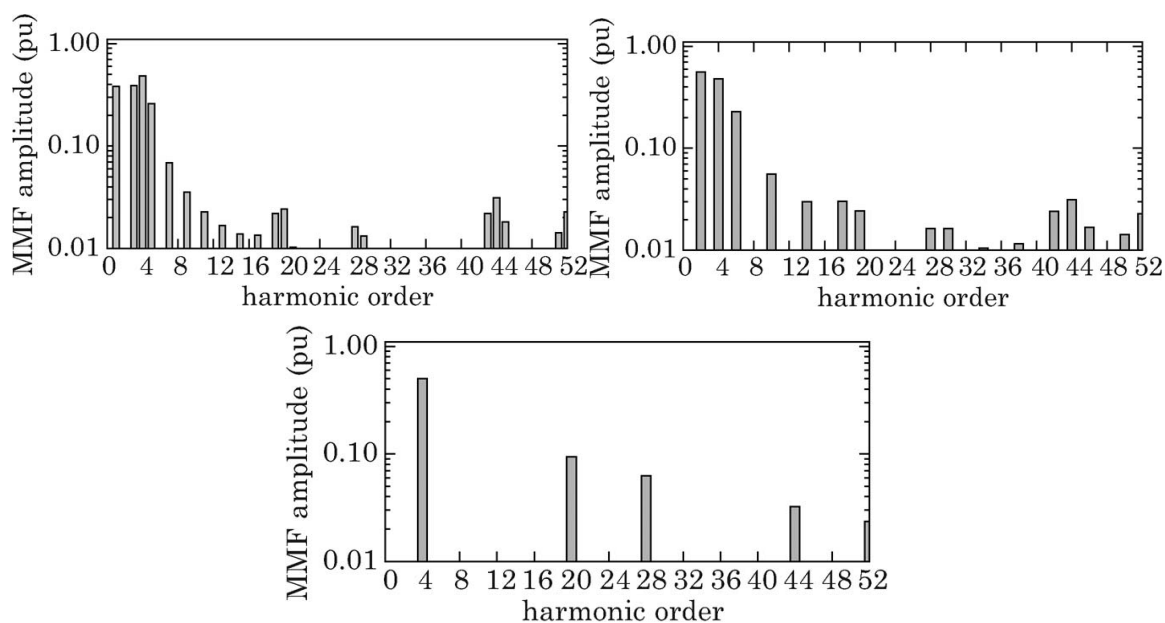
Figure 2 -11: Harmonic content for winding configuration (b), (c), and (d) respectively [29]

It can be seen in Figure 2 -12 that the harmonics for winding configuration (b) are abundant with a large number of lower-order harmonics such as first and third harmonics. Those harmonics would produce severe machine loss and parasitic torque, which would lead to poor performance under the fault condition.

The MMF harmonics components of configuration (c) show a series harmonics component including the second and fourth harmonics, but compared to winding (b), the lower order harmonic is significantly reduced. This phenomenon is because the winding of (b) is not as uniformly distributed as the winding in (c), which leads to the growth of the inverse sequence component.

The harmonic spectrum of winding (d) shows that even though the harmonic amplitude is slightly different from the three-phase healthy condition, the harmonic component is the same. In this case, the model is a uniformly distributed three-phase IM if the mutual coupling is ignored.

By analyzing the MMF harmonics in different conditions along with the simulation results, this paper draws the conclusion that (d) shows fewer losses, less phase current, more mechanical power, higher efficiency, and less rotor current in both the no-load test and full load test under the open circuit condition. It also discusses the short circuit performance for (b) and (c), but it fails to show the performance of the winding configuration (d), although due to the highly mutual coupled winding design, it can be deduced that the severe overcurrent shall result in a higher mutual coupling, which leads to the poor performance of the winding (d).

2.3.1.2 A five-phase induction machine using a combined star/pentagon stator winding connection

The pentagon winding connection is found to be ideal for open circuit operation because it provides a smaller degrading factor to the system. In other words, the faulted torque performance is higher than the star or delta connection. However, the star connection has unique advantages for eliminating triple harmonics while operating under healthy conditions. In [31], the author raised a new winding configuration for the fault-tolerant induction machine stator by combining the star and pentagon connections; the winding connection schematic has been shown in Figure 2 -13.
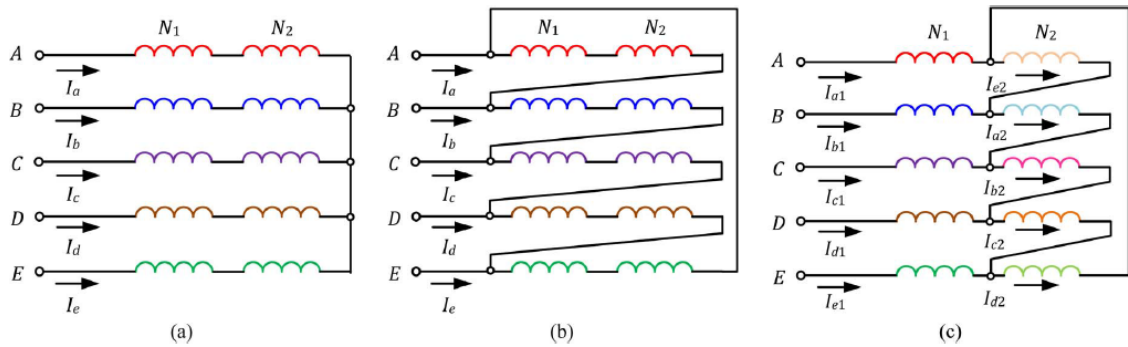
Figure 2 -12: The five-phase winding connections for (a) Star connection (b) Pentagon connection (c) Combined star/pentagon connection

The MMF is kept the same as the star connection for purpose of comparison. The induction machine used to apply this method is 40 slotted with a standard cage rotor. As a result, this induction machine operated as a dual five-phase machine with each side fed with a standard five-phase inverter which shifted in time with the angle of 18 degrees [31]. Furthermore, the motor shows great fault-tolerant ability. The torque comparison among the star connection, pentagon connection, and star/pentagon connection has been shown in Figure 2 -14. It can be seen that the star/pentagon connection performs better than the other two connections under the one-phase open circuit condition. The torque reduced to 90% compared to the healthy condition. However, as the author stated in the paper, the short circuit is out of the research range. Additionally, by researching the induction machine under the fault condition, the author of this thesis has found that the induction machine with a standard cage rotor is usually showing a torque tip at around 80% of the synchronous speed. However, this paper fails to demonstrate the speed curve around the speed of 1400 rpm, which means performance acceptability at the lower speed remains unknown.
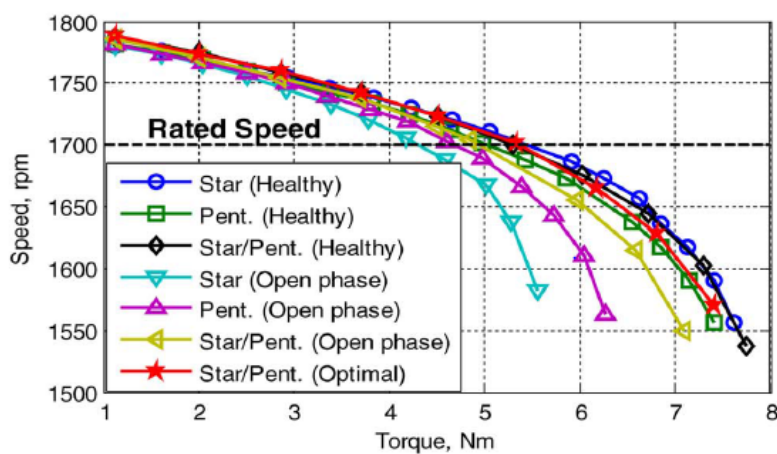
Figure 2 -13: The torque-speed curve comparison

2.3.2 Triple three-phase induction machine

Currently, a great interest in triple three-phase induction machine is in progress. Compared to the dual three-phase machine, it has the merit of more reliability, small torque ripple, higher efficiency, and optimization of the overall system due to the more segmented system [32].

2.3.2.1 Control method to achieve a triple three-phase fault-tolerant induction machine

New control methods have made it possible for the conventional triple three-phase induction to operate under the fault condition with a relatively high torque density and more efficiency. In [33], the study focuses on the MMF around the rotor under the fault condition. To replicate the same MMF before the fault happens, the three symmetrical sequence current components have been calculated for pre and post faulted condition. By eliminating the negative and zero sequences current component in the post fault system, the faulted system can achieve the same level of torque compared to the healthy condition model. During this procedure, the stator copper loss has been increased by 16.66% and 3.9% of the inverter loss [33].

In the same paper, the author also proposed another method. In this method, instead of considering the three sequence components, the focus is on the current magnitudes

$$MMF_{original} = \left(\frac{9}{2}\right) N \hat{I} e^{j\theta} \qquad (2 - 15)$$

, where $MMF_{original}$ is the MMF under the healthy condition, N is the number of the conductor in the slots, and θ is the electrical displacement between the slots.

Equation (2-17) illustrated the relationship between the peak current in the stator and the MMF. By re-adjusting the equation into a real part and an imaginary part, and if phase A is an open circuit, the equation is formed to be the system below.

$$\frac{9}{2} N \hat{I} cos\theta = 2NI_p[\cos(40°) + \cos(20°)] \cos(\delta) \qquad (2 - 16)$$
$$+ 2I_p[\cos(80°) + \cos(60°)] \cos(90° + \delta/2) \, cos\theta$$

$$\frac{9}{2} N \hat{I} sin\theta = 2NI_p[\sin(40°) + \sin(20°)] \sin(\delta) \qquad (2 - 17)$$
$$+ 2I_p[\sin(80°) + \sin(60°)] \sin(90° + \delta/2) \, sin\theta$$

Where I_p is the magnitude of the eight-phase current under the fault condition. As the method maintains the same amplitude of the current, the absolute value of the current in each phase is $I_p \hat{I}$. With two equations and two unknowns, the solution of δ and I_p can be calculated. In this

way, each stator phase current has been calculated with the new balance of the phase difference and the magnitude of the current. By adjusting the current into the calculation results, the machine would function as a new eight-phase motor to avoid the side-effects of the motor operating under a fault condition.

However, this new control method must assume the motor is only possible to operate under a one-phase open circuit condition. If the fault in the motor is anything other than that condition, the control method is no longer suitable. Since predicting the fault type before the fault condition occurs is considerably complicated, future work can focus on fault condition distinguishing or prediction.

2.3.2.2 Modelling and control of a fault-tolerant nine-phase induction machine

In [32], the fundamental problems in the modeling and control of nine-phase induction motors operating in the absence of one phase failure is explored. The development of the proposed model is described in detail, including an algorithm that ensures the correct representation of the isolated neutral motor. The simulation results illustrate the post-fault behavior of the nine-phase motor due to the phase loss, including the elimination of torque ripple by employing appropriate control methods. The experimental results from the laboratory test setup are described. The results of the experiment illustrate the operation of a nine-phase induction motor under a phase loss fault and are used to verify the proposed model.

As seen in Figure 2 -15 (a), the induction machine is connected in a star connection, and there is a 40-degree phase difference between each phase. Also, the stator winding configuration has been displayed in Figure 2 -15 (b).

Three-phase system 1: I_1, I_4, I_7
Three-phase system 2: I_2, I_5, I_8
Three-phase system 3: I_3, I_6, I_9

(a)   (b)
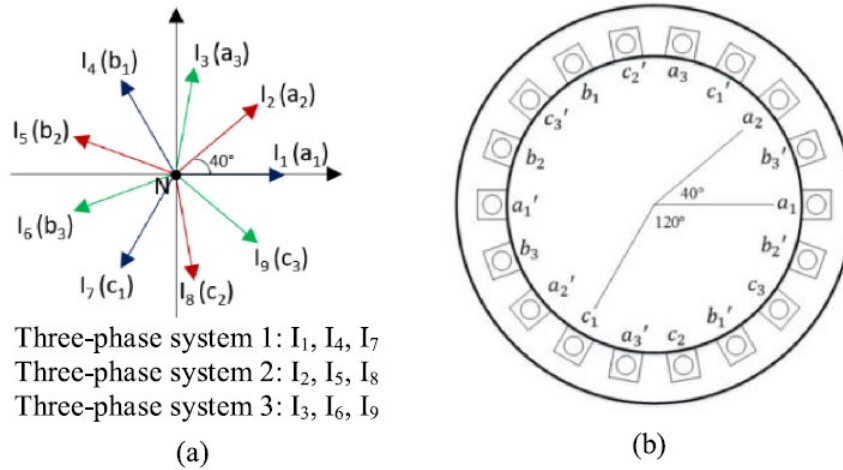
Figure 2 -14: Current diagram and winding configurations for the nine-phase induction machine with two poles [32]

When the open circuit fault occurs to a_1, the control method from **2.3.2.1** will be applied to the motor, which will produce the same MMF for the rotor compared to the healthy condition. In the post fault condition, the inductance on the q axis, L_q, is not changed, but L_d is decreased and the new inductance is $L_d^{'}$. To compensate for the loss of the stator MMF, the stator current i_{sa} should be increased by the factor of 1.1339. The torque ripple can be eliminated if

$$\frac{I_\alpha}{I_\beta} = \frac{L_q}{L_d^{'}}$$ (2-18)

where I_α and I_β are the amplitude of stator current in the α and β axis. According to different fault conditions, different $\alpha\beta$ stator currents will be calculated to suppress the torque ripple.
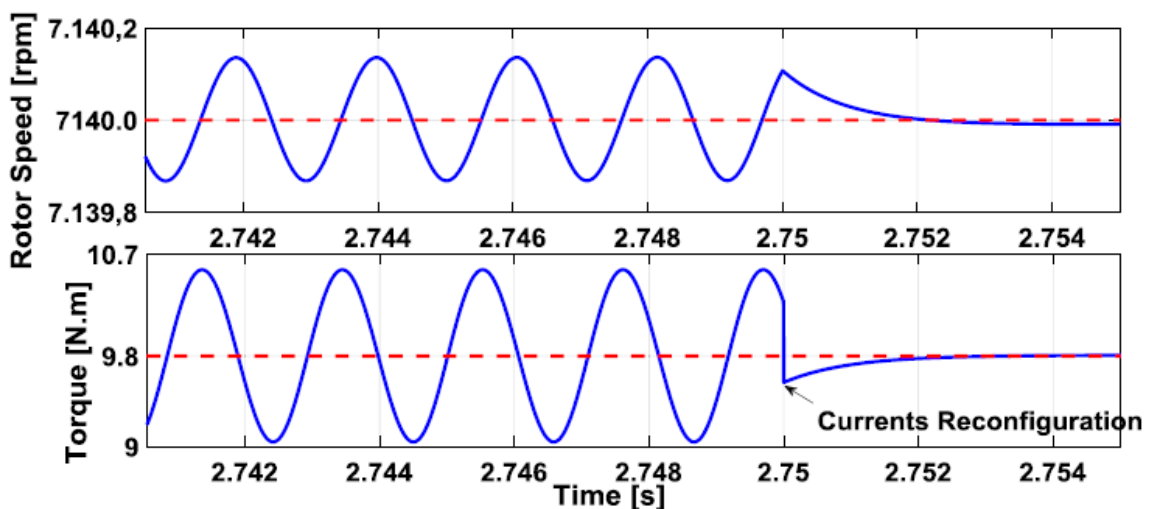
Figure 2 -15: Torque ripple suppression results by the current compensation method [32]

Figure 2 -16 shows the triple three-phase induction machine under a one-phase open circuit condition. The current compensation method has been applied to the system at 2.75s, which reduces the rotor speed and the torque to a small level of oscillation. The motor is operated at 0.05 slip, which is the rated speed.

2.3.2.3 Fault-tolerant control of MIM drives based on a virtual winding method [34]

The MIM shows excellent potential in operating under a fault condition and maintaining a consistent torque performance. Many researchers try to control the MIM with a current control unit to the asymmetrical machine structure [23, 35-37]. In [34] the author proposes a virtual winding method for precise current control and flux observation. By using this method, under the open circuit fault condition for one or more phases the rest of the machine can be still treated as a symmetrical induction machine with virtual winding instead of faulted.

In the simulation and test verification, a five-phase induction machine with a standard cage rotor has been adopted. The experimental platform has been shown in Figure 2 -17. The performance of the five-phase machine drive has been shown in Figure 2 -18. Under the fault condition, the control method performs better by controlling the q-axis current more similarly to the reference current compared to the conventional control method.
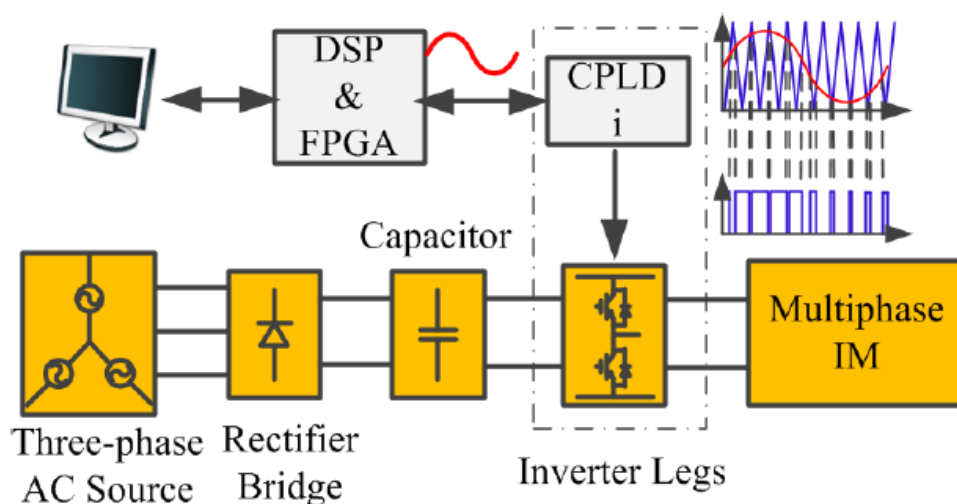
Figure 2 -16: Block diagram of the experimental platform[34]
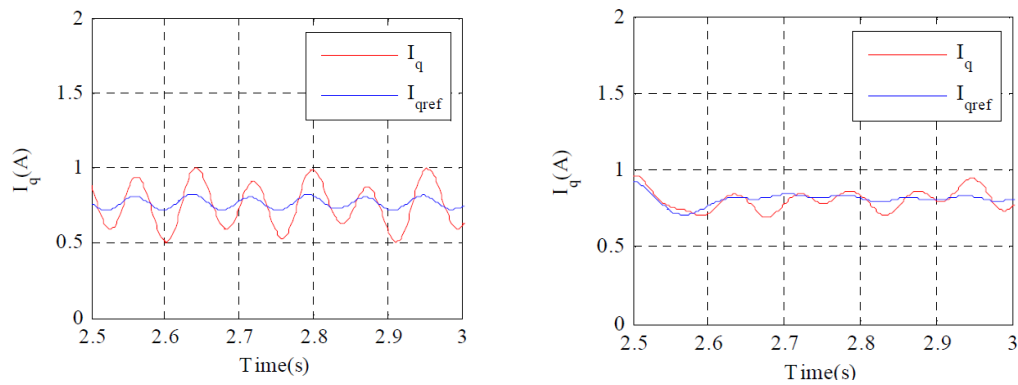
Figure 2 -17: The q-axis current before and after the control method[34]

2.4 Summary

In this section, the literature on the induction machine and the current research stage of the fault-tolerant induction machine has been fully demonstrated and discussed. Firstly, many advantages and applications of the MIM have been introduced. The introduction started with the general advantages of the MIM, and then the possible application to the marine and aerospace industries. Due to the high level of similarities between the induction machine and synchronous machine, the development of the multiphase synchronous machine has also been studied. Secondly, some of the fundamental principles of the induction machine have been presented. The mathematical model of a single-phase equivalent circuit has been presented with the equation to obtain the mechanical torque. In addition, the fault types of an induction machine have been discussed and sorted into different groups for a full understanding of the fault condition and to narrow the scope of this project. Thirdly, the fault-tolerant induction machine's current development has been presented and discussed. In this section, two types of fault-tolerant induction machines have been focused on, the dual three-phase induction machine and the triple three-phase induction machine. During the literature review, it has been found that most studies of the triple three-phase induction machine study have examined the converter level, instead of the design of the induction machine. In the few examinations of designing the fault-tolerant induction machine, most papers overlook the problem that occurs to the triple three-phase induction machine when the speed range changes from the rated slip to a higher slip such as 0.2. In the meantime, most papers focus on the open circuit condition. Some study the short circuit condition but fail to provide a method to optimize the performance. As a result, this project will focus on the problems that occur to the triple three-phase induction machine at all speed ranges under not only the open circuit condition but short circuit condition and proposes a method to solve this problem at the machine design level.

.

2.5 Reference

1.   Lyra, R.O.C., and T.A. Lipo. Torque density improvement in a six-phase induction motor with third harmonic current injection. in Industry Applications Conference, 2001. Thirty-Sixth IAS Annual Meeting. Conference Record of the 2001 IEEE. 2001.

2.   Farquharson, D., P. Jaramillo, and C. Samaras, Sustainability implications of electricity outages in sub-Saharan Africa. Nature Sustainability, 2018. **1**(10): p. 589-597.

3.   Alger, P.L., E.H. Freiburghouse, and D.D. Chase, Double Windings for Turbine Alternators. American Institute of Electrical Engineers, Transactions of the, 1930. **49**(1): p. 226-244.

4.   Franklin, P.W., A Theoretical Study of the Three Phase Salient Pole Type Generator with Simultaneous AC and Bridge Rectified DC Output-Part I. Power Apparatus and Systems, IEEE Transactions on, 1973. **PAS-92**(2): p. 543-551.

5.   Schiferl, R.F., and C.M. Ong, Six Phase Synchronous Machine with AC and DC Stator Connections, Part I: Equivalent Circuit Representation and Steady-State Analysis. Power Apparatus and Systems, IEEE Transactions on, 1983. **PAS-102**(8): p. 2685-2693.

6.   Menzies, R.W., P. Steimer, and J.K. Steinke, Five-level GTO inverters for large induction motor drives. Industry Applications, IEEE Transactions on, 1994. **30**(4): p. 938-944.

7.   Liwei, W., et al. Physical variable modeling of multiphase induction machines. in 2008 Canadian Conference on Electrical and Computer Engineering. 2008.

8.   Apsley, J.M., et al. Experimental validation of load disturbances on a multiphase marine propulsion drive model. in 2008 4th IET Conference on Power Electronics, Machines, and Drives. 2008.

9.   Nanoty, A.S., and A.R. Chudasama. Design of multiphase induction motor for electric ship propulsion. in 2011 IEEE Electric Ship Technologies Symposium. 2011.

10.   Zicheng, L., et al. Modeling and control of 15-phase induction machine under one phase open-circuit fault. in 2013 International Conference on Electrical Machines and Systems (ICEMS). 2013.

11.   Boglietti, A., et al., Efficiency Analysis of PWM Inverter Fed Three-Phase and Dual Three-Phase High Frequency Induction Machines for Low/Medium Power Applications. Industrial Electronics, IEEE Transactions on, 2008. **55**(5): p. 2015-2023.

12.   Apsley, J.M., et al., Induction motor performance as a function of phase number. Electric Power Applications, IEE Proceedings -, 2006. **153**(6): p. 1.

13.   Williamson, S. and S. Smith, Pulsating torque and losses in multiphase induction machines. Industry Applications, IEEE Transactions on, 2003. **39**(4): p. 986-993.

14.   Jahns, T.M., Improved Reliability in Solid-State AC Drives by Means of Multiple Independent Phase Drive Units. Industry Applications, IEEE Transactions on, 1980. **IA-16**(3): p. 321-331.

15.   Levi, E., Multiphase Electric Machines for Variable-Speed Applications. Industrial Electronics, IEEE Transactions on, 2008. **55**(5): p. 1893-1909.

16.   Bennett, J.W., et al., Safety-critical design of electromechanical actuation systems in commercial aircraft. IET Electric Power Applications, 2011. **5**(1): p. 37-47.

17.   Mecrow, B.C., et al., Drive Topologies for Solar-Powered Aircraft. IEEE Transactions on Industrial Electronics, 2010. **57**(1): p. 457-464.

18.   Bo Wang, J.W., Antonio Griffo, Zhigang Sun, and Ellis Chong, A Fault Tolerant Machine Drive Based on Permanent Magnet Assisted Synchronous Reluctance Machine. 2016.

19.   Liu, G., et al., Design and Analysis of Five-Phase Fault-Tolerant Interior Permanent-Magnet Vernier Machine. IEEE Transactions on Applied Superconductivity, 2016. **26**(4): p. 1-5.

20.   Kianinezhad, R., et al., Modeling and Control of Six-Phase Symmetrical Induction Machine Under Fault Condition Due to Open Phases. Industrial Electronics, IEEE Transactions on, 2008. **55**(5): p. 1966-1977.

21.   Kianinezhad, R., et al. Analysis and evaluation of DTC and FOC in open phase fault operation of six-phase induction machines. in Electrotechnical Conference, 2008. MELECON 2008. The 14th IEEE Mediterranean. 2008.

22.   Hosseyni, A., et al. Fault tolerant control strategy of a five-phase permanent magnet synchronous motor drive. in 2015 16th International Conference on Sciences and Techniques of Automatic Control and Computer Engineering (STA). 2015.

23.   Bojoi, R., et al. Analysis of the asymmetrical operation of dual three-phase induction machines. in Electric Machines and Drives Conference, 2003. IEMDC'03. IEEE International. 2003.

24.   Sui, Y., et al., A novel five-phase fault-tolerant modular in-wheel permanent-magnet synchronous machine for electric vehicles. Journal of Applied Physics, 2015. **117**(17): p. 17B521.

25.   Sen, P.C., Principles of electric machines and power electronics. Third edition.. ed. 2014: Hoboken, New Jersey : John Wiley and Sons, Inc.

26.   Nasar, I.B.S.A., The Induction Machines Design Handbook, ed. S. Edition. 2010, United State of America: CRC Pressof Taylor&Francis Group , an Informa business. 827.

27.   Marques, M., et al. Fault Detection and Diagnosis in Induction Machines: A Case Study. in Technological Innovation for the Internet of Things. 2013. Berlin, Heidelberg: Springer Berlin Heidelberg.

28.   Munoz, A.R. and T.A. Lipo, Dual stator winding induction machine drive. Industry Applications, IEEE Transactions on, 2000. **36**(5): p. 1369-1379.

29.   Alberti, L. and N. Bianchi, Experimental Tests of Dual Three-Phase Induction Motor Under Faulty Operating Condition. Industrial Electronics, IEEE Transactions on, 2012. **59**(5): p. 2041-2048.

30.   Alberti, L. and N. Bianchi. Impact of winding arrangement in dual 3-phase induction motor for fault tolerant applications. in The XIX International Conference on Electrical Machines - ICEM 2010. 2010.

31.   Abdel-Khalik, A.S., et al., An Improved Fault-Tolerant Five-Phase Induction Machine Using a Combined Star/Pentagon Single Layer Stator Winding Connection. IEEE Transactions on Industrial Electronics, 2016. **63**(1): p. 618-628.

32.   Souza, T.S.d., R.R. Bastos, and B.J.C. Filho, Modeling and Control of a Nine-Phase Induction Machine With Open Phases. IEEE Transactions on Industry Applications, 2018. **54**(6): p. 6576-6585.

33.   Souza, T.S.d., R.R. Bastos, and B.J.C. Filho. Fault-tolerant operation of a nine-phase induction machine with open phases. in 2017 IEEE Industry Applications Society Annual Meeting. 2017.

34.   Zhong, P., et al. Fault-tolerant control of multiphase induction machine drives based on virtual winding method. in 2017 IEEE Transportation Electrification Conference and Expo (ITEC). 2017.

35.   Che, H.S., et al., Current Control Methods for an Asymmetrical Six-Phase Induction Motor Drive. IEEE Transactions on Power Electronics, 2014. **29**(1): p. 407-417.

36.   Jones, M., et al., A Synchronous Current Control Scheme for Multiphase Induction Motor Drives. IEEE Transactions on Energy Conversion, 2009. **24**(4): p. 860-868.

37.   Tani, A., et al., Control of Multiphase Induction Motors With an Odd Number of Phases Under Open-Circuit Phase Faults. IEEE Transactions on Power Electronics, 2012. **27**(2): p. 565-577.

Chapter 3 Conventional Cage Rotor Three-phase Induction Machine Modelling

To set the comparison base for the triple three-phase induction machine, a conventional induction machine was first modelled with the FEA software. The most substantial challenge of this part is that the machine was pre-built and cased. As a result, the machine had to be disassembled to measure the specifications for simulation and optimization. To replicate the performance of the induction machine, the inter-connection of the stator was investigated, as well as the number of turns and other parameters of the induction machine. In this part, two identical machines were purchased, one was disassembled for study and measurement purpose, and the other one was kept intact for further optimization.

3.1 The outline parameters for the conventional induction machine

To become familiar with the software, a full machine has been constructed. In order to fully understand the purchased machines, all the scale-related parameters have been taken into consideration in terms of measurement and constructed in the FEA software. However, as some of the parameters are irrelevant to this project, such as casing size, only the parameters that are involved in the FEA software are presented in Table 1.

Table 1: The relevant parameters of the conventional induction machine

Parameter	Scale	Unit	symbol
Stator outside diameter	160.0	mm	D_out
Stator inside diameter	103.9	mm	D_g
Stator slots	36		Z_s
Number of poles	6		Two_p
Coil turns	63		T_c
Stator winding parallel paths	2		a_s
Core length	161.0	mm	L0
Stacking factor	0.46		k_s
Rotor outside diameter	103.4	mm	D-r
Rotor inside diameter	35.9	mm	D_in
Rotor slots	26		Z-r

Rated frequency	50	Hz	f_e
Rated voltage	400	Volts	V_f
Rated torque (slip 0.05)	22.1	N·m	
Rated current (slip 0.05)	5.6	A	
Power factor(slip 0.05)	0.69		
Speed (slip 0.05)	950	rev/min	
Efficiency(slip 0.05)	82.5%		

These parameters are obtained from the measurement and manufacturing data. The general structure of the conventional induction machine has been presented in Figure 3 -1 and Figure 3-2.
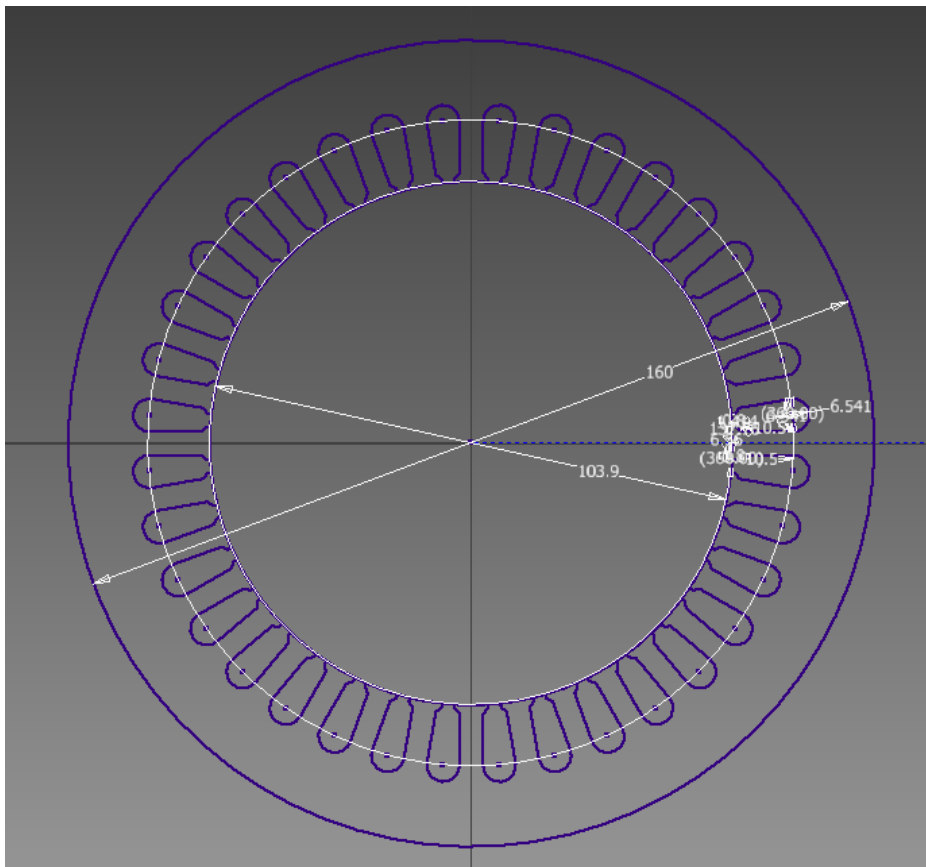
Figure 3 -1: The general dimensioned stator drawing of the conventional induction machine
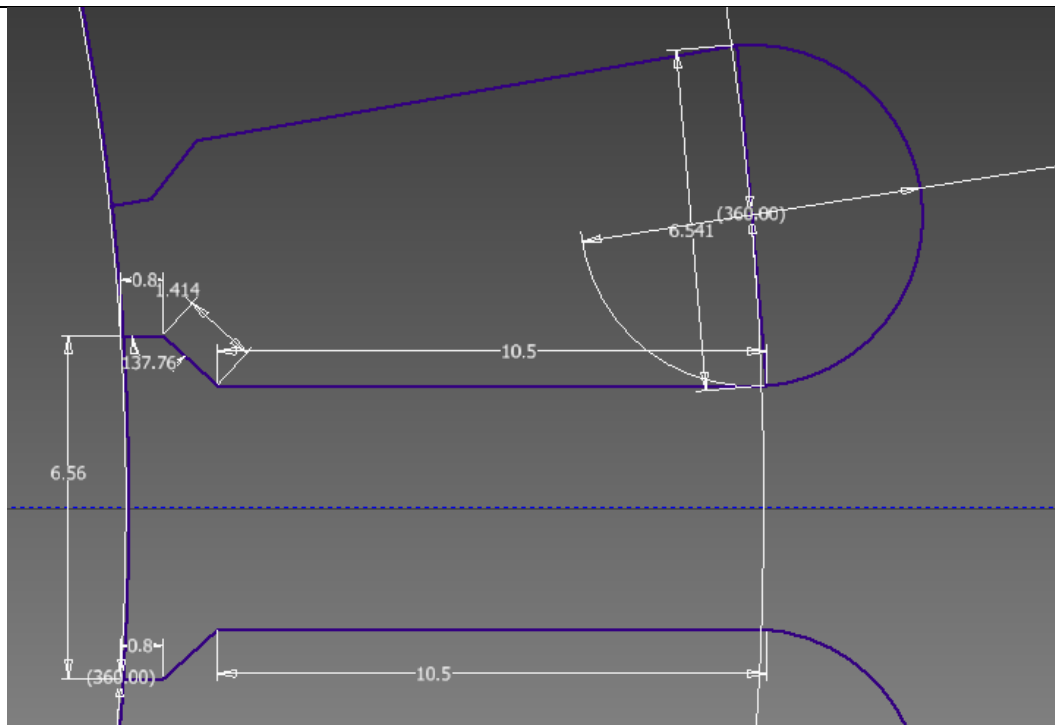
Figure 3 -2: The amplification of the stator in the slot area

According to the nameplate shown in Figure 3 -3 and Table 2, there are three operating modes.

Figure 3 -3: A photo of the manufacture induction machine's nameplate

Table 2: Transcript of the nameplate on the manufacturing machine

V	Hz	rpm	A
690Y	50	950	3.10
400D	50	950	5.50
460D	60	1160	4.70

As a result, there are two connections for the same machine, which are star-connected and delta connected. The manufacture data has given the rated voltage as 400 V. As a result, 400 V should be the line to line voltage, which means all the voltage sources should be connected in star with a 120 degree phase difference.

The nameplate has given three working modes for the 690 V with star connection and 400 V with delta connection. The two modes mentioned above are equivalent since the phase voltage is kept the same as 400 V. In that case, there are only two types of work modes in 50Hz and 60 Hz respectfully. For the 60 Hz one, it is the supporting data for the model to operate in the USA, where the electrical industrial frequency is 60 Hz. As a result, the 60 Hz operating mode will not be focused on in this project.

3.2 The construction of the conventional induction machine

The construction of the conventional induction machine is based on the script written in Excel with vbs., which was created by Dr. Richard Martin for building the Switch reluctance machine (SRM) but modified by the author to fit the induction machine.

(a)   (b)
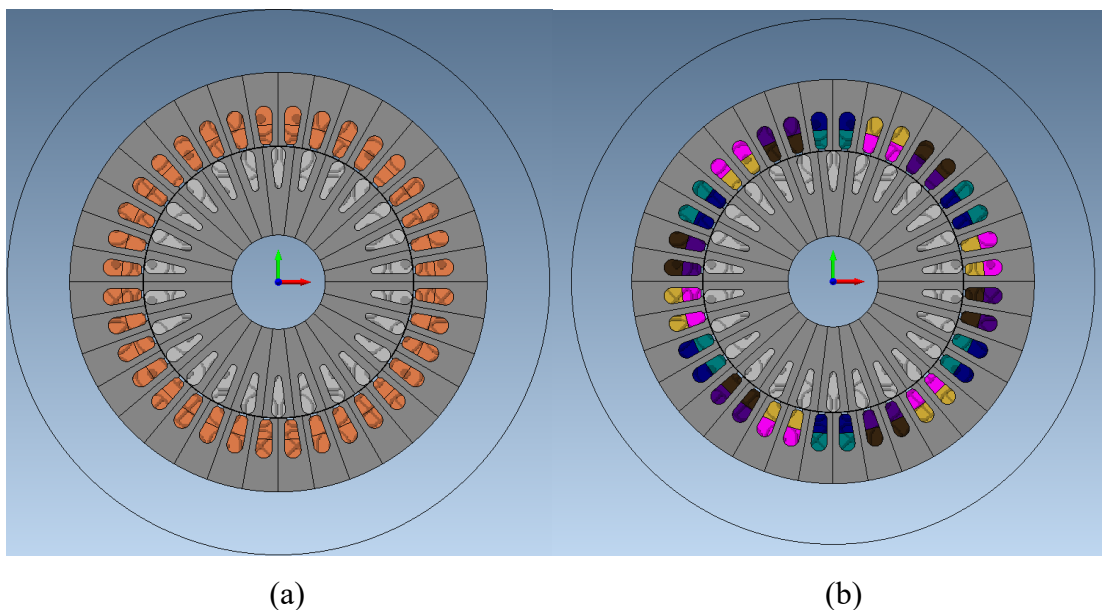
Figure 3 -4: The structure and winding configurations of the conventional induction machine

Figure 3 -4 (a) is the simulation model for the conventional induction machine. As the logic of the script is built on SRM, the induction machine is segmented in the rotor and the stator, which has been changed manually in the following discussion. Figure 3 -4 (b) is the simulation model with slots colored to show the winding connection of the stator. The same color slots are

connected to the same coil. The machine is a fully pitched double-layer six-pole machine with an aluminum squirrel cage rotor. As can be seen in Figure 3 -4, the 2-D machine is axisymmetric. As a result, the model can be simplified into a half model with boundary condition to reduce time in simulation, as shown in Figure 3 -5.
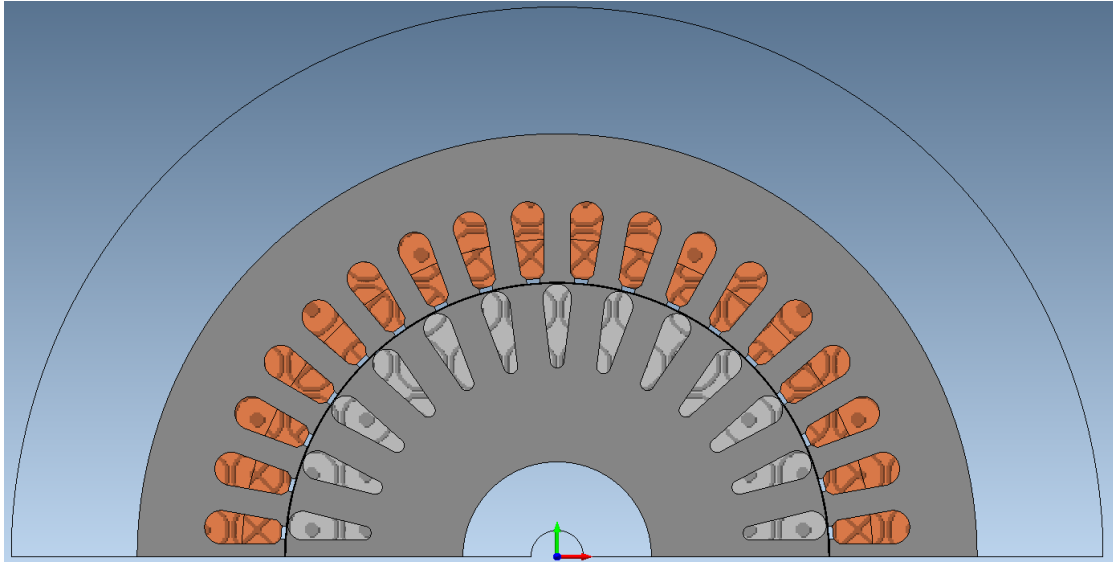
Figure 3 -5: The simplified half model with odd boundary condition

3.3 The simulation results of the conventional induction machine

Before the simulation, the construction of the model needs to be validated to guarantee the results from this model are trustworthy. The default field results have been shown in Figure 3 - 6.
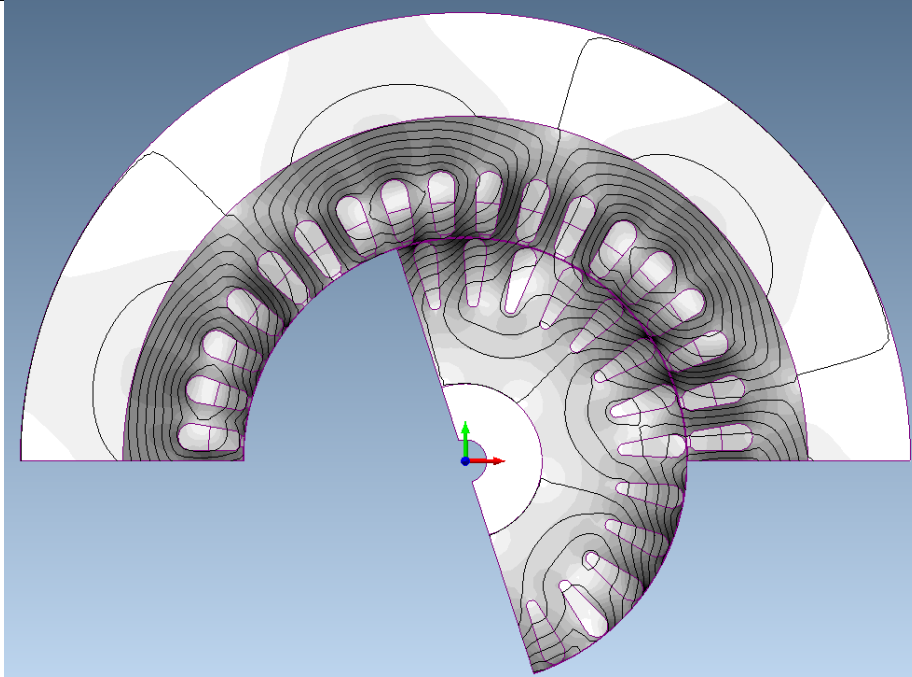
Figure 3 -6: The default field schematic of the half model with boundary condition

The default field shows that the model is connected correctly in terms of phase and pole number. The boundary condition has been set to "odd", which can be observed in Figure 3 -6 as well.

The model was first simulated at the rated torque speed, 950 RPM, with 5.6 A in RMS current source feed each phase with the constant current.

The circuit connection is vital for most machines; the way of connecting the stator coils decides the machine type, pole numbers, back EMF, etc. For this machine, which has been calculated to prove that there is no need for parallel circuits, it is much more straightforward. The calculation has been omitted for the concision of the report. The physical construction and winding configuration of the half-machine has been presented in Figure 3 -7.

It can be seen from Figure 3 -7 that it is a standard six-pole three-phase squirrel cage induction machine with the odd boundary condition. It is supplied with three 5.6 A current sources, at the rated slip which is 0.05. The odd boundary condition is, by omitting the other, the central symmetrical part of the machine, which produces 1/scale of the machine's performance to reduce simulation time. As shown in Figure 3 -7, the windings, which are shaded in the same color, are receiving power from the same source. Therefore, the machine is fully pitched. The reason that the current source is applied here is that the voltage source is rather complicated for the MagNet computing because the current of the voltage source is what MagNet needed to calculate the torque and other results. Therefore, if a voltage source is applied the software has to calculate the current first then compute the results. At the early stage of the research, the rated current at rated slip has been adopted for model checking.

The odd boundary condition is chosen for the physical construction of the full conventional induction machine. For a three-phase induction machine with 36 slots and 26 rotor bars, it can be divided into four identical parts. However, the circuit connection is 120 degrees short-pitched, which means the direction of the current is not identical in each part, necessitating the half-machine model. The odd boundary condition is being used in the scenario that the half-machine is centro-symmetric to the other part, which is precisely the case here. As a result, the odd boundary condition is chosen here.
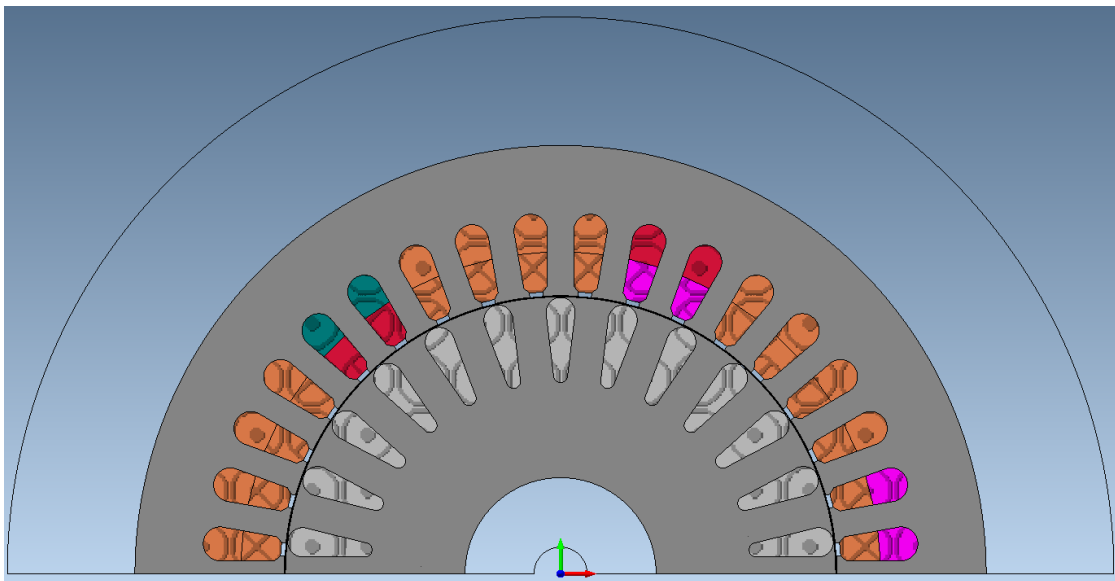
Figure 3 -7: The winding configuration of the half model with boundary condition

Following the logic of research, the most straightforward connection has been chosen here, which is that each current source feeds the corresponding phase. Additionally, the current has been set to 5.6 A in RMS, as shown in Figure 3 -8. The current source would provide the precise current to the stator, which would allow the author to focus more on adjusting the parameters of the induction machine.
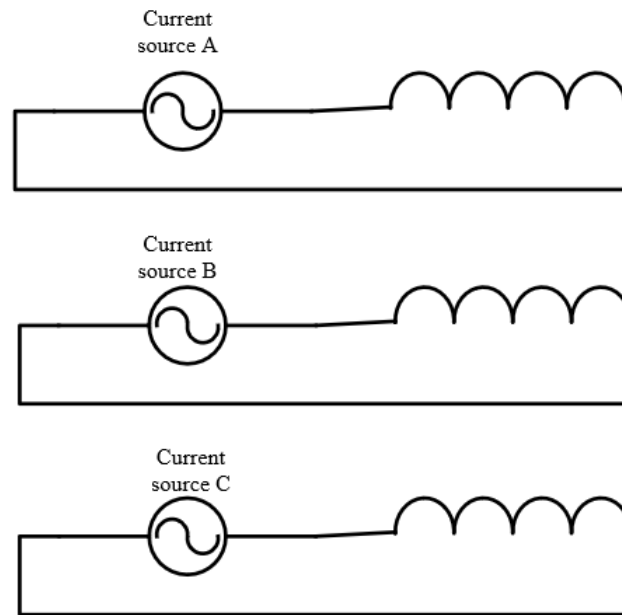
Figure 3 -8: The half-machine with odd boundary condition fed with three current sources set to 5.6 A at the rated slip

The simulation for the current source is only capable of providing the torque performance under the rated slip. To obtain the performance of the induction machine under other speeds, the voltage source model has been designed to fulfill the purpose, as seen in Figure 3 -9.
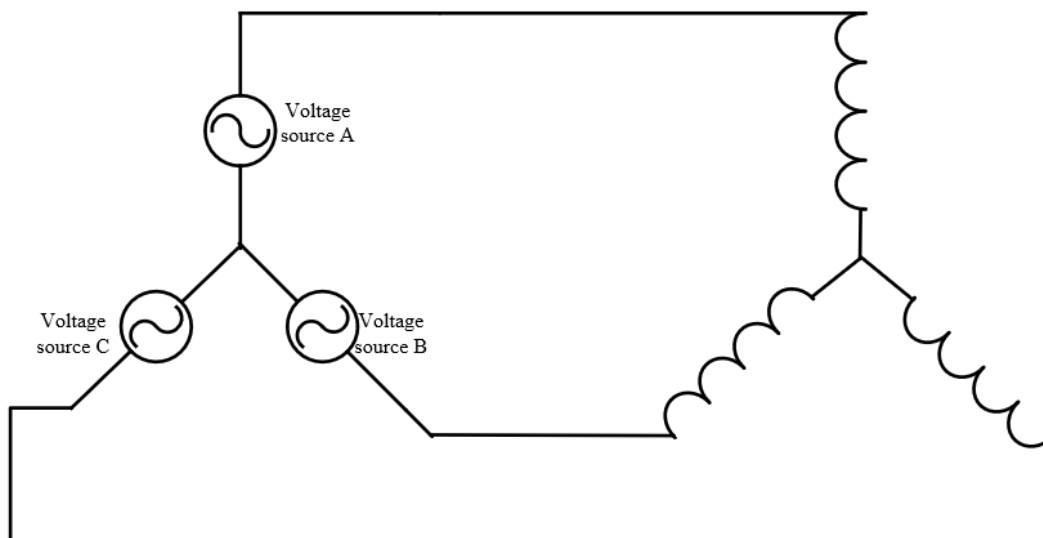
Figure 3 -9: The half-machine with odd boundary condition fed with three voltage source set to 400 V RMS at the rated slip

Generally speaking, as torque ripples may cause noise and vibrations and shorten the life span of the machine, they are undesirable. They are also the main reason for causing the extensive torque ripple which is the interaction between the MMF and the airgap flux harmonics. This

can be avoided by changing the geometry of the machine; for most scenarios, the percentage of the difference between the maximum torque and the minimum torque compared with the average torque is defined as torque ripple.

As a result, the torque-time curves have been obtained from the simulation at the rated slip. The simulation was operated with a star-connected voltage source with 400 V in RMS. The frequency was set to 50 Hz according to the nameplate. The max value of the torque performance can be organised and compared in EXCEL, which is 22.95N·m, and the minimum value is 18.85 N·m. Hence, the torque ripple is

$$T_{rp} = (MAX - MIN) \times \frac{scale}{T_{mean}} = (22.95 - 18.85) \times \frac{2}{47.9} = 17.11\%$$
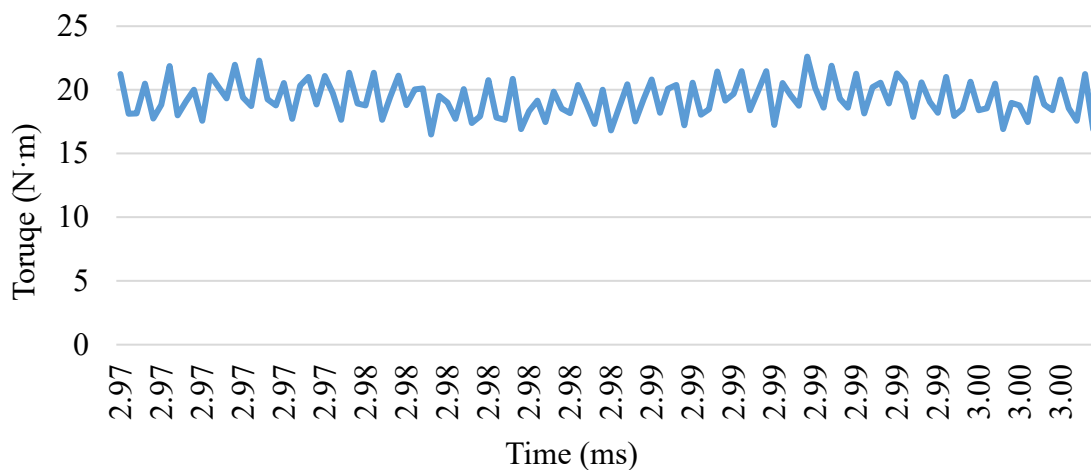
Figure 3 -10: The torque-time curve for the half model with voltage control

3.4 The end winding calculations

The complete construction of the induction machine includes the end winding resistance and inductance. The end windings of the motor are very complex in shape and vary greatly depending on the winding type. The adjacent metal components have a significant influence on the distribution of magnetic field leakage, but the type of metal components and function vary with the type of the motor. As a result, it is difficult to accurately calculate the magnetic permeability of the leakage resistance at the end of the machine. Many scholars have done theoretical research and experimental analysis to obtain some expressions with empirical correction coefficients. In the following section, some of those studies will be introduced and discussed.

3.4.1 The end winding resistance calculation

As mentioned in Table 1, the outline of the motor has been shown in Figure 3 -11. The winding inside each segment is fully pitched three-phase winding, and all the phase terminals are led to the circuit outlet. As a result, all the end windings are leading approximately 1/9 of the perimeter of the stator slot circle, as shown as a red circuit in Figure 3 -11. The radius of that circle is

$$r_p = r_r + r_{AG} + h_S \tag{3 - 1}$$

, where r_p is the perimeter of the red circle, r_r is the radius of the rotor, r_{AG} is the air gap length, and H_S is the height of the slot. As a result, the radius for the red circle is 67.36 mm. The perimeter is 423.20 mm. As it has been discussed, each coil takes 1/9 of the red circle perimeter, which makes the arc length between two phases A 47 mm.

For each coil, there are 115 turns with two paralleled paths, which means the end winding arc length for two slots on both ends is

$$L_A = 47 \ mm \times 115 \times 2 = 10,810 \ mm \tag{3 - 2}$$

As in this project the stator wire has been chosen to be 0.56mm (diameter) 24SWG copper wire, the resistance can be calculated by

$$R = \rho \frac{L}{S} \tag{3 - 3}$$

, where R is the resistance of the conductive material, ρ is the resistivity of the material, S is the cross-sectional area, and L is the length of the material. The end winding resistance between the two slots that are marked in Figure 3 -11 can be calculated as

$$R_{phase \ A} = 1.73 \times 10^{-8} \times \frac{10,810 \times 10^{-3}}{\pi \times \left(\frac{0.56 \times 10^{-3}}{2}\right)^2} = 0.76 \ Ohms \tag{3 - 4}$$

Because the two paths of phase A1 that are marked in Figure 3 -11 are parallel connected, the total resistance is 0.38 Ω. Further information concerning the end winding resistance has been given in Table 3.

In Table 3, phase A1 is one-third of phase A, which is utilized to be the fundamental unit of the end winding resistance. In the meantime, the resistance of the calculation and the resistance of the measured one has been compared to verify the calculation method.

Table 3: The end winding resistance for different parts of the stator

	Phase A1 end winding resistance (Ohms)	Phase A end winding resistance (Ohms)	Phase A resistance (Ohms)	Phase A resistance measured (Ohms)
Between four slots	0.38	1.14	2.1	2.02
To the circuit outlet	0.02	0.02	N/A	N/A
Total	0.4	1.16	6.3	6.06
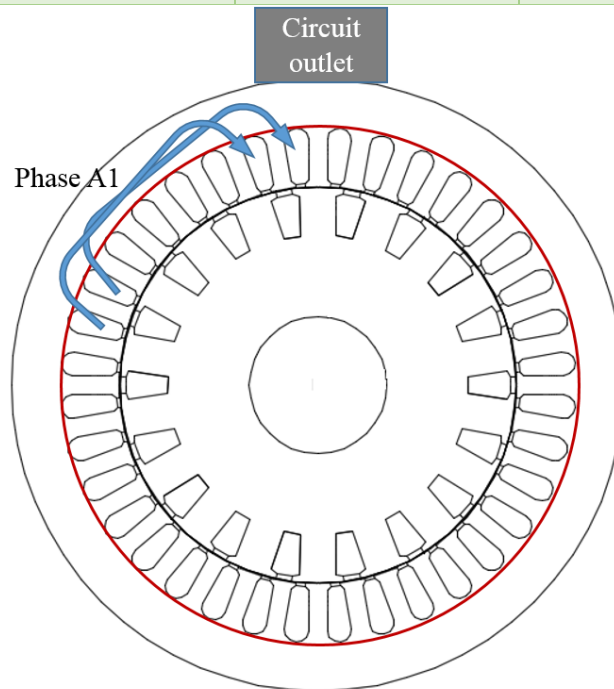
Figure 3 -11: The winding configuration of the conventional induction machine for the end winding calculation

3.4.2 The end winding reactance calculation

As it has been stated, the iron core has a significant impact on the reactance leakage, which makes the prediction highly inaccurate. Typically, according to [1] and many other textbooks, the reactance leakage can be calculated as

$$X_l = 4\pi f_1 \mu_0 \frac{N_1^2}{p} \times 0.47(I_E - 0.64\tau)$$

(3 - 5)

, where X_l is the end winding leakage reactance, f_1 is the stator voltage frequency, N_1 is the number of series connected conductors per phase, p is the number of pole pair, I_E is the average length of the end winding, and τ is the stator coil pitch. This formula contains an empirical correction factor of 0.47. Because the scale of the induction motor is lower than 10kW, the end

winding plays a relatively insignificant role in the motor operation. In this project, the end winding leakage reactance will be calculated with the above formula. However, the proposed motor has the potential to be manufactured to be a high-power motor based on the same principle. As a result, in this dissertation, some other researchers' developments in the high power machine area are also discussed.

As described in[2], the author finds that the inductance that is measured from the terminals of a coil with an iron core can be divided into seven parts, and each part is proportional to the width of the iron core except the end winding reactance. As a result, a 3D simulation and an experiment have been conducted with an air-core and iron core to measure the end winding inductance as seen in Figure 3 -12.
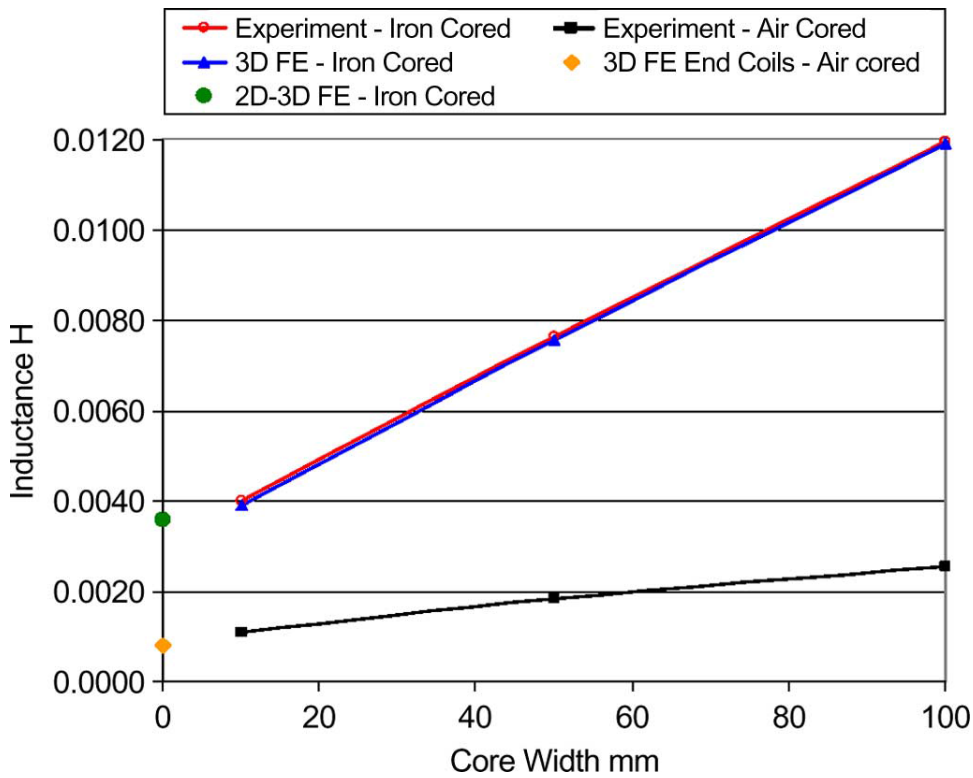
Figure 3 -12: The flux leakage of experimental and simulation results with iron and air-core respectively[2]

Because the end winding inductance is a constant if one extends backward the line, seen in Figure 3 -12, back to the point when core width is zero. The number of the cross point is the end winding inductance, as marked in Figure 3-12 with the green and the yellow point for iron core and air-core respectively.

On the other hand, [3] offered a new formula for calculating the end winding inductance,

$$L_w = \frac{Q}{amq}\frac{1}{a}(qN)^2\mu_0 l_w \lambda_w \qquad (3 \text{ - } 6)$$

, where Q is the slot number, a is the number of the paralleled path, q is the number of slot per phase per pole, m is the phase number, N is the number of turns, and μ_0 is the vacuum permeability. l_w is the average length of the end winding. λ_w is the permeance factor. The permeance factor can be calculated and deduced by [4]. In this method, the accuracy is approximately 92% of the value measured from the experiment. However, if compared to the 3D simulation, it is a time-efficient method.

However, the above method is only adopted when the machine is over 1000kW. For a small power motor, the influence of the end winding inductance is insignificant. As a result, in this project, the end winding inductance can be estimated by the empirical formula.

$$X_l = 4\pi \times 50 \times 4\pi \times 10^{-7} \times \frac{57^2}{3} \times 0.47 \times (47 \times 10^{-3} - 0.64 \times 41 \times 10^{-3})$$ $$(3 - 7)$$
$$= 8.34 \times 10^{-3}\Omega$$

As a result, the end winding reactance is $8.34 \times 10^{-3}\Omega$.

3.5 The simulation results of the conventional induction machine under fault condition

As the model has been tested for the torque ripple and connections, the reliability of the model under different conditions needs to be tested. The conventional induction motor winding connections determine that if one part of the machine is under open circuit or short circuit condition, depending on the state of the motor, the machine would cease to operate or overheat, causing damage to property and people. As the fault-tolerant synchronous machine is widely discussed and studied, the author attempts to use a similar idea of the stator in the induction machine due to the many similarities between the stators of those two types of machines.

The healthy condition simulation was conducted under voltage control with three voltage sources star-connected. The voltage has been set to a 400 V line to line RMS value; the frequency is 50 Hz. The rotor is a standard cage rotor with aluminum rotor bars and is shorted at all terminals. Further details have been shown in Table 1.

To simulate a one-phase open circuit condition, phase C has been deleted from the circuit in which the current in the stator becomes a single-phase current. Furthermore, the magnetic field in the air gap would not rotate. In this case, if the motor is still in the first place the winding would not be able to provide enough torque to start. However, the purpose of this simulation is to imitate the performance of a motor operated under the loss of one phase, which means the motor is rotating when the fault occurs. In this scenario, due to the changes of the magnetic

field in the air gap, the torque is reduced dramatically and the current increases to compensate for the loss of torque. If this operation continues, the motor would overload and finally overheated.

The simulation of the short circuit condition was conducted by shorting phase A and phase B. A short circuit between phases often occurs when the motor is rotating. In this situation, the current in Phase B and Phase A was highly distorted in amplitude and phase. As a result, the magnetic field would be unbalanced. Furthermore, the torque performance would be poor MMF in the air gap. In the meantime, the shorted circuit would produce a significant current which would burn the motor in a short time.

As to the inter-turn short circuit, the simulation is beyond the scope, due to the fact that the inter-turn short circuit would produce a very high short circuit current, and the situation can be completely different according to the number of turns shorted in a slot. Due to the complexity and the feasibility, in this project, the short circuit condition only refers to the short circuit between phases.
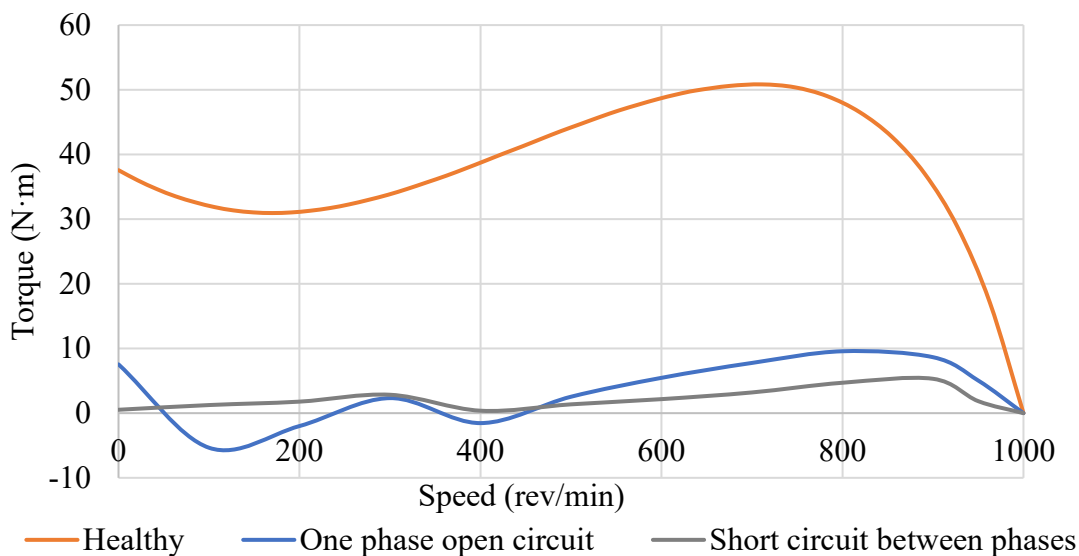
Figure 3 -13: The torque slip curve comparison of the conventional motor under healthy and fault conditions

As it can be seen in Figure 3 -13, the conventional induction machine performs poorly under the fault condition which includes the one-phase open circuit and short circuit between phases as expected. As the conventional three-phase induction machine under a one-phase short circuit equals to one-third of the power loss, to similarly compare the torque performance with the proposed model, the one-phase open circuit fault condition has been utilized here.

The torque under the rated speed has dropped from 22.1 N·m to 5.3 N·m in the one-phase open circuit condition and 4.1 N·m in the condition of the short circuit between two phases. As mentioned in the literature review, there are many studies of the fault-tolerant synchronous machine. In Figure 3 -14, the performances of a six-phase synchronous machine under healthy and two-phase open-circuit conditions at the rated speed can be seen. The model under the healthy condition has a mean torque of 0.33 N·m and under the two-phase open circuit condition, which is one-third of the power loss, the mean torque is 0.25 N·m, a decrease of 24.2%. Compared to the conventional induction machine, it dropped to 76%, which means the conventional induction machine can be optimized to be more fault-tolerant.
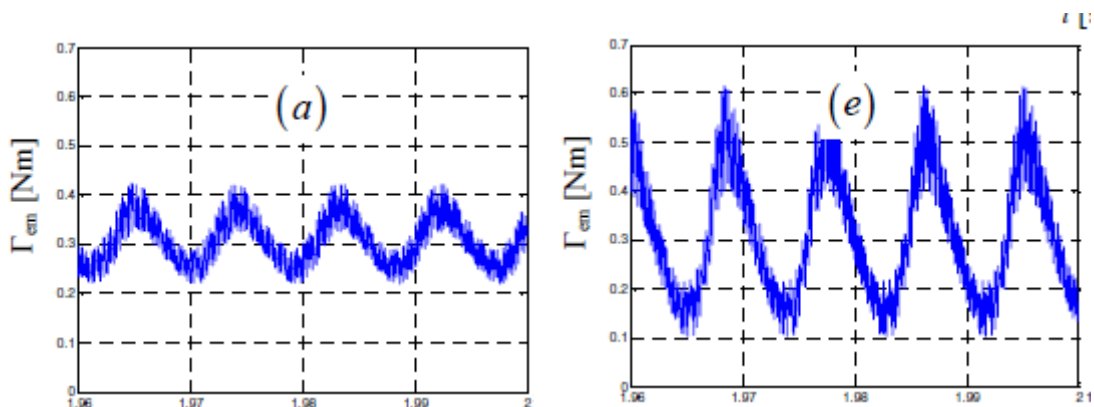
Figure 3 -14: The torque performance comparison between the healthy condition and the two-phase open circuit condition for a synchronous machine[5]

3.5.1 Mathematic calculation of the conventional induction motor operated under a one-phase open circuit

It is widely known that all rotating magnetic fields have a forward rotating H field and a backward rotating field. Regarding how to optimize the conventional induction machine to be more fault-tolerant, the rotating magnetic field has been studied. As shown in Figure 3 -15, the performance of the conventional induction machine under open circuit condition is considered poor. Discovering the reason behind this phenomenon could help to further improve the induction machine.

As a result, this section will focus on the mathematical reasons for the motor's performance. In this case, the phase which is under open circuit condition is assumed to be phase B, and the open circuit occurs to the power source, as shown in Figure 3 -15.
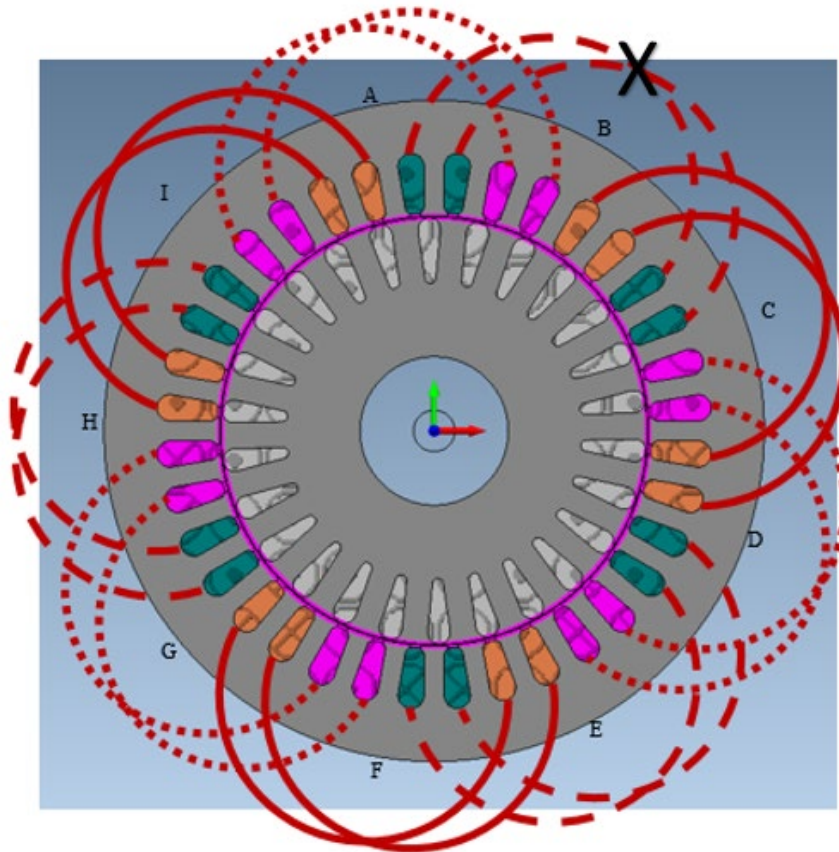
Figure 3 -15: The schematic diagram of the conventional induction machine under open circuit condition

Without phase B, the MMF of each phase can be assumed to be

Phase A: $\widehat{MMF}cos\theta\cos(\omega t)$

Phase B: $\widehat{MMF}\cos(\theta-120)\cos(\omega t-2\pi/3)=0$

Phase C: $\widehat{MMF}\cos(\theta-240)\cos(\omega t-4\pi/3)$

The combined MMF is

$$\widehat{MMF}cos\theta \cos(\omega t) + \widehat{MMF} \cos(\theta - 240) \cos(\omega t - 4\pi/3) \tag{3 - 8}$$

$$= \widehat{MMF}(cos\theta \cos(\omega t) + (-1/2\, cos\theta$$

$$- \sqrt{3}/2\, sin\theta)(- 1/2\, cos\omega t - \sqrt{3}/2\, sin\omega t))$$

$$= \widehat{MMF}(cos\theta \cos(\omega t)$$

$$+ (1/4\, cos\theta \cos(\omega t) + \sqrt{3}/4 cos\theta \sin(\omega t)$$

$$+ \sqrt{3}/4 sin\theta \cos(\omega t) + 3/4\, sin\theta \sin(\omega t)))$$

$$= \widehat{MMF}(5/4\, cos\theta cos(\omega t) + \sqrt{3}/4 cos\theta \sin(\omega t)$$

$$+ \sqrt{3}/4 sin\theta \cos(\omega t) + 3/4\, sin\theta \sin(\omega t))$$

$$= \widehat{MMF}\sqrt{3}/4 \sin(\theta + \omega t) + \widehat{MMF}\, 3/4 \cos(\theta - \omega t)$$

$$+ 1/4 \widehat{MMF}(\cos(\theta - \omega t) + \cos(\theta + \omega t))$$

The MMF can be calculated as

$$MMF = \frac{4}{\pi}\frac{3}{2}\frac{N\hat{I}}{P}k_p k_d \cos(\omega t - \theta) \tag{3 - 9}$$

, where the N is the number of turns per coil, $\hat{I}$ is the peak value of the current, k_p is the pitch factor, k_d is the distribution factor, and P is the pole pair number, this equation can be found in the EP textbook of Newcastle University.

As a result,

$$\widehat{MMF} = \frac{4}{\pi}\frac{3}{2}\frac{N\hat{I}}{P}k_p k_d = \frac{4}{\pi}\times\frac{3}{2}\times\frac{63 \times 12 \times 7.91}{3} \times 1 \times 0.966 = 3677.52A \tag{3 - 10}$$

In this case, the combined MMF is expressed by

$$MMF = 1592.41 \sin(\theta + \omega t) + 2758.14 \cos(\theta - \omega t) \tag{3 - 11}$$

$$+ 919.38 \cos(\theta - \omega t)$$

$$+ 919.38 \cos(\theta + \omega t) = 2720 \sin(\theta + \omega t) + 4794 \cos(\theta - \omega t)$$

This calculation has also been checked with MATLAB; the results have been shown in Figure 3 -16.
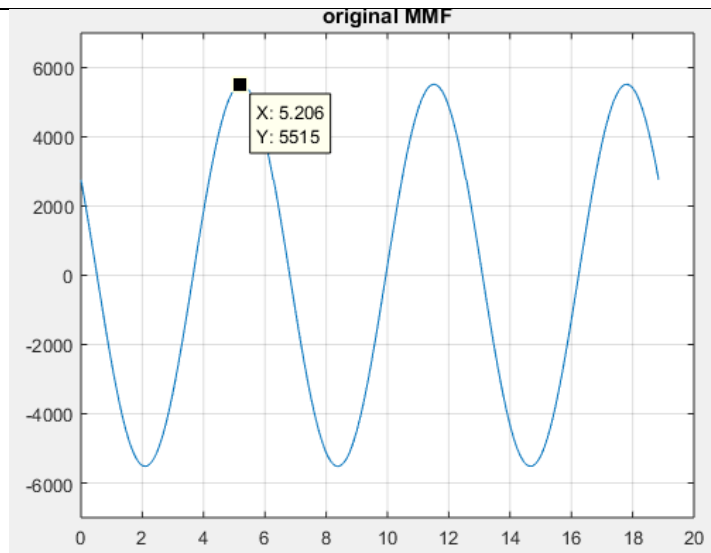
Figure 3 -16: The MMF obtained in MATLAB and the maximum of MMF

To collaborate with the results of the calculation and simulation, the maximum MMF for the calculated MMF has been obtained as seen in Figure 3 – 16.

The Maximum MMF is obtained at the condition of t = 0.01667, $\theta = 5.206\ rad$, in this case, the MMF can be calculated as

$$MMF = 2720 \sin(5.206 + 5.236) + 4794 \cos(5.206 - 5.236) \qquad (3 - 12)$$
$$= 721.4 + 4794 = 5515.4\ A$$

According to the results of MATLAB, the calculation has been proved to be correct. In this case, the positive direction of the stator rotating field MMF is considered to be 2720A, and in the negative direction is 4794 A.

Since

$$\widehat{H} = \frac{\widehat{MMF} \times n}{2r} \qquad (3 - 13)$$

, where r is the rotor radius, n is the pole pair number, and $\widehat{H}$ is the peak value of the magnet field strength.

As a result, for the positive direction,

$$\widehat{H} = \frac{2720 \times 3}{2 \times 0.517} = 7891.68\ A/m \qquad (3 - 14)$$

Moreover, for the negative direction,

$$\widehat{H} = \frac{4794 \times 3}{2 \times 0.517} = 13909.1\ A/m \qquad (3 - 15)$$

3.5.2 Complete machine simulation

In order to verify the simulation of the conventional induction machine has the appropriate performance, a complete machine has been simulated to check if the results are consistent with the half-machine simulation.

As seen in Figure 3 -17, the 'Healthy' curve represents the manufacturing data. The torque performance of the half-machine model and complete machine model in MAGNET has been compared with the manufacture data. Both simulations were conducted with a voltage-controlled circuit with a 50 Hz 400 V RMS voltage source. Each phase has been fed with one voltage source with no connection to other sources. From those two 2-D models, the simulation of model in both simulation models show significant similarities, which, although they are quite different while in the low-speed part, are believed to be induced by the nature of the induction machine. Due to the voltage control, the voltage of the model has been kept the same at all speeds. However, the current would rise during the speed reducing the process of the induction machine, as seen in Figure 3 -16. While the speed is reduced to a certain point where the back EMF is smaller than the total unwanted inductance including the end winding inductance, mutual inductance, and inductance leakage. In the circuit, the torque shall reduce due to the reduction of the back EMF, which is caused by the reduced efficiency and the inductance.
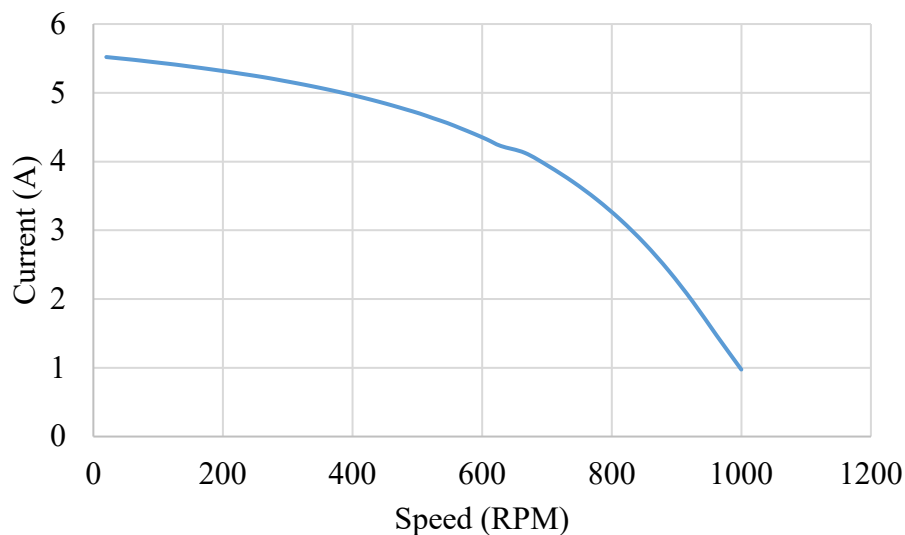
Figure 3 -17: The current speed curve of the conventional induction machine with voltage control

As the half model with odd boundary condition has been constructed in the early stage of the research, the end winding resistance and inductance has not been taken into consideration,

which caused the differences between two simulation torque-speed curves. The calculation of the end winding resistance and inductance will be shown in the last section.
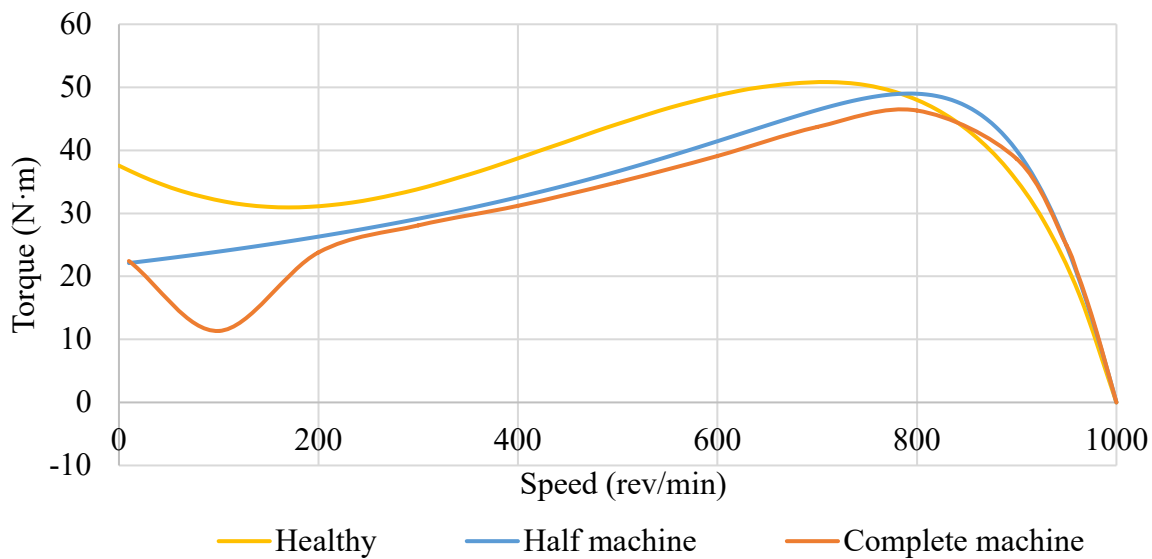
Figure 3 -18: The torque slip curve comparison between different models

In the meantime, it also can be seen that there are some differences between the manufacturing data and the simulation result. The reason might be that the end winding of the model is calculated based on the material and experience. On top of that, the rotor bars are skewed for 10 degrees in the manufacturing machine. In the 2D model, it is difficult to consider the skew effect. However, the skew effect will be discussed in the next chapter.

3.6 Conclusion

In this chapter, the conventional induction machine has been modeled according to an existing manufacturing model. At the start, the parameters of this model have been introduced, and by modifying the machine constructing script, the complete model of the conventional induction machine has been built. It has been found that the simulation takes a relatively long time to finish, a half model with odd boundary condition has been modeled to reduce the simulation time. In addition, the simulation condition and the winding configuration has been introduced as well. In the second part, some of the simulation parameters have been calculated such as the end winding resistance and inductance, in which some of the previous researchers' study and some empirical equations have been involved. In the last part, the model simulation for the half model, complete model, and the manufacture test data has been compared with each other, which finds the simulation results are accurate. In addition, the calculation of the positive and

negative rotating field furtherly confirm the torque performance and laid the ground field for further study of the induction machine performance under fault conditions.

All in all, this model has been checked and compared with the manufacturing data to verify the accuracy of the simulation model to set a baseline for the whole project. It demonstrates different winding connections and control methods for setting a foundation for the fault-tolerant induction machine study. In the meantime, some of the basic parameters have been calculated in order to assist in the understanding of the performance of the conventional induction machine. In the end, the torque-speed curves of different types of simulation models have been compared and discussed to prove the simulation results can be trusted.

3.7 Reference

1.   Bo Su, D.M., Analysis and Calculation of Stator End-leakage Reactance for Induction Motors with Low Harmonic Windings. 2013.

2.   Cox, T., F. Eastham, and J. Proverbs, End Turn Leakage Reactance of Concentrated Modular Winding Stators. IEEE Transactions on Magnetics, 2008. **44**(11): p. 4057-4061.

3.   Fang, Y., et al. Evaluation of stator end-winding leakage inductance of water filling induction motor equipped with two plane end-winding. in 2015 Tenth International Conference on Ecological Vehicles and Renewable Energies (EVER). 2015.

4.   Lin, R. and A. Arkkio, Calculation and Analysis of Stator End-Winding Leakage Inductance of an Induction Machine. IEEE Transactions on Magnetics, 2009. **45**(4): p. 2009-2014.

5.   Aroquiadassou, G., et al. Six-phase induction machine drive model for fault-tolerant operation. in Diagnostics for Electric Machines, Power Electronics and Drives, 2009. SDEMPED 2009. IEEE International Symposium on. 2009.

Chapter 4 Triple Three-phase Induction Machine

Multiphase machines are defined as those in which the number of phases is variable. Since three-phase systems are the minimum which has both constant input and output power, with only three connections, a multiple of three phases is often selected. As a result, the multiphase system in this project is composed of multiple three-phase subsystems and multiple three-phase inverters. Among all the multiphase machines, the triple three-phase machine is most exciting and proved to obtain more reliable and larger torque density [1]. It is composed of three three-phase inverters and three three-phase subsystems which develop a 120 degrees displacement to each other.

4.1 Fault-tolerant machine principle

For a long time, researchers have been seeking methods to create machine concepts with extra reliability and robustness. At the machine design level, most of them turn to the multiphase machine, a machine with more than three phases. In a three-phase system, if one of the phases is an open circuit, the current in the other two phases will be the same magnitude with 180 degrees of phase difference, assuming the machine is assembled as a star connection with no neutral point. However, the emergence of the multiphase machine has changed this situation. As explained in Chapter Two, when there is more than one set of three-phase systems, and a fault occurs in one, the remaining three-phase systems continue to operate and, if there is no coupling between systems, they are unaffected by the fault.

4.2 Triple three-phase induction machine topology

4.2.1 General topology

Above all, the multiphase machine reduces the cogging torque induced by the mutual inductance between the rotor and stator. Typically, the cogging torque is expected to be as small as possible because it would affect the performance of the machine in medium speed control and the accuracy of the machine in rotor position control. Subsequently, the fractional slot machine helps to weaken the amplitude of the tooth harmonics and improve the waveform of the electromotive force effectively. It also reduces the pulse amplitude of each pole flux caused by the variation of the air gap permeability and the pulse vibration loss on the surface of the stator conductor.

In this case, the triple three-phase induction machine is designed as three segments: each segment compromises one conventional three-phase fully pitched star-connected subsystem, and all segments are powered by three synchronized inverters. As can be seen in Figure 4 - 2, the model is split into three segments, each comprising two poles. Compared to a conventional overlapped winding, as seen in Figure 4 - 1, the three independent segments have no winding overlap between segments and are electrically, thermally, and physically isolated from each other, though continue to be coupled via the rotor. The machine stator is adapted from a standard three-phase induction machine stator. In order to flux density
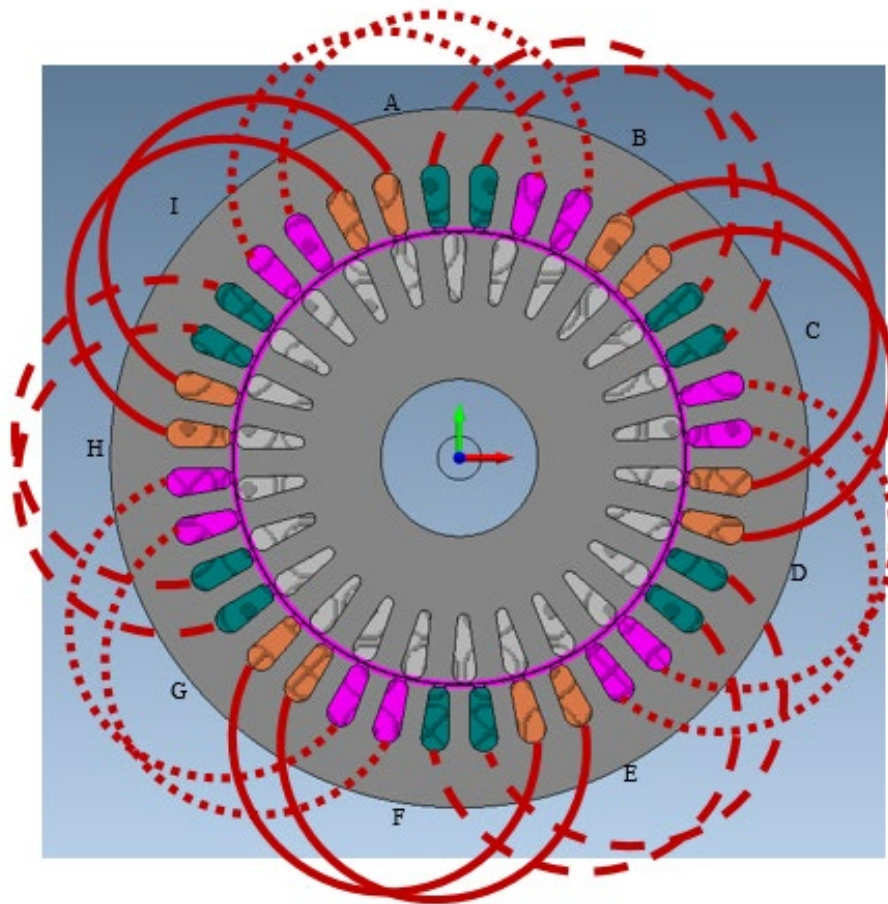
Figure 4 - 1: Conventional stator winding arrangement
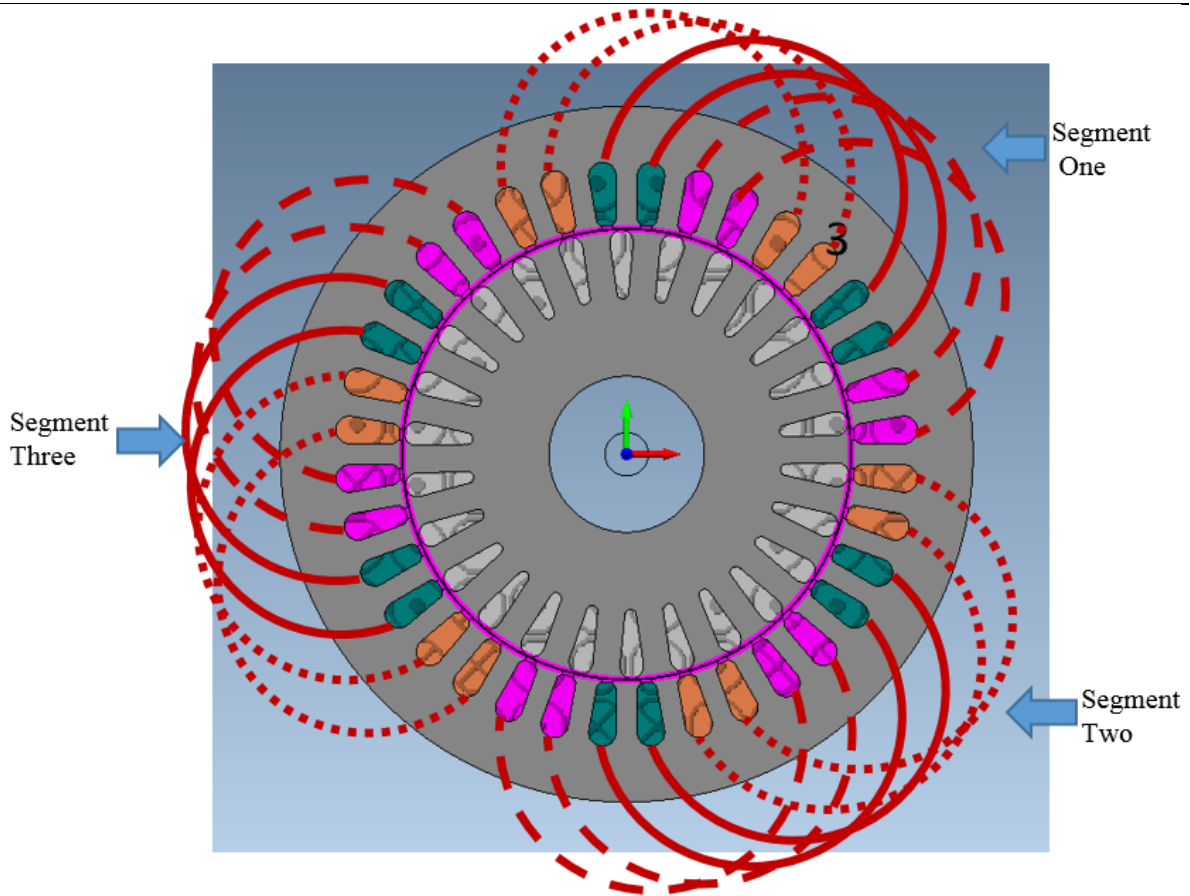
Figure 4 - 2: Fault-tolerant stator winding arrangement

4.2.2 The slots geometry

As seen in Figure 4 - 2, a standard cage rotor has been used at the beginning of the simulation. The cage rotor bar is aluminum and short-circuited on both ends. Moreover, the shape of the slots on both stator and rotor are rounded trapezoidal shapes with a semi-closed slot opening, as shown in Figure 4 - 3.
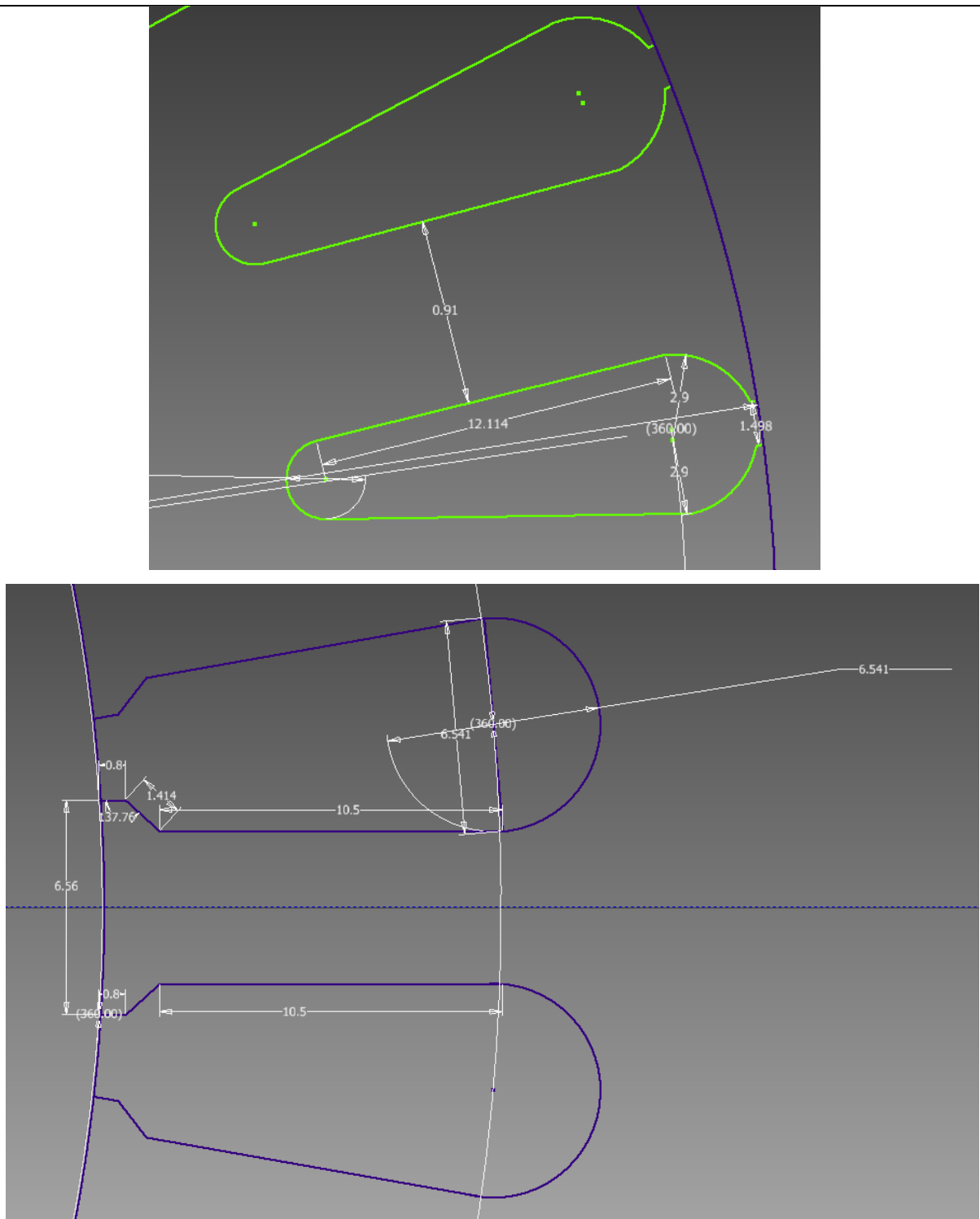
Figure 4 - 3: The specific parameters for the stator and rotor slots (Unit: mm and degree)

Generally, this slot shape would be chosen if the wire is round and the machine rating is relatively low (below 100 kW). This slot geometry is chosen because a smaller slot opening leads to a higher flux density in the air gap. With a certain stator MMF, the electrical magnetic pulse in the stator tooth would be small, which significantly reduces the core loss. However, too small of a slot opening will result in a higher magnetic field between the main body of the

slot and the edge of the stator/rotor, which will cause a higher inductance leakage and partial saturation.

4.2.3 The triple three-phase IM windings

Since the stator is adapted from an existing machine, the slot area and the number of slots are maintained. As seen in Figure 4 - 2, the conventional induction machine is wound with overlapping between phases. As mentioned in Chapter 3, under the open circuit fault, the MMF in the air gap periphery is not sinusoidal enough to provide the model with enough starting torque. However, the open circuit fault condition is hardly the most catastrophic fault in an induction machine. In the case of an inter-turn short circuit, the voltage input will induce a large current in the fault. The current will produce enough energy to burn through the insulation between the conductors. Consequently, due to the overlapping of the coils and the good thermal conductivity of the copper, the heat will spread around the whole machine and result in a complete breakdown.

To create an induction machine with more reliability, the windings of the stator have been redirected to a fully pitched, single-layer winding. In this scenario, the windings are reconfigured as three isolated three-phase subsystems, each powered by an isolated inverter.

As can be understood from Figure 4 - 4 and Figure 4 - 5, in both models, the current directions in each slot are unchanged, despite the changed winding configurations. Hence, if the amplitude of the current in each coil is sinusoidal AC, the MMF in the air gap is believed to be sinusoidal and 120º apart from each phase.
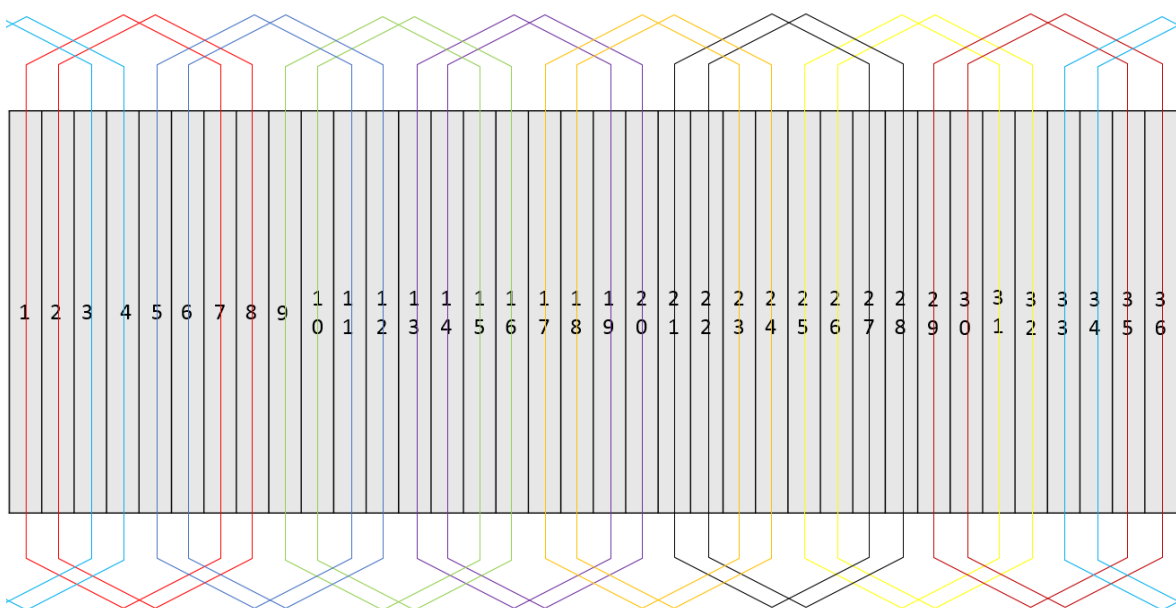
Figure 4 - 4: The conventional winding topology of the stator
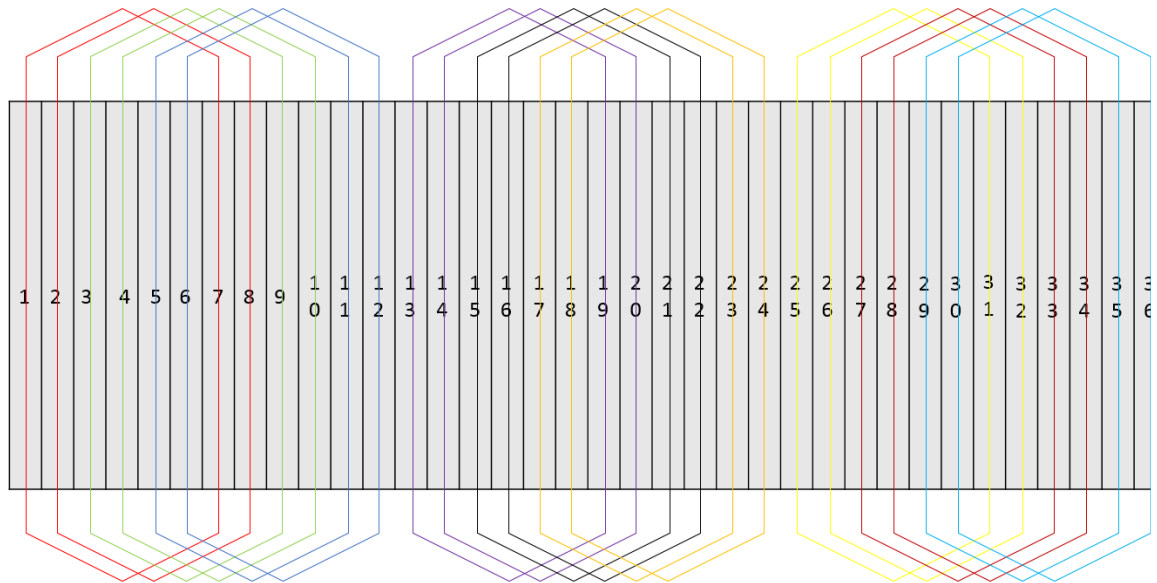
Figure 4 - 5: The triple three-phase winding topology of the stator

4.3 Triple three-phase induction machine performance analysis

4.3.1 Simulation environment

The triple three-phase induction machine is simulated with the help of FEA software (MagNet), with each subsystem connected in star-connection. The line voltage and frequency were decided according to the manufacturer's data, and relevant parameters are shown in Table 4

Table 4: The relevant parameters for simulation

Parameters	Value	Units
Line voltage (RMS)	133.33	Volts
Frequency	50	Hz
Stator end winding resistance (each subsystem)	5.52×10^{-2}	Ohms
Stator end winding inductance (each subsystem)	1.47×10^{-4}	H
Rotor end winding resistance	1.27×10^{-6}	Ohms

Number of turns	115	N/A

4.3.2 Simulation results when healthy

The performance of the proposed triple three-phase induction machine can be demonstrated simply by comparing the H field in the air gap, as shown in Figure 4 - 6.
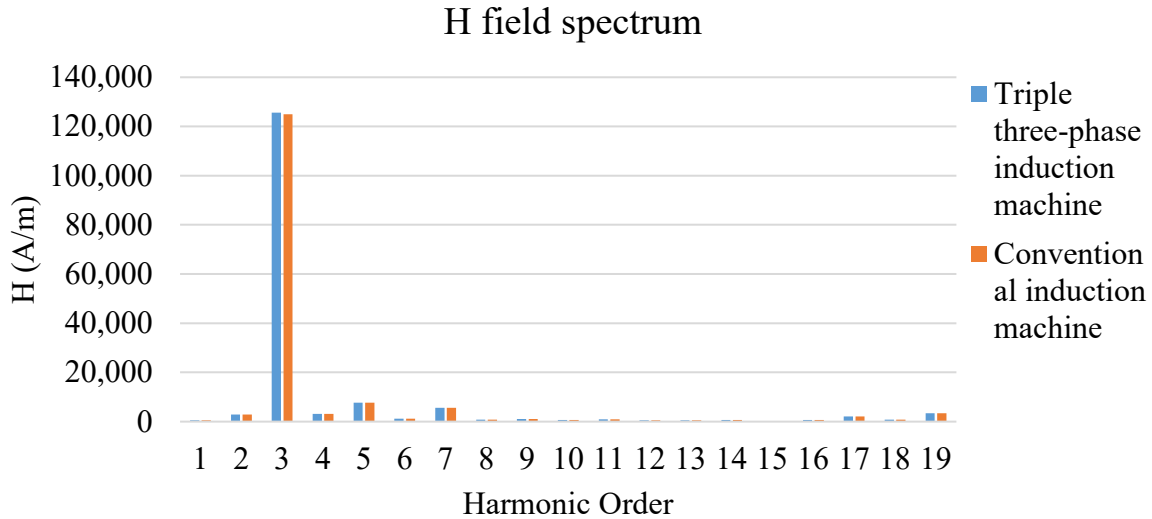
Figure 4 - 6: The H field spectrum for the conventional and the proposed induction machine

As can be seen in Figure 4 - 6, the fundamental H fields for both models are around 125000 (A/m), and the harmonics are small enough to ignore. To confirm the results, obtained from MagNet and MATLAB, are correct, a series of calculations of the H field for a conventional induction machine has been compared and shown below.

The magnetomotive force (MMF) can be presented as

$$MMF = \frac{\pi}{4}\frac{3}{2}\frac{N\hat{I}}{p}k_d k_p \cos(\omega t - \theta)$$

(4 - 1)

, where N is the number of turns per phase, $\hat{I}$ is the peak current in the stator winding at rated condition, p is pole pair number, and $k_d k_p$ are distribution factor and pitch factor respectively. According to Table 1 and Table 2, the N is

$$N = \frac{126 \times 36}{3} = 1512 \ (turns/phase)$$

(4 - 2)

$$\hat{I} = 5.6 \times \sqrt{2} = 7.91 \ A$$

(4 - 3)

Hence the MMF is

$$MMF = \frac{\pi}{4}\frac{3}{2}\frac{1512 \times 7.91}{3} \times 1 \times 0.966 \times \cos(\omega t - \theta) \tag{4 - 4}$$

$$= 4536.96 \cos(\omega t - \theta) \tag{4 - 5}$$

The H field can be presented as

$$\widehat{H} = \frac{\widehat{MMF} \times p}{2r} \tag{4 - 6}$$

, where r is the radius of the rotor.

As a result,

$$\widehat{H} = \frac{4536.96 \times 3}{2 \times 0.0517} = 131600 \, (A/m) \tag{4 - 7}$$

By comparing the analytical results and finite element numerical results, it has been found that the results of the fundamental harmonic obtained from the FEA software are 125566.5 A/m and 124938.6 A/m for the triple three-phase induction machine and conventional induction machine respectively, while the calculation result is 131600 A/m; the error is 4.58%. This error is believed to be caused by the end winding resistance because the valuation of end-winding is based on the empirical formula. As a result, the simulation has been proved to be correct based on the calculation results.

Besides the H field, the torque ripple has been studied as well.
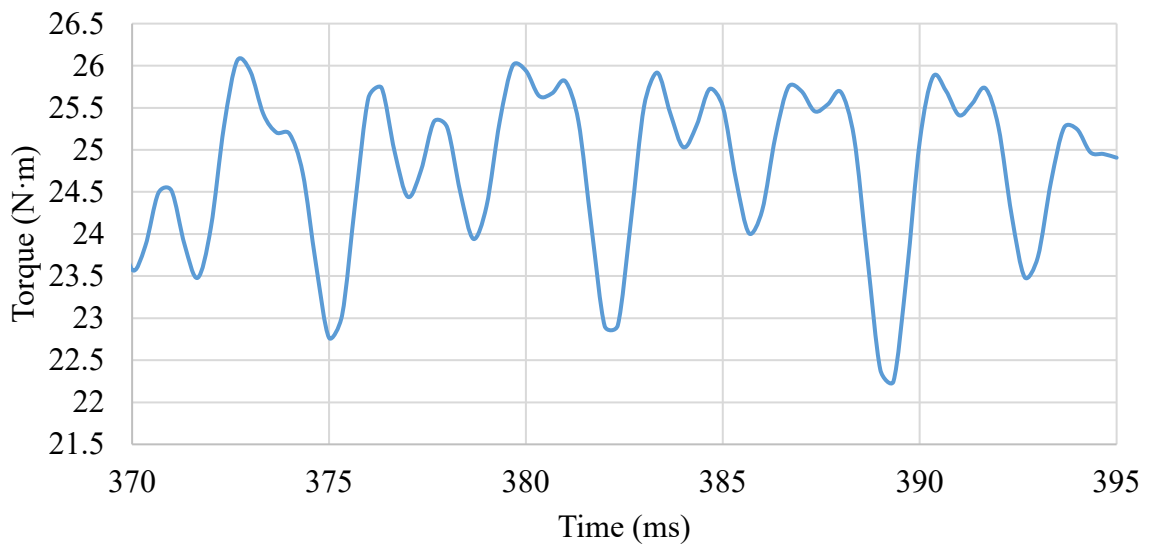
Figure 4 - 7: Finite element predictions of torque in the proposed model with a slip of 0.05 with voltage control 400 V 50 Hz

As seen in Figure 4 - 7, the maximum torque for the simulation is 25.9 N·m; the minimum is 22.2 N·m. As a result, the torque ripple of the rewinding machine is 3.7 N·m, the mean torque is 24.2 N·m, the torque ripple is 15.3%.

As the torque ripple is larger than expected, several methods have been taken to study this phenomenon.

a) The skew effect of the skewed rotor bar: it can be seen from the induction machine that the rotor bar of the induction machine has been skewed to reduce the torque ripple.

b) The accuracy of the FEA model, such as testing the best match for the maximum mesh length and the time step.

c) The machine's problem. In the manufacture data, there is no mark of the torque ripple; the induction machine could have had that problem from the beginning.

The first two possibilities are focused on here.

Firstly, for the possibility (a) four experiments have been done to choose the best match of mesh as well as "time step". The results have been shown in Table 5 and Table 6

Table 5: The investigation of the relationship between torque ripple and step length in 0.002 mesh

Steps per cycle	30	60	120	600
Mean torque	24.2	24.2	24.2	24.2
Maximum torque	26.4	26.3	26.1	26.1
Minimum torque	22.9	22.4	22.5	22.7
Torque ripple	3.5	3.9	3.6	3.4
Torque ripple (%)	14.5%	16.1%	14.9%	14.1%

Table 6: The investigation of the relationship between torque ripple and step length in 0.001 mesh

Steps per cycle	30	60	120	600
Mean torque	24.2	24.2	24.2	24.2
Maximum torque	26.3	26.1	26.1	26.1

Minimum torque	22.9	22.3	22.6	22.6
Torque ripple	3.4	3.8	3.5	3.5
Torque ripple (%)	14.1%	15.7%	14.6%	14.6%

As shown in Table 5 and Table 6, changing the mesh size does not have a significant impact on the torque ripple, with similar conclusions for the time step length. As the simulation with smaller meshes and shorter step length takes significantly more time in simulation and the differences between each scenario are much less significant, it is concluded that the scenario of 120 steps per cycle and a maximum mesh size of 0.002 m is a sensible compromise.

As 3D simulation takes a substantial amount of time, the concept of modeling skew effect in a 2D model comes into being. There are several methods of modeling the skew effect in a 2D model, such as 2D N-slice modeling and extruded modeling. In this research, N-slice modeling has been considered.

Figure 4 - 10 is an N-slice model for an induction machine which is duplicated n times in the Z direction. In that way, the motor is composed of n slices, and each of them has a thickness of L/n, where L is the stack length of the induction machine. Figure 4 - 8 shows a method to accomplish the N-slice model in MagNet.
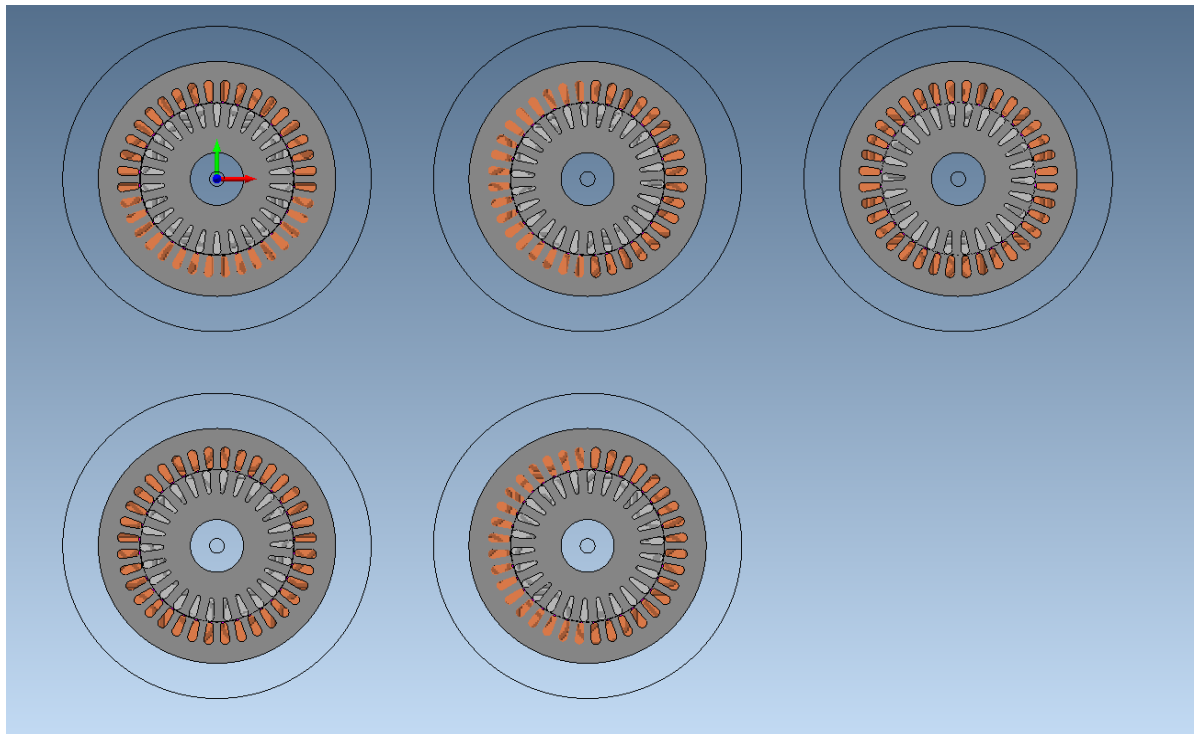
Figure 4 - 8: An N-slice model of conventional induction machine in FEA software

In this case, as shown in Figure 4 - 9 between each slice the rotor position is twisted by α/n, where α is the skew angle of the whole machine. The winding of the stator and the rotor bar of each slice are connected in series to make sure all the slices obtained the same current as in practice. In this way, the line current can be assumed to be continuous.
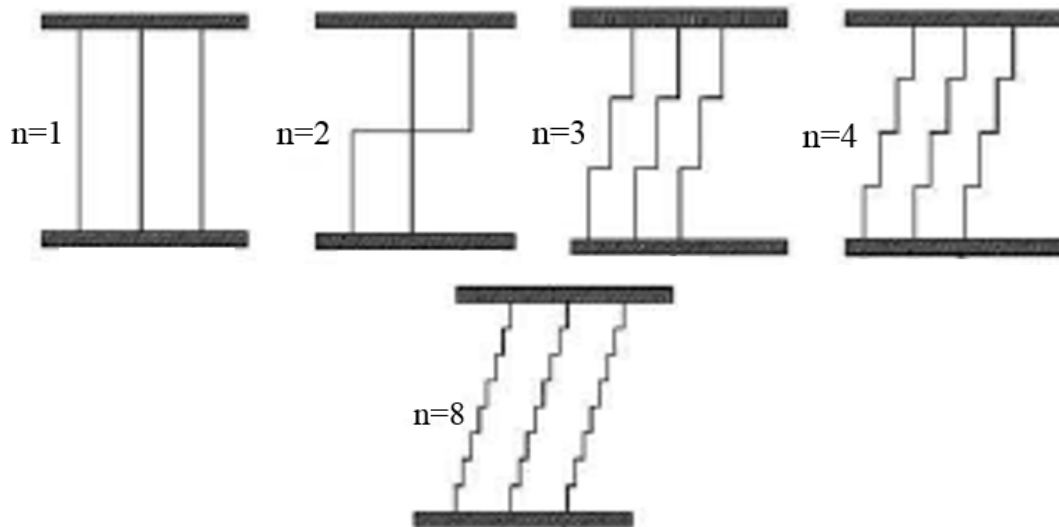
Figure 4 - 9: The schematic of the skewing when n=1,2,3,4,8
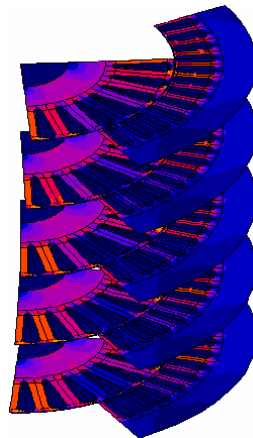
Figure 4 - 10: The schematic diagram of modeling the skew with n slice model [1]

The effect of the skewed rotor bars has been shown in Table 7, the variation of the torque ripple has been displayed, and in Figure 4 - 12, the torque ripple without skewed rotor and the one with skewed rotor have been assembled into one picture to demonstrate the differences. The spectrums of the simulation with the skew effect have been shown in Figure 4 - 11. All further results of torque analyzation, H field spectrum, and voltage comparison are obtained from the model with 10 degrees skewed rotor. The simulation model is voltage controlled, and the voltage is star connect to eliminate the impact of the triple harmonics.
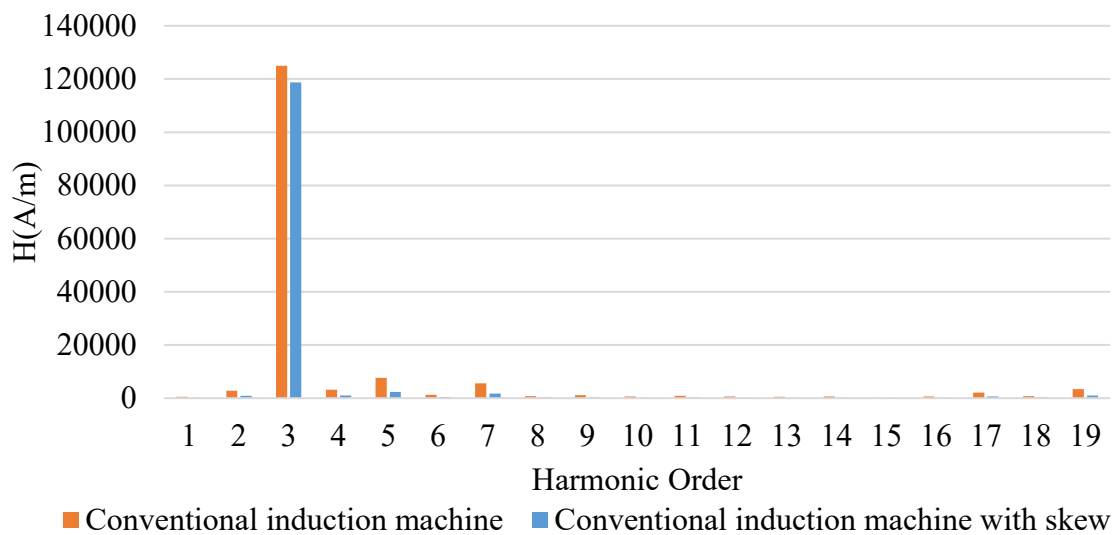
Figure 4 - 11: The spectrum of the induction with skew effect
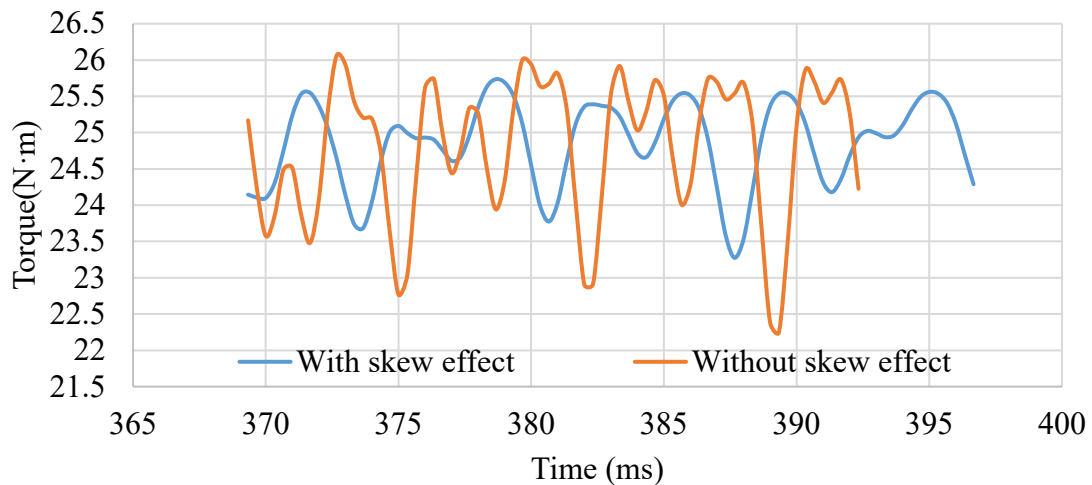
Figure 4 - 12: Torque ripple comparison before and after skew with voltage control

400volts 50Hz

It can be seen from Figure 4 - 13; there are some ripples to prevent the current from being sinusoidal. However, with the help of the skew effect, the current is smoother in the peak area, which indicates that the skew effect removes some harmonics in the current, by which reducing the torque ripple, as seen in Figure 4 - 14.
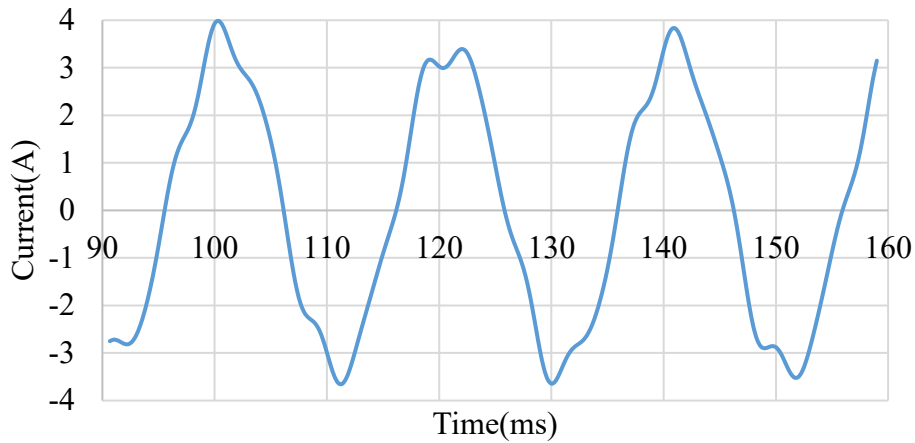
Figure 4 - 13: The current waveform of the induction machine without the skew effect with voltage control 400Volts 50Hz
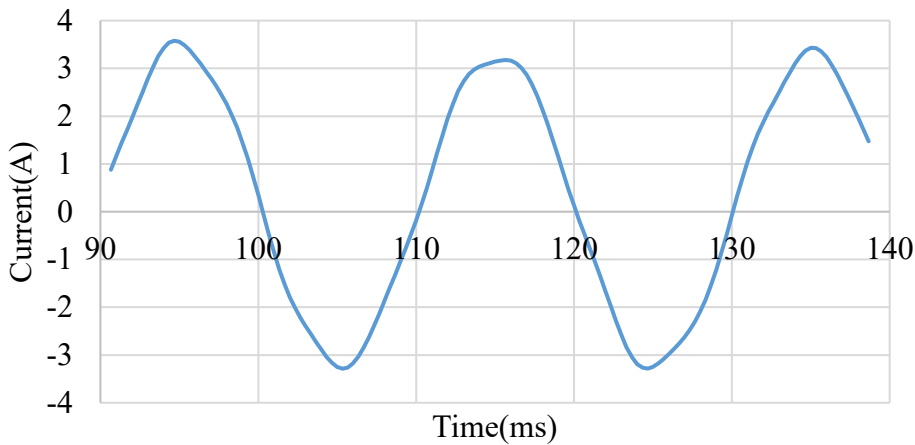
Figure 4 - 14: The current waveform of an induction machine with a skew effect with voltage control 400Volts 50Hz

Table 7: The comparison of induction with and without skew effect

	Mean Torque	Torque ripple
Without the skew effect	24.21 N·m	3.74 N·m (15.4%)
With skew effect(5º)	24.22 N·m	3.1 N·m (12.8%)
With skew effect(10º)	24.21 N·m	2.8 N·m (11.6%)
With skew effect(15º)	24.22 N·m	3.1 N·m (12.8%)

As a result, as seen in Table 7, the skew effect has been studied proving that it has a positive effect on the torque ripple, and comparing the skewed angle, it has been found that skew the rotor bars for 10º gives the least torque ripple. It should be noted that the n-slice mode still takes significant time to simulate. As a result, the simulation beyond this point will not apply the skew effect on it. In practice, the model where this research araised has skewed in the rotor as

well, however, the physical skew angle is not able to measured anymore due to the dissembled rotor, the skew can be speculated as 10 degree, which is one stator slot in this project.

4.3.3 The simulation results under open-circuit fault condition

As has been mentioned, the induction machine has been separated into three thermally, electrically, and physically independent segments. In this section, the primary purpose is to test the performance of the machine operating with one segment in the open circuit condition. Figure 4 - 15 shows the torque performance at s=0.05. Compared to the torque when it operates under a healthy condition with the same power input and same slip, the mean torque falls from 23.6 N·m to 12.25 N·m, which is 51.9% of the original. Moreover, the maximum torque of the in 200ms is 15.54 N·m; the minimum is 10.29 N·m, which means the torque ripple from peak to peak is 5.25 N·m and 42.8% in percentage.
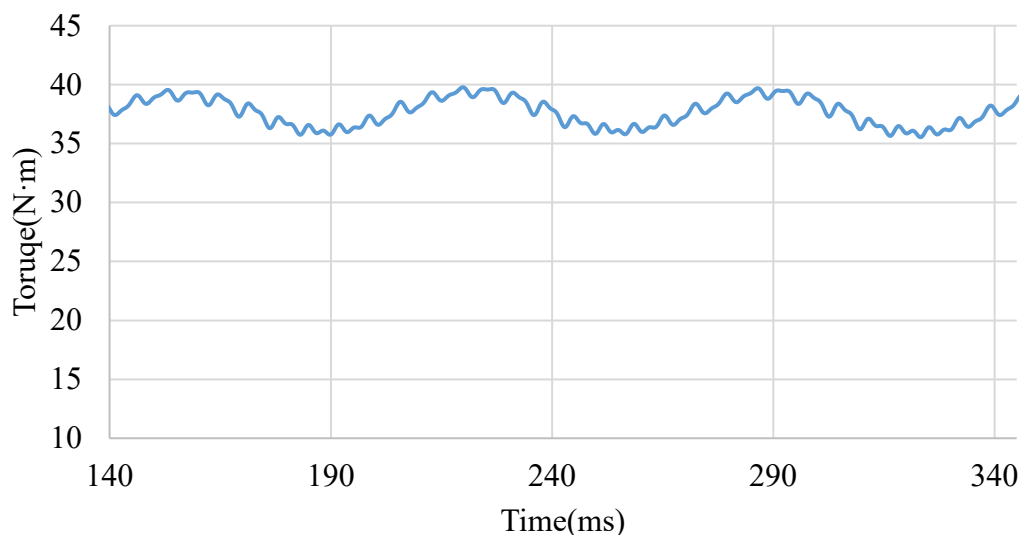
Figure 4 - 15: Torque performance at s=0.05 under one segment fault condition

The simulation results of the torque slip curve have been shown in Figure 4 - 16. It should be noted that the simulation of the triple three-phase induction motor with a cage rotor has been simulated with three 50 Hz current sources of 5.6 A (RMS value) for convenience of further comparison with the proposed motor. The sources and motor phases are star-connected. The open-circuit has been achieved in the same method shown in Chapter 3 in the fault operation for the conventional induction machine.
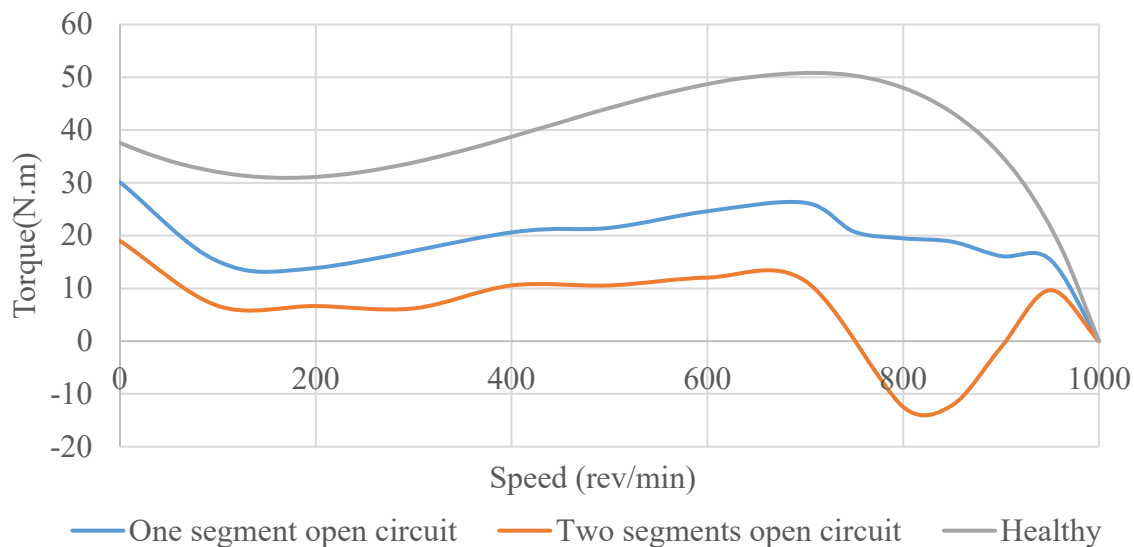
Figure 4 - 16:The torque-speed curve for the model working under healthy, one and two lanes open circuit fault with 5.6 A current control 50 Hz

As can be seen in Figure 4 - 16, the stator has been rewound into a triple three-phase induction machine and the model under the two fault conditions as well as the healthy condition. Compared to Figure 3 – 13, the performance is much better. However, it still shows some abnormal performance, especially the condition of two segments open circuit performs poorly particularly in the speed range of 750 rpm to 850 rpm when the torque is negative. This is clearly not useable in practice.

To furtherly study the reasons for this phenomenon, a perfect sinusoidal wave has been generated between two flat zero lines. Each of them occupies 360 electrical degrees to represent the spatial MMF around the rotor in the air gap, which has been shown in Figure 4 - 17. In this way, the MMF is imitated for the triple three-phase induction machine under the idealized fault condition.
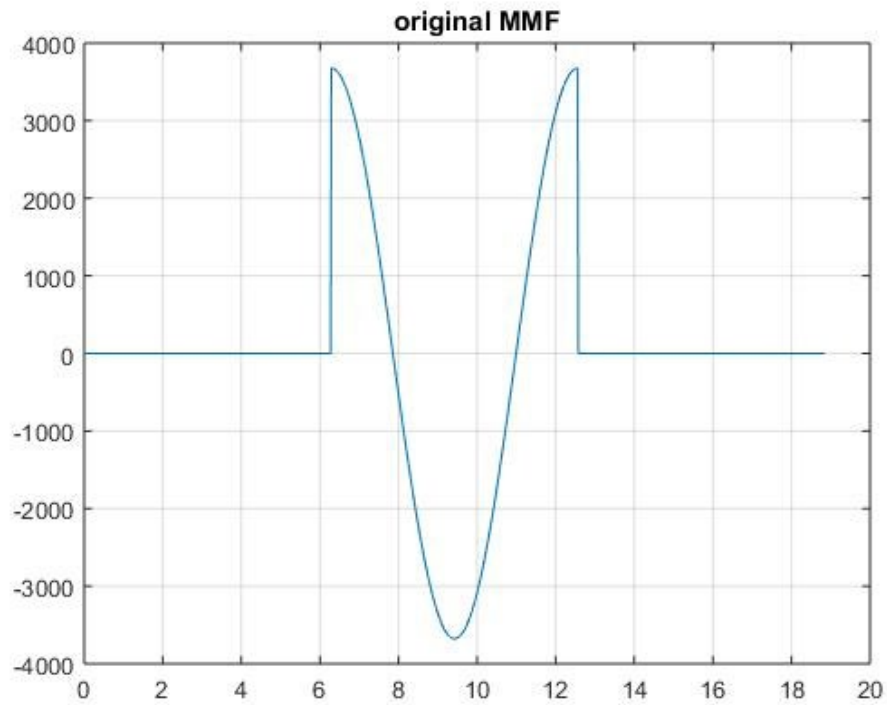
Figure 4 - 17: The ideal MMF generated in MATLAB (x-axis: Electrical angle(rad), y-axis: MMF(A/m))

Usually, the MMF in the real motor will include the slot harmonics and other phase belt harmonics. Regardless of all those harmonics, more attention can be paid to the harmonics that are responsible for this phenomenon.

FFT is applied to the MMF waveform using the formula

$$\widehat{H} = \frac{\widehat{MMF} \times n}{2r} \tag{4 - 8}$$

, where n is the number of the pole pair and r is the rotor radius. The H field is shown in Figure 4 - 18.
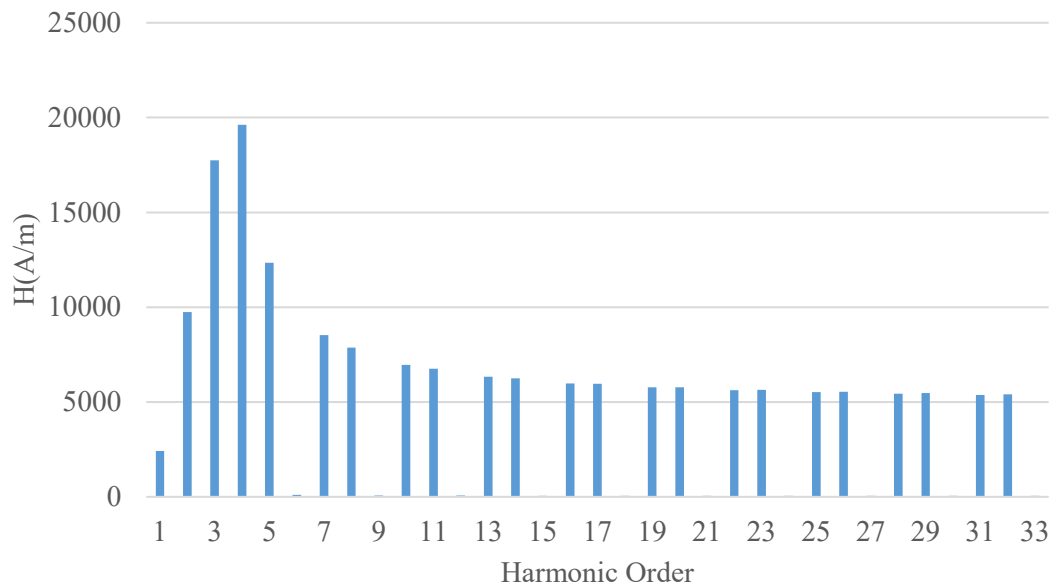
Figure 4 - 18: The H field spectrum for the perfect sinusoidal wave

As it can be seen in Figure 4 - 18, there are 2nd, $4^{th,}$ and 5th space harmonics present in the harmonic spectrum, it is postulated that these harmonics are the reason for the distorted torque slip curve with only one three-phase segment operational. In order to understand each harmonic's contribution to the torque performance, the current sheet model has been introduced.

4.4 The triple three-phase induction machine optimization

4.4.1 Space harmonic under the two segments open circuit condition

As it has been mentioned that in Chapter 3, there are two directions for the rotation of the H field in the air gap. As a result, the FFT results of H, which has been shown in Figure 4 - 18, can be expressed in equations. Those equations would help to further study the performance of the triple three-phase induction machine.

Table 8 The MMF FFT results of the two segments open circuit condition(per unit)

		t=0 s	t=0.0025 s	t=0.005 s
1 pole pair	a_n	0.1012	0.07217	0
	b_n	0	0.2179	0.3085
2 pole pair	a_n	-0.33	-0.3481	0
	b_n	0	-0.2354	-0.4943
3 pole pair	a_n	0.5	0.35	0
	b_n	0	0.35	0.5

4 pole pair	a_n	-0.4741	0.3382	0
	b_n	0	-0.2475	-0.3555
5 pole pair	a_n	0.26	0.1855	0
	b_n	0	0.1085	0.1573
6 pole pair	a_n	0	0	0
	b_n	0	0	0
7 pole pair	a_n	0.1446	-0.1031	0
	b_n	0	-0.04142	-0.06152
8 pole pair	a_n	0.1266	0.08603	0
	b_n	0	0.03045	0.04587
9 pole pair	a_n	0	0	0
	b_n	0	0	0
10 pole pair	a_n	-0.09076	-0.06473	0
	b_n	0	-0.01714	-0.02688

As seen in Table 8, the FFT results of different space harmonics have been obtained from MATLAB. As the frequency of the stator is 50 Hz, the rotation speed of stator MMF is 20 ms for one revolution. As a result, the 0.0025 s is 1/8 of one revolution and 0.005 s is the 1/4 of one revolution. As the results are from FFT, the MMF of 1 pole pair space harmonic can be expressed as

$$F_1(\theta) = 0.1012 cos\omega t cos\theta + 0.3085 sin\omega t sin\theta \qquad (4 - 9)$$

The positive rotation and negative rotation of the 1 pole pair space harmonic should be able to express as

$$F_1(\theta) = C_1 \cos(\omega t - \theta) + C_2 \cos(\omega t + \theta) \qquad (4 - 10)$$
$$= C_1 cos\omega t cos\theta + C_1 sin\omega t sin\theta + C_2 cos\omega t cos\theta - C_2 sin\omega t sin\theta$$
$$= (C_1 + C_2) cos\omega t cos\theta + (C_1 - C_2) sin\omega t sin\theta$$

Comparing to (4 - 9), the constant should be calculated as

$$\begin{cases} C_1 + C_2 = 0.1012 \\ C_1 - C_2 = 0.3085 \end{cases} \qquad (4 - 11)$$
$$\begin{cases} C_1 = 0.205 \\ C_2 = -0.1012 \end{cases}$$

As a result, the expression of the 1 pole pair harmonic can be expressed as

$$F_1(\theta) = 0.205 \cos(\omega t - \theta) - 0.1012 \cos(\omega t + \theta) \qquad (4 - 12)$$

Similarly, the 2 pole pair harmonic can be expressed as

$$F_2(\theta) = -0.4122\cos(\omega t - 2\theta) + 0.08215\cos(\omega t + 2\theta) \tag{4 - 13}$$

The 3 pole pair harmonic can be expressed as

$$F_3(\theta) = 0.5\cos(\omega t - 3\theta) \tag{4 - 14}$$

The 4 pole pair harmonic can be expressed as

$$F_4(\theta) = -0.4148\cos(\omega t - 4\theta) + 0.0593\cos(\omega t + 4\theta) \tag{4 - 15}$$

The 5 pole pair harmonic can be expressed as

$$F_5(\theta) = 0.2087\cos(\omega t - 5\theta) + 0.05135\cos(\omega t + 5\theta) \tag{4 - 16}$$

The 6 pole pair harmonic can be expressed as

$$F_6(\theta) = 0 \tag{4 - 17}$$

The 7 pole pair harmonic can be expressed as

$$F_7(\theta) = 0.1031\cos(\omega t - 7\theta) - 0.2477\cos(\omega t + 7\theta) \tag{4 - 18}$$

The 8 pole pair harmonic can be expressed as

$$F_8(\theta) = 0.08324\cos(\omega t - 8\theta) + 0.03737\cos(\omega t + 8\theta) \tag{4 - 19}$$

The 9 pole pair harmonic can be expressed as

$$F_9(\theta) = 0 \tag{4 - 20}$$

The 10 pole pair harmonic can be expressed as

$$F_{10}(\theta) = -0.05882\cos(\omega t - 10\theta) - 0.03194\cos(\omega t + 10\theta) \tag{4 - 21}$$

It can roughly understand that the second, fourth, and fifth space harmonics are relatively high. However, there are two parts of the MMF expression of each harmonic, the real effect of this harmonic upon the rotor can not be revealed. As a result, by utilizing the MMF for each harmonic, the current sheet model would help to intuitively observe the effect of each harmonic to focus on the limitation of the triple three-phase induction machine.

4.4.2 The current sheet model establishment

The current sheet model is a model with a standard induction machine cage rotor, which possesses the same specification with the machine in practice. However, instead of using the slotted stator, a sheet of current has been utilized to distribute around the stator bore. Each of the surface element has been assigned with a current and a phase angle corresponding to each space.

The surface element has been assigned to be copper without electrical resistance, also known as a superconductor. To make sure the results are reliable, the outside surface boundary condition has been set to tangential the same as the iron core-back to make sure there is no flux leakage from this side of the machine. The air-gap between the current sheet and the cage rotor has been kept the same as the previous model. In terms of the current that been assigned to the current slot has been calculated as below

$$I = \frac{H_t}{N_{coil}} 2\pi r \tag{4 - 22}$$

, where the I is the current that been assigned to the current slot, H_t is the tangential flux intensity, N_{coil} is the number of current-slot that has been placed in the current sheet. With this method, the amplitude of the current can be calculated. As to the phase angle, the initial angle can be set to the angle obtained from the FFT analysis, in which the H_t in different harmonics can be obtained as well.

With this model, it is possible to produce accurate MMF in the air gap without including the slot harmonics. The current sheet model is shown in Figure 4 - 19. (The script for the generation of the current sheet and applying current to each current slot will be attached to the appendix)
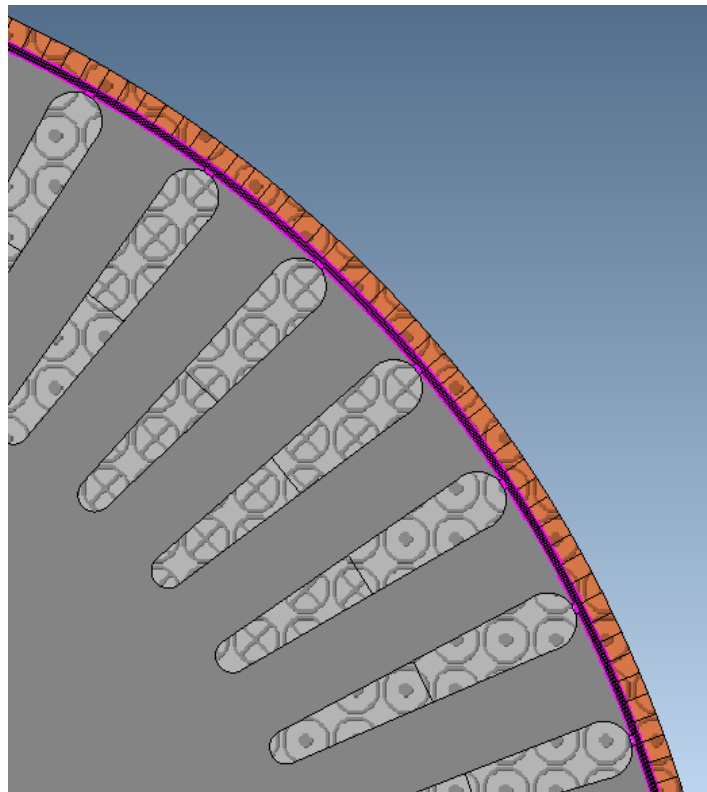
Figure 4 - 19: The current slot of the current sheet model
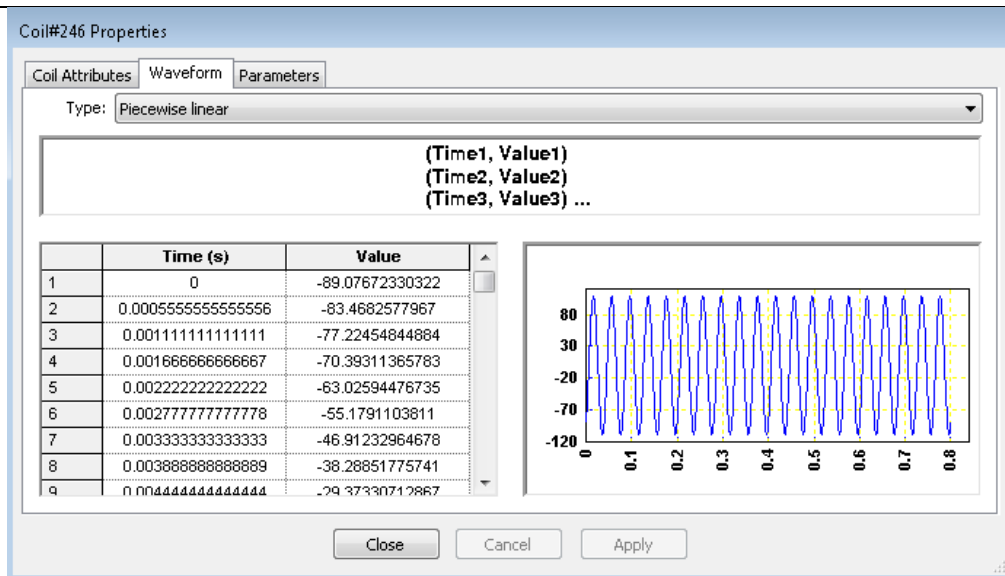
Figure 4 - 20: The current assignment system of the current sheet model

4.4.3 The performance of each harmonic under the two lanes operation

With the help of the current sheet model, each harmonic's contribution to the torque performance has been studied and organised into one figure. Because the synchronous speed is different for different harmonics, the simulation results for the harmonics cannot be simply added upon each other. For instance, the beginning of the torque slip curve for the fourth harmonic is at the synchronous speed for the 4th harmonic, which is 750 rpm.

Therefore, the entire torque slip curve for the harmonics between first and tenth has been shown in Figure 4 - 21.
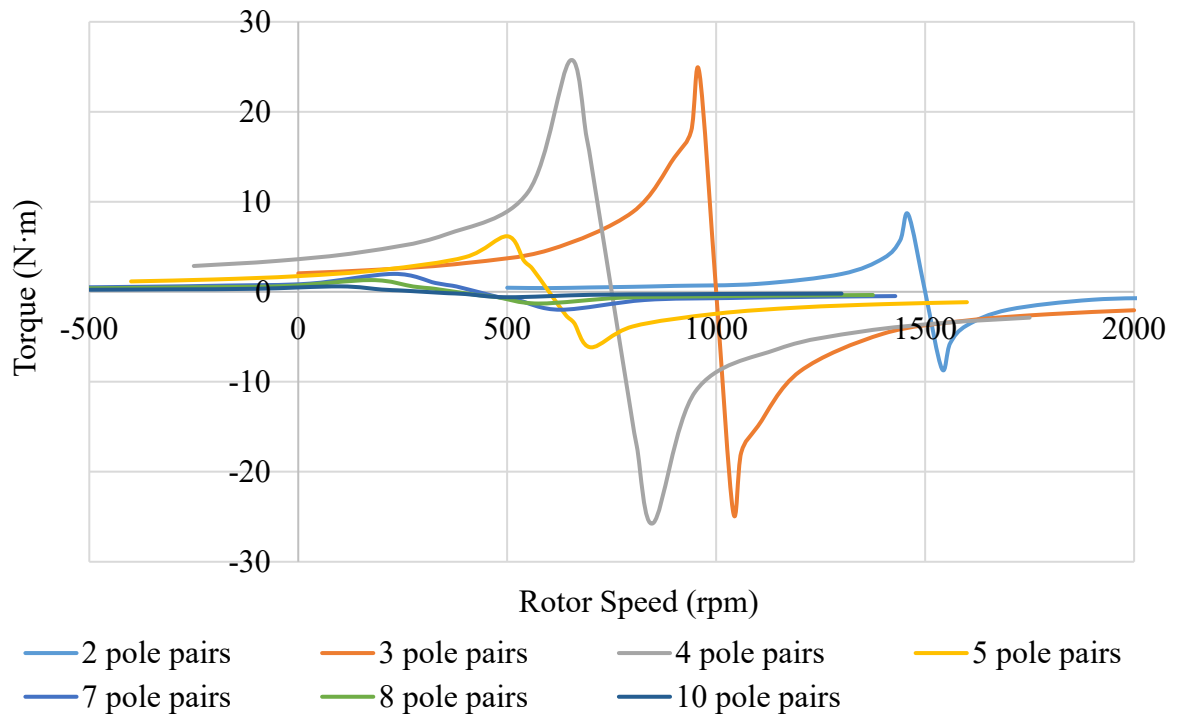
Figure 4 - 21(a): The torque slip curve for harmonics from first to tenth
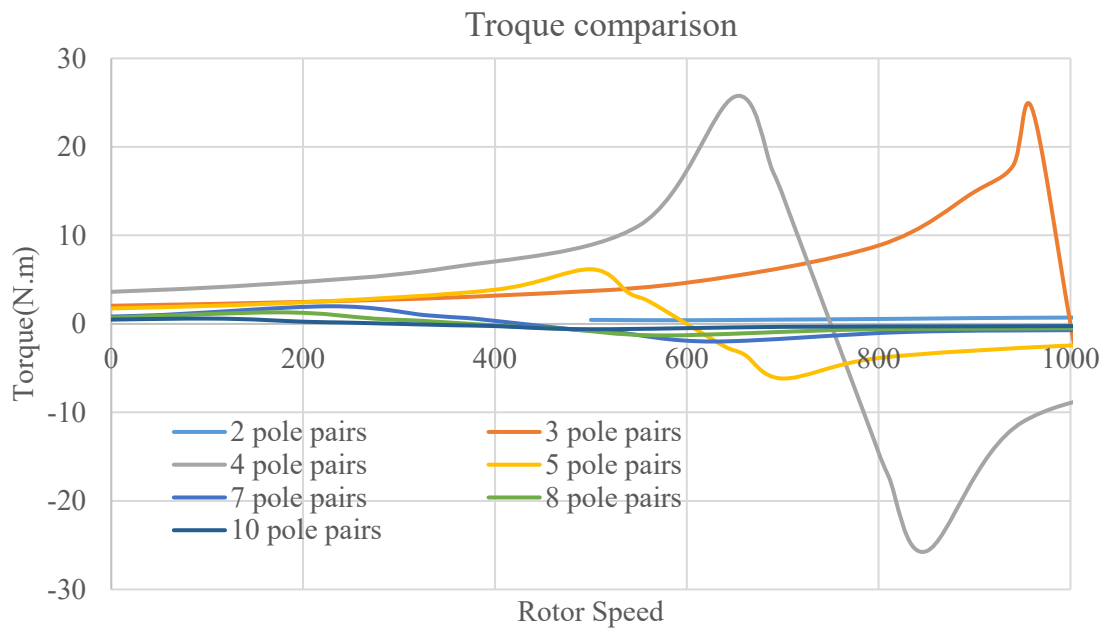
Figure 4 - 22(b): The torque slip curve for harmonics from first to tenth

For this method only utilized to discuss the torque performance during 0 to 1000 rpm as it is the practice speed range for this machine, Figure 4 – 21(a) can be simplified to Figure 4 – 21(b). Since any MMF harmonics can be decomposed into a sine wave with a forward rotation and a reverse rotation, each harmonic in Figure 4- 21(b) has two parts. Take the 4 pole pairs harmonics as an example. Between the 0 to 750 rpm, it provides positive torque to the machine torque performance, this torque is provided by the forward rotation sinewave of the 4 pole pair

harmonic. On the other hand, the negative torque between 750 rpm to 1000 rpm is provided by the reverse rotation sine wave from the same harmonic.

It can be seen that the grey line which is the four pole pair harmonic (also known as fourth spatial harmonic) contributes to the positive torque before 750 rpm but provides a substantial negative torque between 750 rpm and 1000 rpm. In addition, the five pole pair harmonic also provides a negative torque between 600 and 1000 rpm. In contrast, the second harmonic, whose maximum torque is small, provides all positive torque from zero rpm to 1000 rpm. As a result, the fourth and fifth harmonic are the ones responsible for the poor torque behaviour for the motor operating with one lane, especially during the speed range 750 rpm to 1000 rpm.

In order to ensure the veracity of the simulation, all the above torque slip curves have been added up and compared to the model working under the above situation; the result has been shown in Figure 4 - 22.
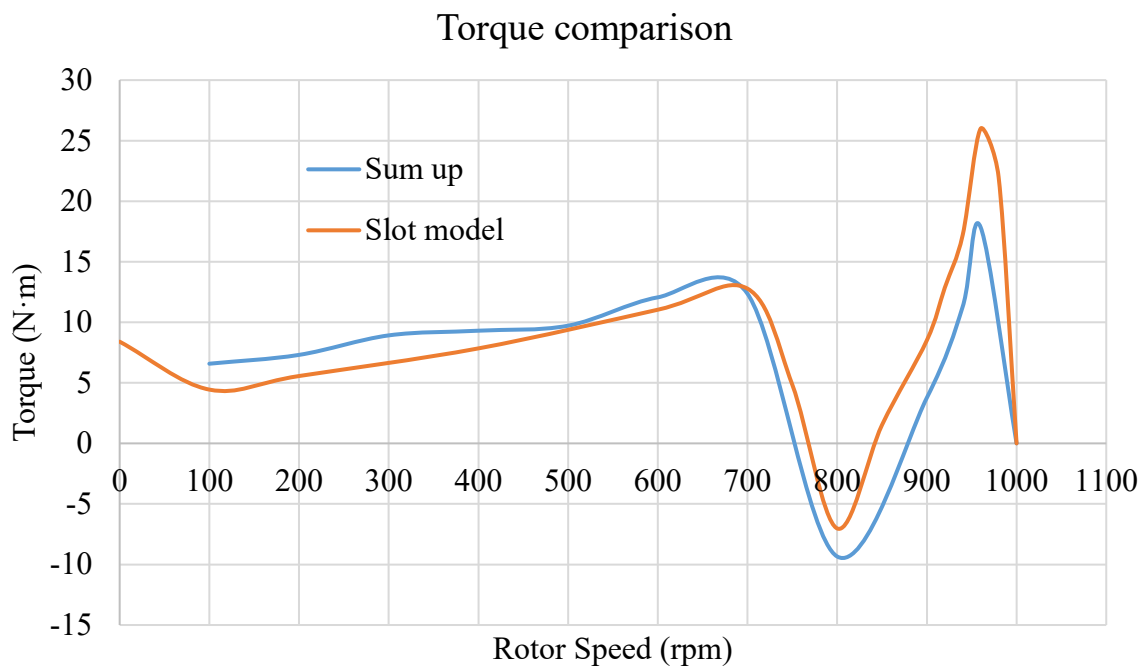
Figure 4 - 23: Torque comparison between the sum of the spatial components of MMF and the torque from the slot model, with two segments in the open circuit fault condition

It can be seen in Figure 4 - 22, although the torque produced by summing the individual harmonic summation is lower than that of the full model, the shape is very similar. The large negative torque component is a direct result of a large four pole pair harmonic.

As it has been established from previous simulations, the fifth and fourth spatial harmonics are responsible for the negative torque for the motor under two lanes open circuit fault condition. Therefore, it is significant to suppress or even eliminate the impact of those harmonics.

Thus, a three-pole pairs winding rotor has been taken into consideration. With a particular winding configuration, it can eliminate the effect of particular harmonic, such as winding the rotor with a specific winding factor, or with a certain skew degree. In this project, both approaches will be applied to achieve the best possible performance.

4.5 A winding rotor design

4.5.1 The wound rotor topology for a 54 slots rotor

To further illustrate the reason that the wound rotor would not react to the fourth and fifth harmonic, the winding factor for the specific rotor design under different harmonic has been calculated and presented below.

The rotor has been designed as a six-pole, 54 slots, three-phase rotor, the winding configuration has been shown in Figure 4 - 23.
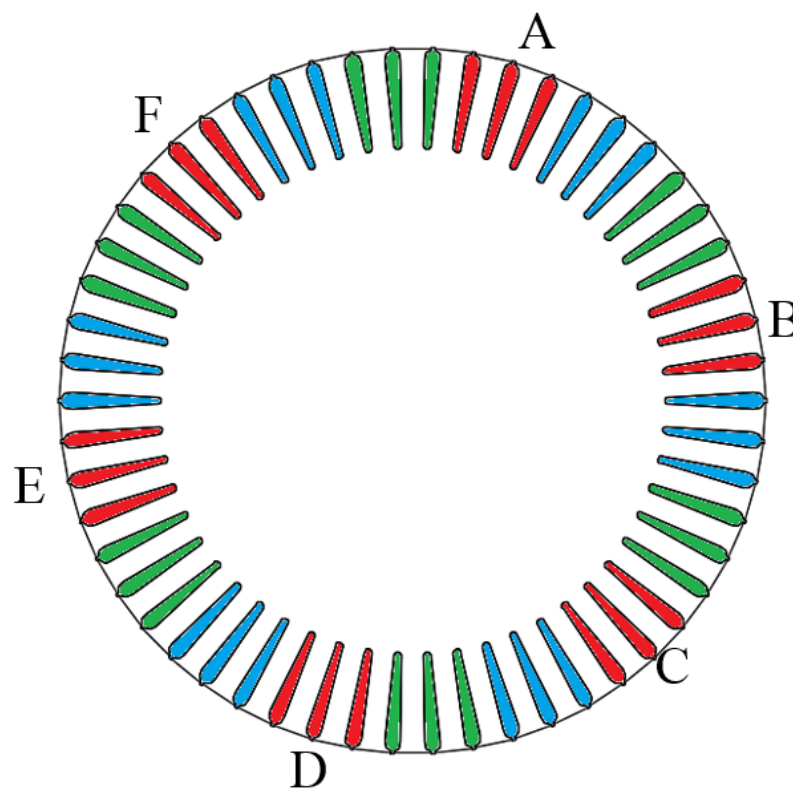
Figure 4 - 24: The winding configuration for 54 slots three-phase six-pole rotor

Table 9: The phase diagrams position for different harmonics

	A	B	C	D	E	F
Mechnical degree	0º	60º	120º	180º	240º	300º

1 pole pair	0º	-60º	120º	-180º	240º	-300º
2 pole pair	0º	-120º	240º	-360º	120º	240º
3 pole pair	0º	-180º	360º	-180º	360º	-180º
4 pole pair	0º	-240º	120º	-360º	240º	-120º
5 pole pair	0º	-300º	240º	-180º	120º	-60º

If consider the three red slots are one slot, the slot mechanical angle has been displayed in Table 9. The slot positions for different space harmonics are electrical angles. As described in Table 9, some of the phase diagrams of different spacial harmonics have been drawn to further illustrate the function of the proposed rotor.

For the fundamental space harmonic which is the third pole pair harmonics, the phase diagram is shown in Figure 4 - 24.

Figure 4 - 25: The phase diagram for fundamental harmonic

As the phase diagram shows all the slots are in the same direction, which indicates that the winding factor is one if, as mentioned before, the three slots are considered as one. Given there are three slots in this rotor, the winding factor will slightly lower than 1, due to the distribution factor. It should be noted that in Table 9, the positive and negative only represent direction, not the angle. As a result, -180º stands for 180º but in the opposite direction.

The phase diagram of the one pole-pair harmonic (first space harmonic) has been shown in Figure 4 - 25. As the amplitude of each slot is the same, the amplitudes of the A+D, E+B and C+F shall be the same, which means the sum up of those voltage phases should be zero. In this case, the first space harmonic should not have any impact on rotor performance.
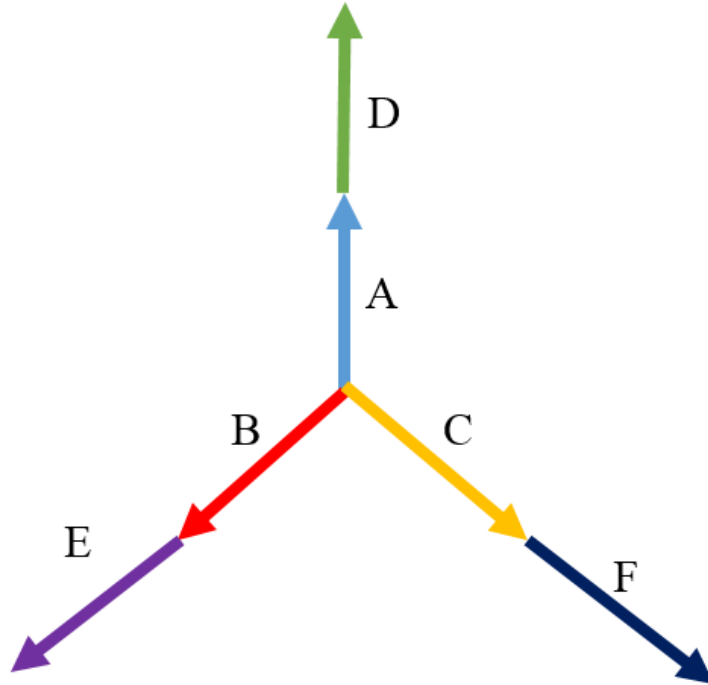
Figure 4 - 26: One pole pair harmonic voltage phase diagram

Similarly, the phase diagram of two-pole pair harmonic has been shown in Figure 4 - 26, as the A and D, C and F, B and E are cancelling each other the influence from the second space harmonic is zero.
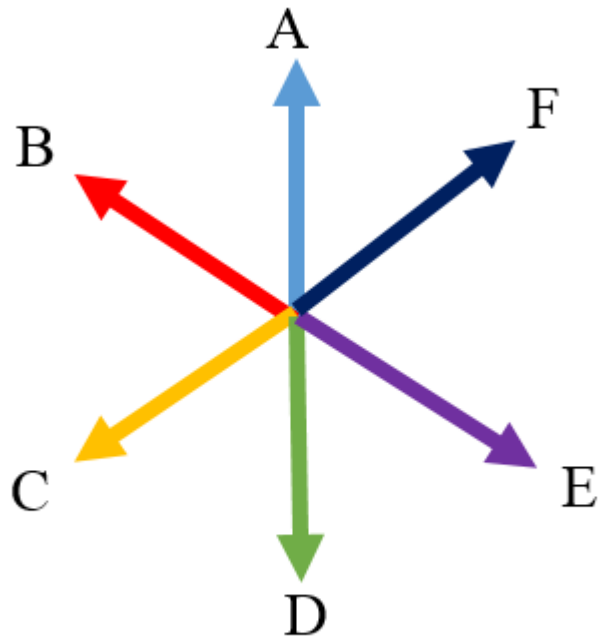
Figure 4 - 27: Two pole pair harmonic voltage phase diagram

The phase diagrams of four pole-pair and five pole-pair harmonics are shown in Figure 4 - 27 and Figure 4 - 28. Based on the same principle, the impact from fourth and fifth harmonics are proved to be zero.
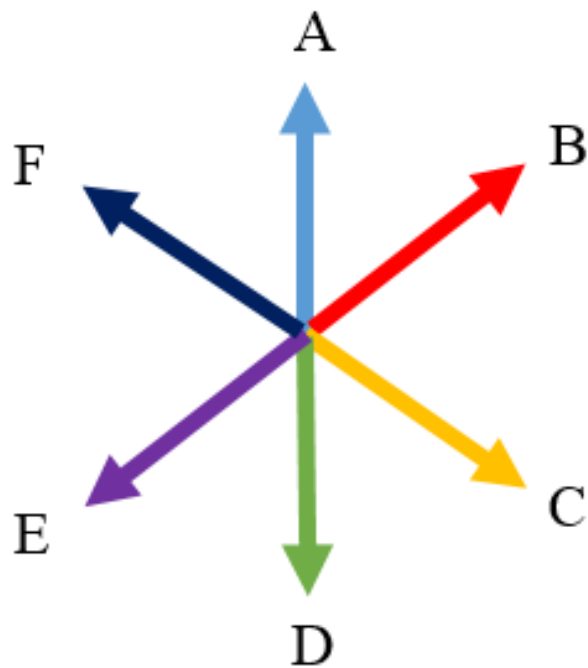
Figure 4 - 28: Four pole pair harmonic voltage phase diagram
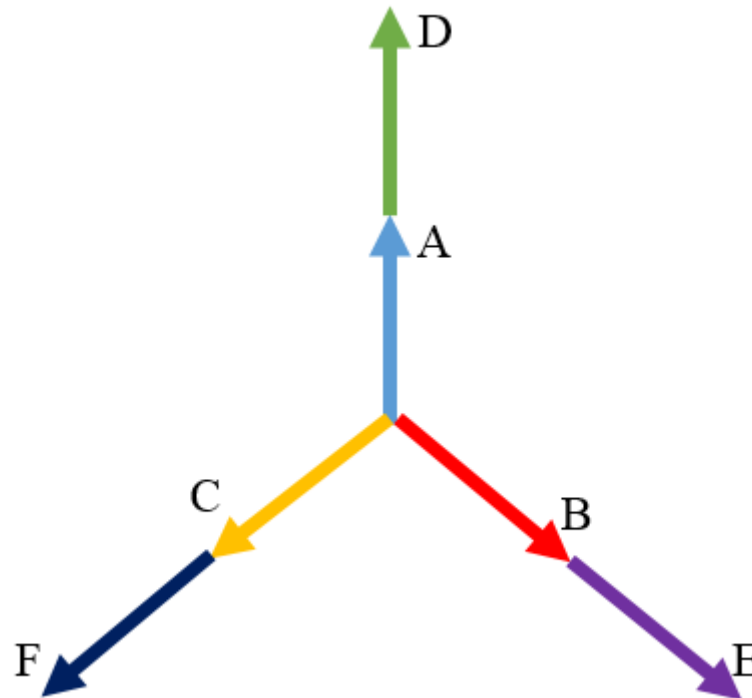
Figure 4 - 29: Five pole pair harmonic voltage diagram

As can be understood in the above phase diagrams, apart from the three-pole pair harmonic (the third spatial harmonic), the winding factors are all zero. In other words, the torque that is produced by harmonics other than the triple harmonic would be zero.

Based on this theory, the rotor winding is designed to be a six-pole three-phase rotor.

Regarding the slot number, the number can only be either 18 slots, which means one slot per phase per pole or 54 slots, which means three slots per phase per pole. The 36 slots have not been taken into consideration; according to [2], when the slot number of the rotor and stator are identical, there would be a high cogging torque produced which would highly reduce the performance of the motor.

As the 54 slots model is prone to be adjusted to different winding configurations such as a double-layer, even multi-three-phase connections, a 54 slots rotor model has been further studied for the initial design of the rotor.

4.5.2 The slot shape design

As it has been mentioned in 4.2.2, semi-closed slots have distinct advantages over other choices in small machines. For this design, the total rotor slot area has been made to be identical to that of the cage rotor which it replaces.
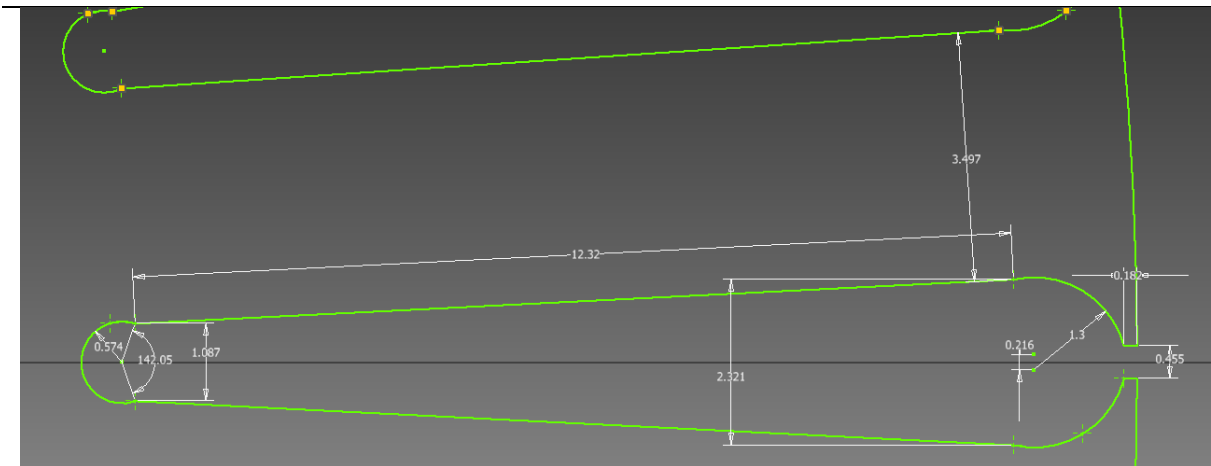
Figure 4 - 30: Rotor slot sketch (Unit: mm, degree)

The rotor slot shape is shown in Figure 4 - 29. This type of the slot shape is commonly used to produce medium starting torque induction machines. It helps to reduce the noise and torque pulsation at the expense of larger rotor leakage inductance.

4.6 Several winding configurations comparison

Although the basic winding configuration has been set, the author expends the scope to find if there is a way to furtherly optimise the rotor. Several winding configurations have been tested in simulation to find the best performance possible in both healthy and fault conditions.

4.6.1 Fully pitched single layer rotor

A three-phase single layer rotor winding connection is firstly shown in Figure 4 - 30.
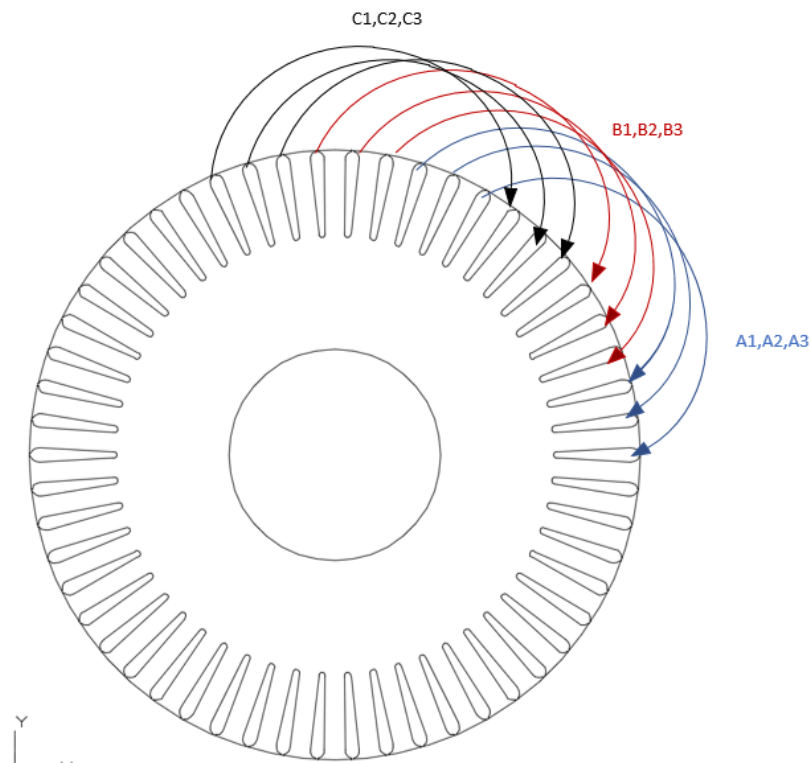
Figure 4 - 31: Rotor winding arrangement

Windings are connected in series and parallel connected with Phase B and Phase C. The simulation was conducted with three star-connected 50Hz voltage sources with rated voltage. The model is also being simulated with one segment open circuit and two segments open circuit. To be compatible with the conventional cage rotor, the stator has been kept the same, including the voltage source connection and the winding configuration. However, the simulation for the open circuit condition can only be done with a current source, since the rotating rotor entering and leaving the active part of the stator field could cause the voltage source to provide an unbalanced current, which changes the rotating fields into a one pole pair type. The discussion and analysis are all based on the ideal condition. In this project, all the simulations with an open circuit fault condition use the same current source as does the simplified current-controlled source.

For the fully pitched, three-pole pairs, three-phase single layer rotor, the result has been shown below.
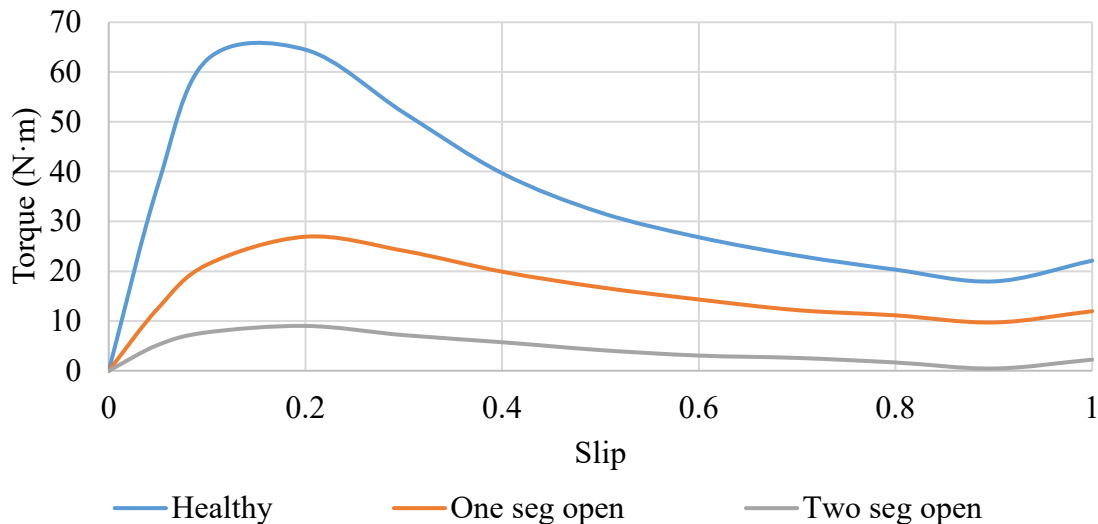
Figure 4 - 32: Torque comparison for the three-phase fully pitched single layer rotor under different conditions with 5.6 A current control 50 Hz

As can be seen in Figure 4 - 31, under the healthy condition, the proposed motor shows approximately the same maximum torque. Comparing to the conventional machine, the torque performance under one segment open circuit condition is more smooth and controlled, as seen in Figure 4 - 32. In the meantime, the torque in the lower speed range is smaller than the one with a cage rotor because removing the impact of the other harmonics, the positive torque they provide in the lower speed range is now missing.
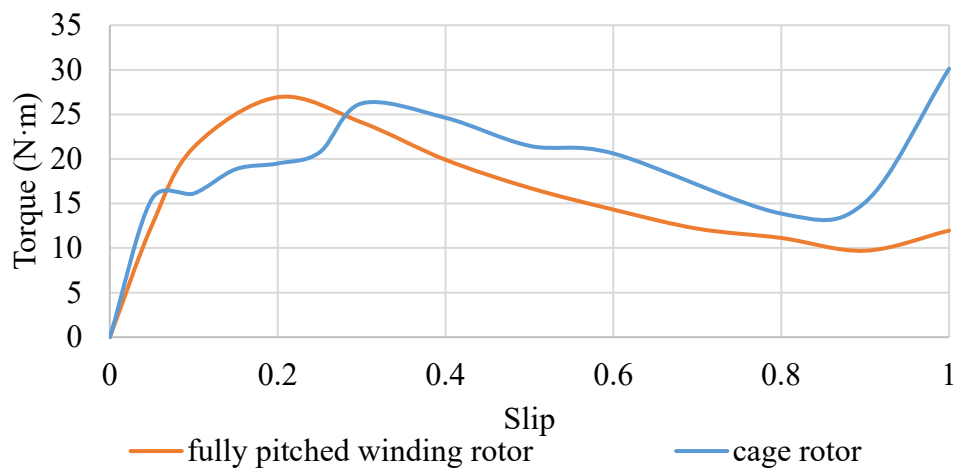
Figure 4 - 33: Triple three-phase induction machine under one segment open circuit with 5.6 A current control 50 Hz

Similarly, the performance of the two segments open circuit has been shown in Figure 4 - 33, the proposed rotor show smooth controlled torque slip curve compared to the cage rotor. The proposed rotor also eliminates the negative torque during the slip range between 0.1 to 0.3.
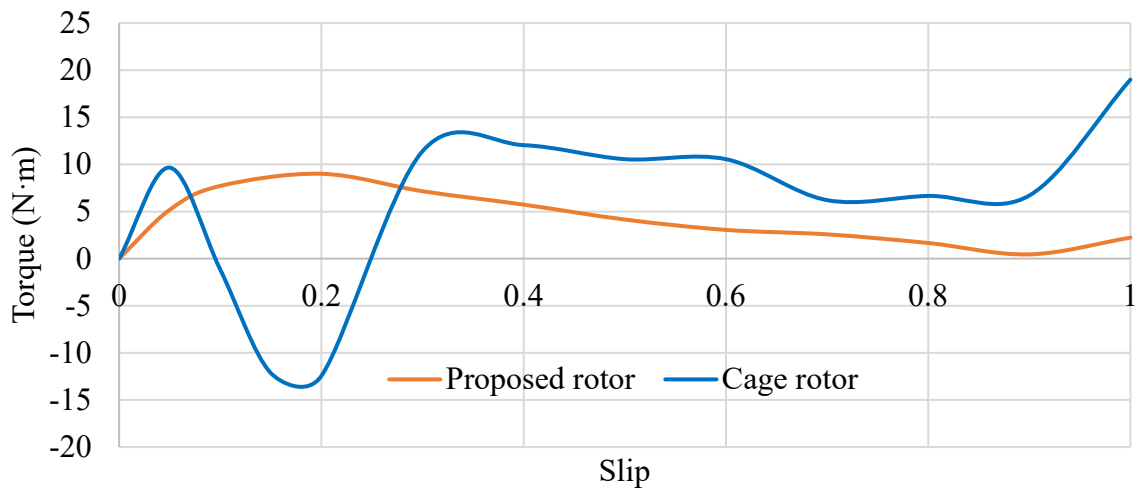
Figure 4 - 34: The triple three-phase induction machine under two segments open circuit with 5.6 A current control 50 Hz

From Figure 4 - 31, for two iconic speeds, the ratio for the torque reduction has been gathered in Table 10. The percentage in parentheses is the percentage of the torque of the motor when operating under error conditions to the torque during healthy operation.

Table 10: Quantity comparison at the maximum torque speed and rated speed

	Healthy	One-seg open	Two-seg open
0.05 (rated)	37.2	12.5 (33.6%)	5.1 (13.7%)
0.2 (maximum)	64.5	26.9 (41.7%)	9.0 (7.6%)

For the nature of the project, the one segment open circuit condition means that one-third of the stator is entirely off-line, which means the fundamental H field should be two-third of the original one.

Moreover, according to the simplified single-phase equivalent circuit,
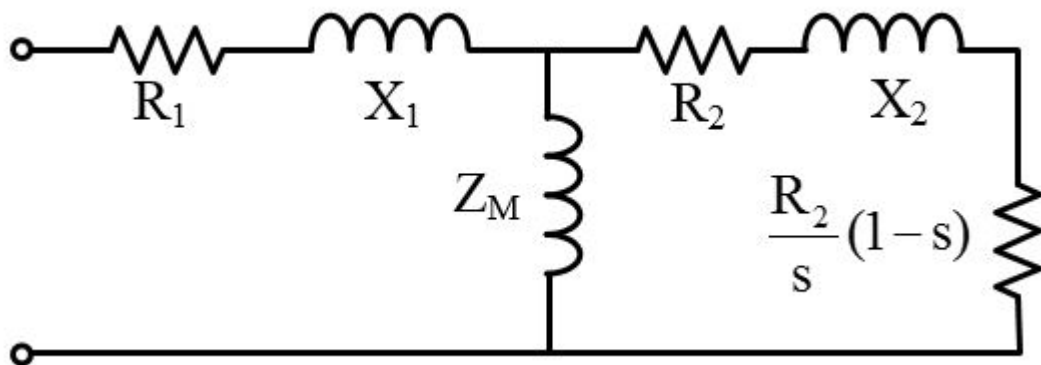
Figure 4 - 35: Standard single-phase equivalent circuit for an induction machine
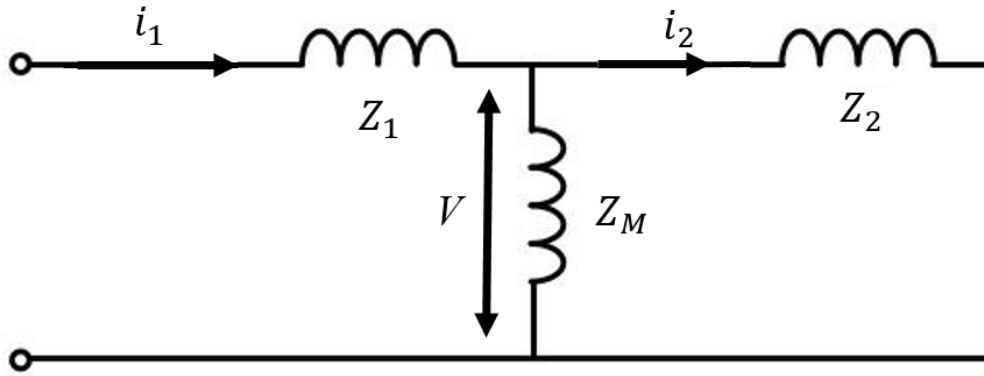
Figure 4 - 36: The simplified single-phase equivalent circuit for an induction machine

For a specific speed, the parameters in the standard equivalent circuit are the same. As a result, the resistance and inductance can be seen as impedance for calculation simplify purpose, which gives Figure 4 - 35.

According to Figure 4 - 34, the electrical power is

$$P = i_2^2 \left(\frac{R_2}{s} (1 - s) \right) \tag{4 - 22}$$

$$T = \frac{P}{\omega} = \frac{P}{2\pi \times 50(1 - s)} \tag{4 - 23}$$

, where ω is the synchronous speed, R_2 is the rotor resistance, s is the slip, i_2 is the rotor side current after converting, T is the electromagnetic torque, P is the active power.

Sub (4 - 9) into (4 - 10),

$$T = \frac{i_2^2 \left(\frac{R_2}{s} (1 - s) \right)}{2\pi \times 50(1 - s)} \tag{4 - 24}$$

According to Figure 4 - 35, there are

$$V = i_1 \frac{Z_m Z_2}{Z_m + Z_2} \tag{4 - 25}$$

$$i_2 = \frac{V}{Z_2} \tag{4 - 26}$$

Sub (4 - 12) into (4 - 13),

$$i_2 = \frac{i_1 \frac{Z_m Z_2}{Z_m + Z_2}}{Z_2} = i_1 \frac{Z_m Z_2}{(Z_m + Z_2)Z_2} \tag{4 - 27}$$

Because the relationship between i_1 and T is one that would help to understand the performance of the proposed motor, (4 - 14) has been used to replace the i_2 in (4 - 11).

$$T = \frac{\left(i_1 \frac{Z_m Z_2}{(Z_m + Z_2)Z_2}\right)^2 \left(\frac{R_2}{s}(1-s)\right)}{2\pi \times 50(1-s)} = i_1^2 \frac{\left(\frac{Z_m Z_2}{(Z_m + Z_2)Z_2}\right)^2 \left(\frac{R_2}{s}(1-s)\right)}{2\pi \times 50(1-s)} \qquad (4\text{ - }28)$$

As can be seen in (4 - 15), for a specific speed the latter part of the equation is a constant value. The torque is positive in proportion to the i_1^2 which is the stator current. Assuming current control from an inverter then, when two-thirds of the machine is operating, the current in total should be two-third of its healthy value. In that case, the torque is expected to be $\left(\frac{2}{3}\right)^2$, which is $\frac{4}{9}$ of the original healthy torque.

As a result, in this case, the expected values and the values produced by simulation have been gathered in Table 11

Table 11: Comparison between the expected value (in bracket) and simulation value

	Healthy	**One-seg open**	**Two-seg open**
0.05 (rated)	37.2	12.5 (16.5)	5.1 (4.2)
0.2 (maximum)	64.5	26.9 (28.7)	9.0 (7.2)

It can be seen that the error is no more than 20% in both two cases, which suggests that the predictions are generally correct, though with a large margin of error.

4.6.2 Double-layer nine-phase short-pitched by two slots rotor

As mentioned before, the rotor is a three-phase 6 pole one, it only reacts to the triple harmonics. It has been found that the 15th and 21st harmonics are the most significant harmonics. As the fully pitched 54 slots rotor is not able to eliminate the 15th and 21st harmonics, a double-layer three-phase rotor short-pitched for two slots have been considered.

The short pitch angle is decided by the pitch factor.

$$k_p = \cos\frac{r\alpha}{2} \qquad (4\text{ - }29)$$

, where k_p is the pitch factor, r is the harmonic order, α is the short pitch angle. Base on that, the rotor short pitch angle has been calculated as

$$\cos\frac{r\alpha}{2} = \cos\frac{15\alpha}{2} = 0, \alpha = 12^{\circ} \qquad (4\text{ - }30)$$

$$\cos\frac{r\alpha}{2} = \cos\frac{21\alpha}{2} = 0, \alpha = 8.3^{\circ} \tag{4 - 31}$$

The rotor is a 54 slots rotor, each slot compromises 6.66°. For two slots short-pitched rotor, it will help to eliminate the 15th and 21st harmonics.

The winding configuration for Phase A has been sketched and shown in Figure 4 - 36.
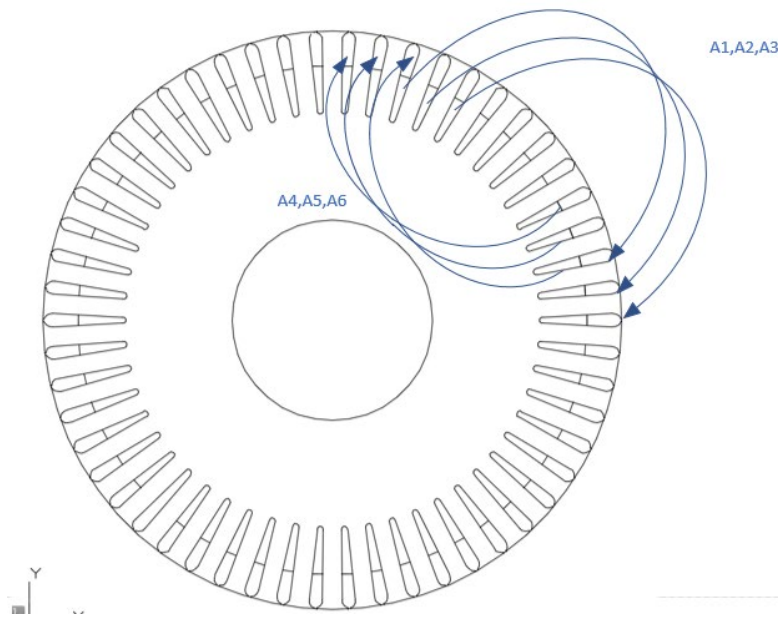
Figure 4 - 37: The winding configuration for the nine-phase double-layer short-pitched for two slots rotor

The simulation results have been shown in Figure 4 - 37.
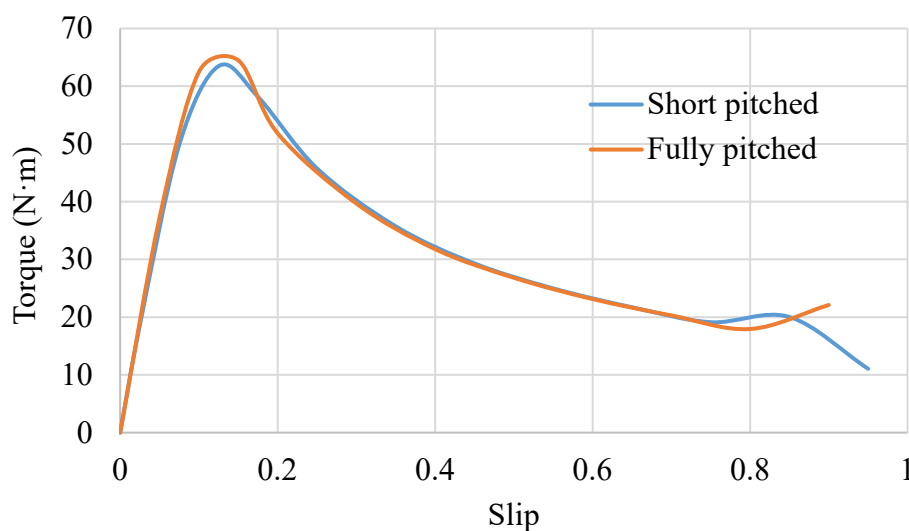
Figure 4 - 38: The Double-layer rotor with two slots short-pitched under the healthy condition with 5.6 A current control 50 Hz

As can be seen that the three-phase short-pitched model performs slightly lower than the fully pitched one in torque, which is caused by the pitch factor.
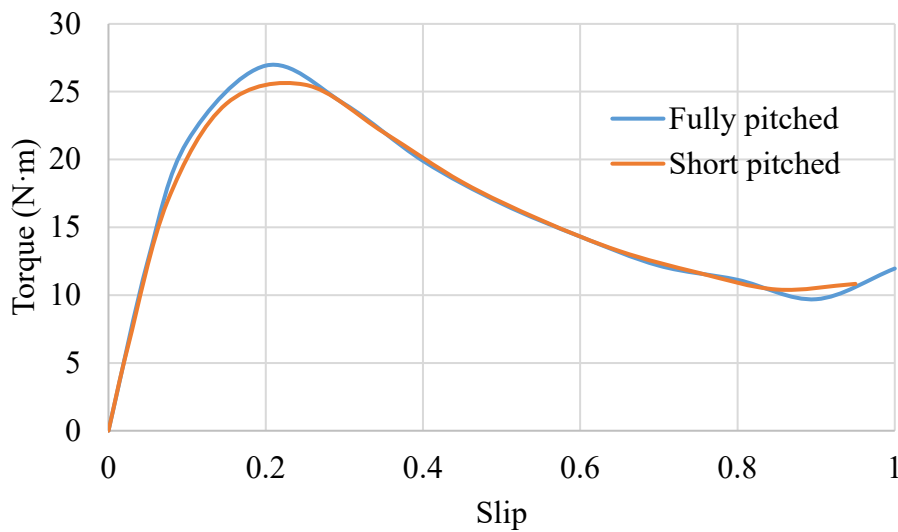
Figure 4 - 39: The Double-layer rotor with two slots short-pitched under one segment open circuit condition with 5.6 A current control 50 Hz

For all the discussion above, it has been concluded that for the triple three-phase fault-tolerant induction machine, the three-phase fully pitched rotor is a better choice compare to other winding configurations.

4.7 18 slots Rotor

As it has been established that the three-phase three-pole pair fully pitched rotor is the scenario which needs to be adopted, ways of manufacturing the rotor have been considered.

The rotor must be wound with bars; solid copper was chosen to provide the lowest resistance. A balanced three-phase, six-pole windings with an integer number of slots per pole per phase needs a multiple of 18 slots. 36 or 54 slots proved to be difficult to construct due to the limitation of the fixed rotor size, so an 18 slot rotor design was selected in this project.

A semi-closed slot was adopted with a slot opening of 0.5 mm.

For the convenience of manufacturing, a semi-open slot has been chosen this time. The slot and teeth dimensions are shown in Figure 4 - 39. This shape of the rotor slot is frequently used in high starting torque, high rated slip induction machines.
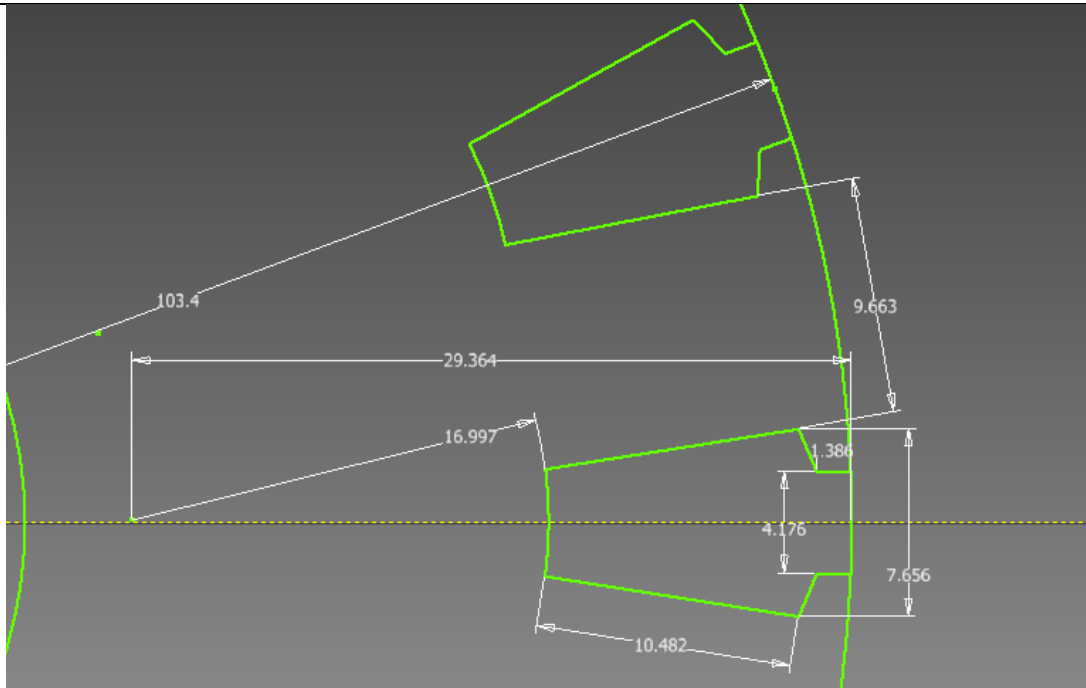
Figure 4 - 40: Rectangular deep bar rotor slot sketch (unit: mm, deg)
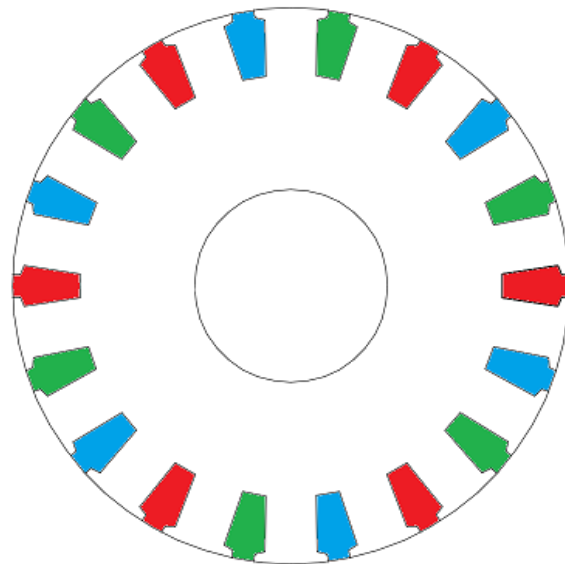
Figure 4 - 41: Slots rotor winding configuration (Red: Phase A, Blue: Phase B, Green: Phase C)

Compared to the 54 slots rotor and 18 slots rotor, it can be easily understood from Figure 4 - 41 that the 18 slot rotor reaches the maximum torque at 0.05 slip instead of 0.2 slip. This is because the cross sectional area for the slot is larger, which correspondingly reduces the resistance in the rotor. During the process of designing the rotor slot, the sum-up of all the slots' cross-section area has been kept the same. The rotor resistance and the torque relationship has been demonstrated in Figure 4 - 42.
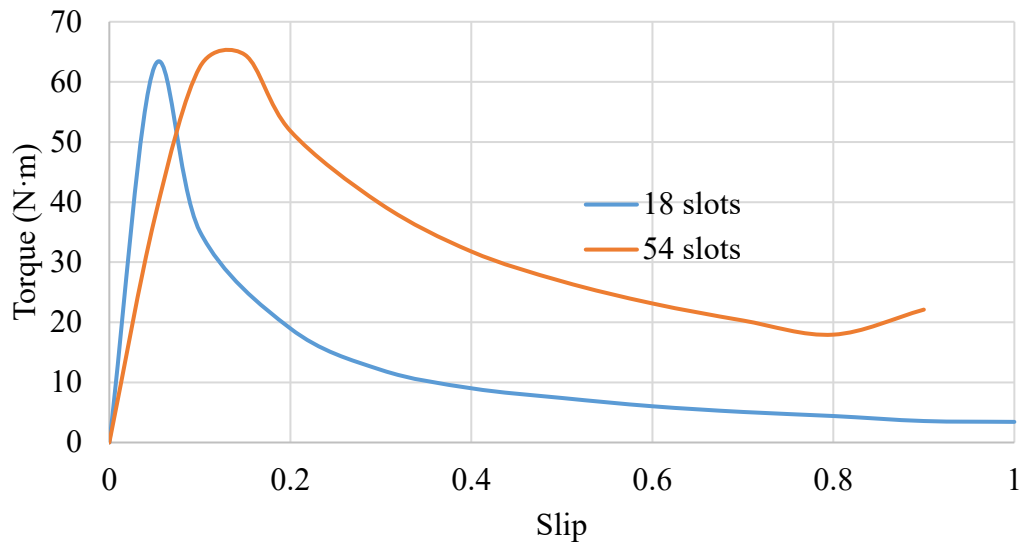
Figure 4 - 42: Torque comparison between the 54 slots rotor and 18slots rotor in the healthy condition
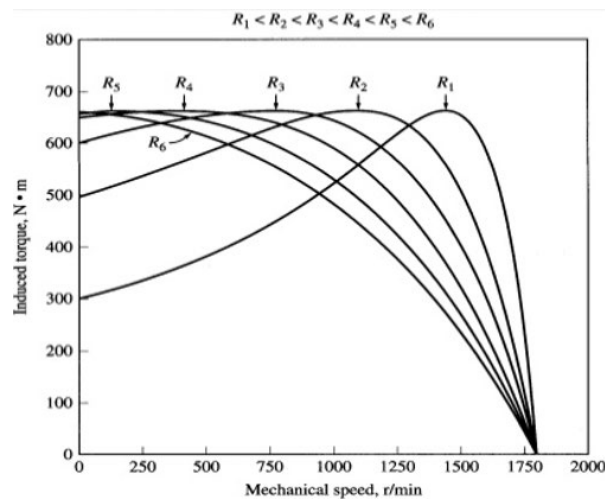
Figure 4 - 43: The relationship between the rotor resistance and maximum torque speed[2]

As can be seen in Figure 4 - 42, the smaller the rotor resistance is, the quicker the torque reaches the maximum.

Regarding fault-tolerant ability, the 18 slots fully pitched rotor shows expected results.
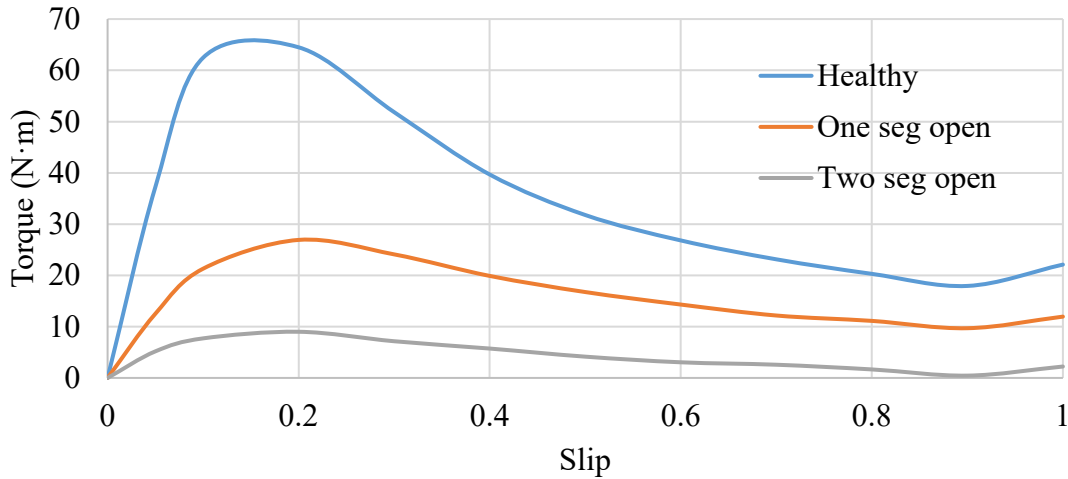
Figure 4 - 44: The 18 slots rotor model under different operating conditions

Table 12: The expected results and simulated result comparison

	Healthy	**One-seg open**	**Two-seg open**
0.05 (rated)	48.2	21.3 (21.4)	5.4 (5.4)

However, the simulated results in Figure 4 - 43 is the model without end winding resistance. For this particular case, the end winding resistance can be calculated as the following procedure.

Take the electrical resistivity for the material at the room temperature 20℃, in this case, is 1.87×10^{-8} $ohms/m$.

For the rotor, in this case, there are 63 turns in the rotor, according to the formula

$$R = \rho \frac{l}{S}$$ (4 - 32)

The resistance is calculated as

$$R = 1.87 \times 10^{-8} \times \frac{161 \times 10^{-3} \times 63}{\frac{66.26}{63} \times 10^{-6}} = 0.89 \ Ohms$$ (4 - 33)

As have been discussed that the end winding should be half of the resistance in one slot and for one phase it has two sides and three sets of coils; as a result, the end winding should be

$$R_{phase} = 0.89 \div 2 \times 2 \times 3 = 2.7 \ Ohms$$ (4 - 34)

As a result, the phase end winding resistance is set to 2.7 Ohms. With the end winding resistance, the torque slip curve has been shown in Figure 4 - 44.
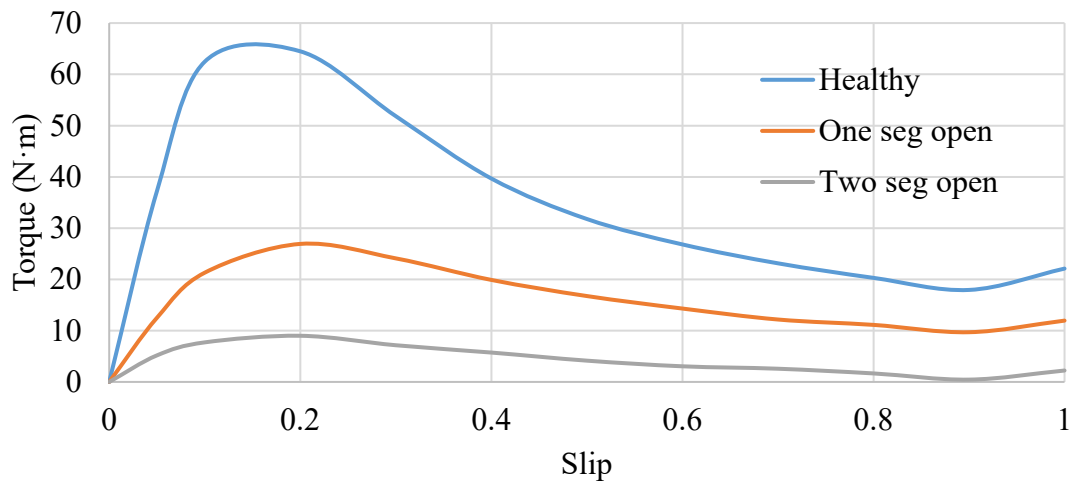
Figure 4 - 45: 18 slots Rotor under different conditions with end winding resistance

4.8 The 18 slot rotor model performance under one segment short circuit condition

Based on the same principle, this project also investigates the performance of the proposed motor under one segment short circuit. The conventional motor and proposed rotor under short circuit condition will be compared and discussed.

The simulation for the cage rotor with one segment shorted is operated with three star-connected voltage sources. The RMS phase voltage is 230 V, which is 400 V for a line to line voltage. Instead of using the conventional model, this simulation used the proposed model by adjusting the rotor into a cage rotor. In this case, the simulation results can be compared, due to the unchanged stator. The torque slip curve has been shown in Figure 4 - 45
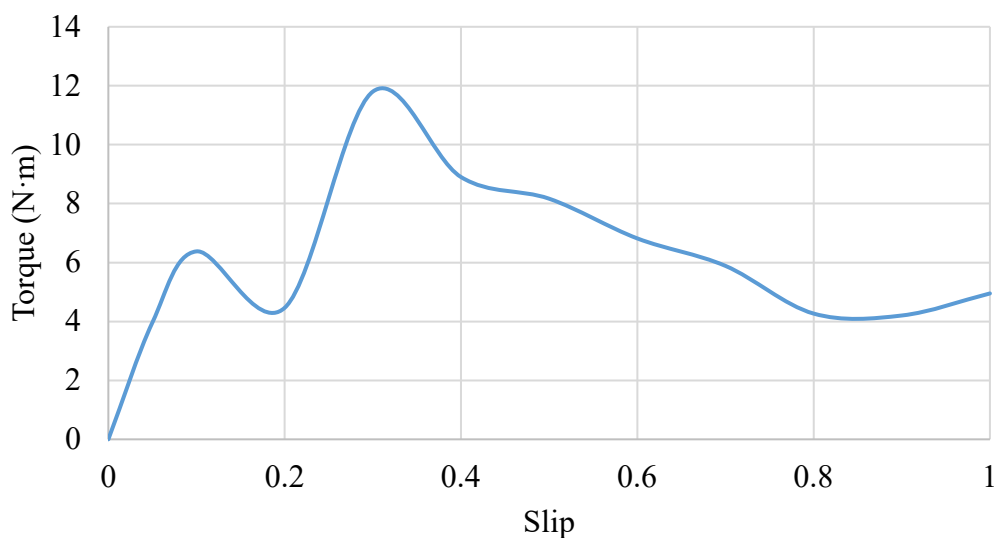
Figure 4 - 46: The cage rotor under short circuit condition

As can be seen in Figure 4 - 45 and Figure 4 - 46, there is a minimal tip at the slip of 0.2, which is similar to the performance found in one segment open circuit operation. To further study this performance and following the same principle of research to this project, the harmonic spectrum of the motor operating with a cage rotor has been studied, the results have been shown in Figure 4 - 46
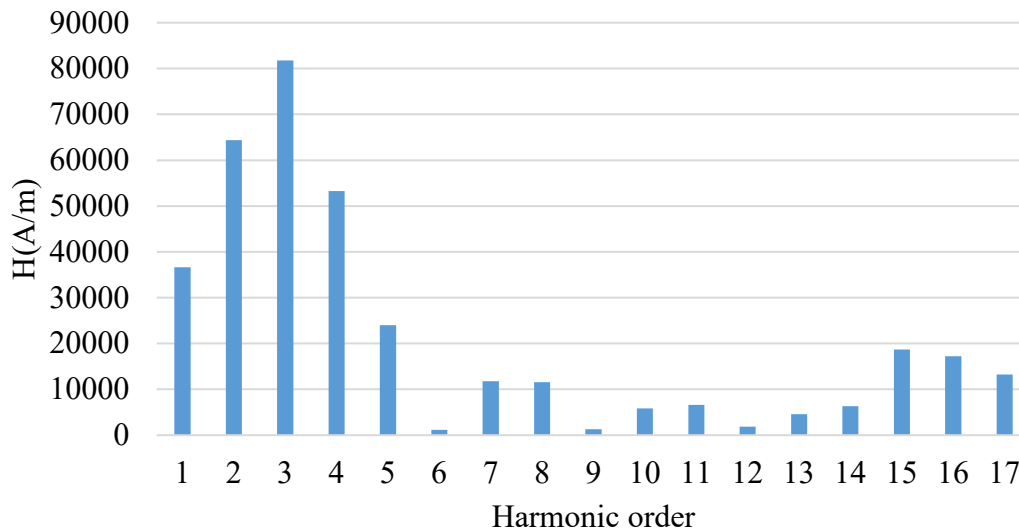
Figure 4 - 47: Harmonics spectrum for cage rotor with one segment shorted

As seen in Figure 4 - 46, the first, second, fourth and fifth harmonics are rich in the spectrum, which is the reason that causing the problems that in the torque slip curve. As it has been established by the current sheet model the fifth and fourth harmonics are providing negative torque during the 750 rpm to 1000 rpm, eliminating the fourth and fifth harmonics will help to improve the performance of the proposed motor under one segment short circuit.

As a result, the simulation of the wound rotor with one segment shorted has been presented as seen in Figure 4 - 47. It can be understood that the proposed rotor helps to eliminate the effect of other harmonics and improve the performance into a controlled induction motor torque slip curve. It also can be seen that the peak torque of the proposed motor is smaller than the one with a cage rotor. The reason for that phenomenon is the first and second harmonics provides positive torque, in the meantime, the fourth and fifth harmonic provides positive torque during the speed from 750 rpm to zero rpm. By eliminating the impact of other harmonics, the positive effect of those harmonics is being eliminated as well.
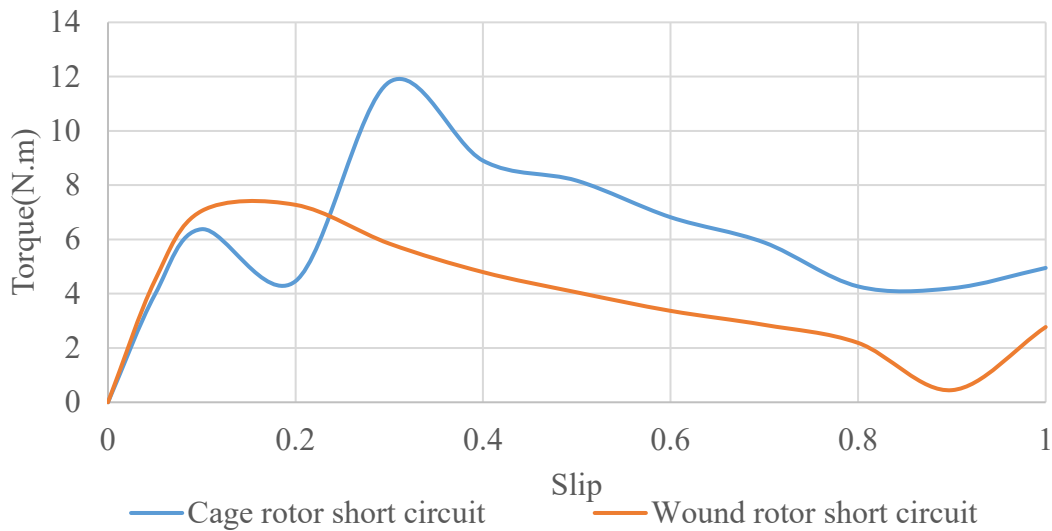
Figure 4 - 48: Torque slip curves for wound rotor and cage rotor with one segment shorted

As a result, the simulation proves that the proposed rotor has the effect of retaining a certain part of the function and maintain a controlled torque slip curve, which is believed to be the first time in the field of induction machine design.

4.9 The saturation check for the final design

Figure 4 - 48, shows the flux distribution under healthy conditions for the 18 slots rotor model. During the rotor design, the tooth width has been chosen to be twice that of the tooth width in the stator. Because there is only half the number of slots, this should give similar rotor and stator saturation conditions. The saturation check is at the rated torque slip condition, which is 0.05 in this case.
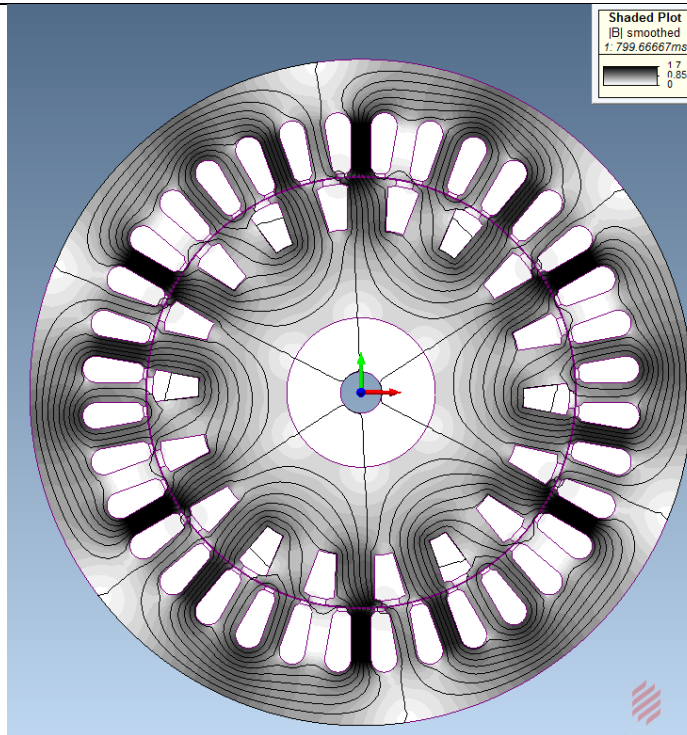
Figure 4 - 49: Healthy condition for the 18 slots rotor model

The flux density in the core back is 1.65T, the flux density in the teeth is 1.88T, and the flux density in the rotor teeth is 1.55T.

The saturation check for the 18 slots rotor model under one segment open-circuit condition.
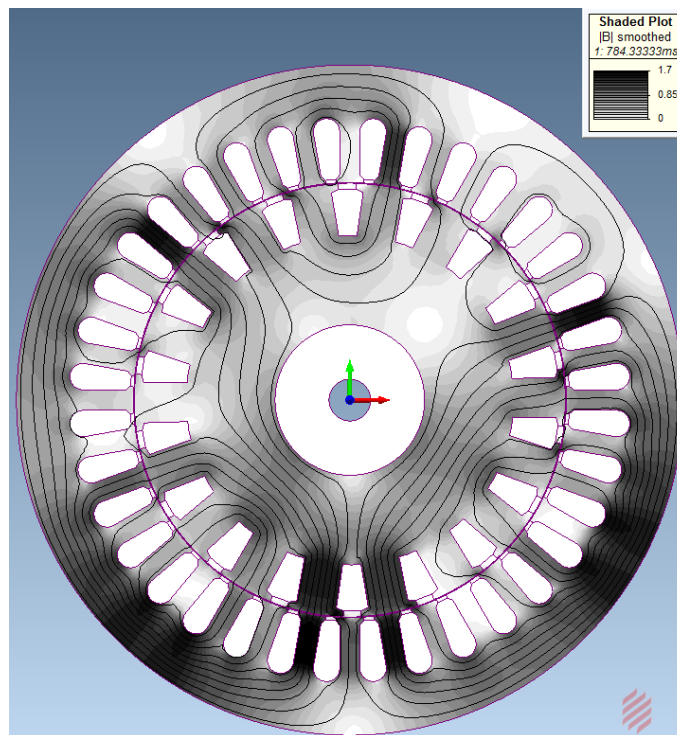
Figure 4 - 50: 18 slots rotor model under one segment open circuit condition

The flux density in the core back is 1.86T, the flux density in the teeth is 1.87T, and the flux density in the rotor teeth is 1.73T

The saturation check for the 18 slots rotor model under two segments open-circuit condition.
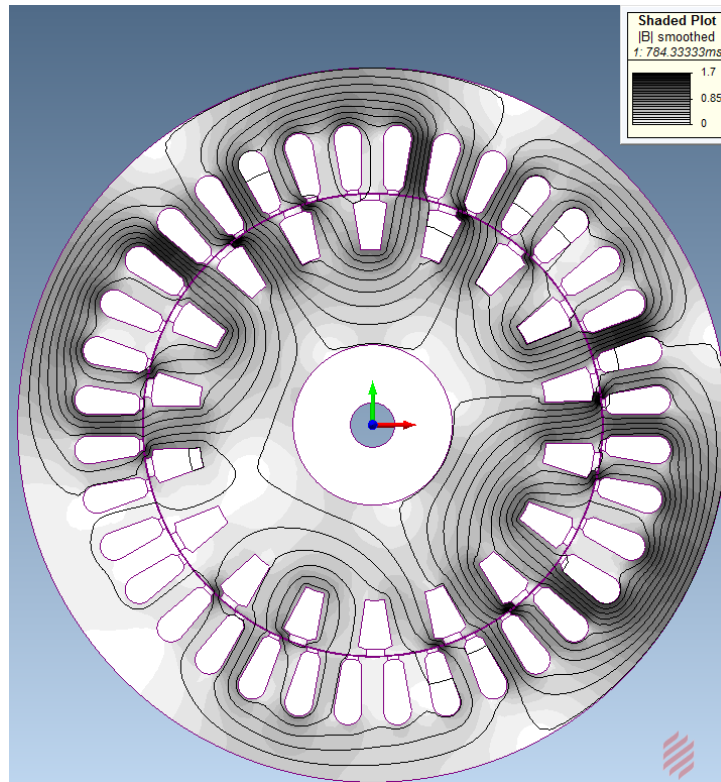
Figure 4 - 51: 18 slots rotor model under one segment short circuit condition

The flux density in the core back is 1.86T, and the flux density in the teeth is 1.83T.

The above results indicate that saturation conditions are acceptable in the 18 slot rotor design. There is no saturation in the rotor and saturation is not excessive in the stator.

4.10 Rotor Loss

The rotor of the proposed rotor is a fully pitched three-phase connection with all terminals star connected. Rotor loss takes a large part of the total loss of the machine. The table below gives finite element based predictions of rotor loss in the proposed machine and the conventional machine with a cage rotor, operating under different conditions.

Table 13: The 18 slots rotor loss under different conditions (high speed only)

	Healthy	**One-seg open**	**Two-seg open**
0.01	19.70W	6.72W	1.90W
0.02	78.39W	23.87W	7.59W
0.03	154.16W	43.44W	15.18W

0.04	224.26W	70.39W	23.35W
0.05	299.01W	93.85W	31.13W

Table 14: Rotor loss comparison between the 18 slots rotor and cage rotor under the two segments open circuit condition

	18 slots rotor(Cu)	Cage rotor(Al)
0.01	1.90W	103.96W
0.02	7.59W	108.15W
0.03	15.18W	116.48W
0.04	23.35W	126.28W
0.05	31.13W	132.39W

Table 15: Rotor loss comparison between the 18 slots rotor and cage rotor under the healthy condition

	18 slots rotor(Cu)	Cage rotor(Al)
0.01	19.70W	178.56W
0.02	78.39W	214.03W
0.03	154.16W	263.70W
0.04	224.26W	317.22W
0.05	299.01W	380.67W

From Table 13, Table 14 and Table 15, it can be understood that compared to the cage rotor the rotor loss is significantly reduced, especially in the fault condition. The reason is not only larger cross-area for the slot and low electrical resistivity for the coil material (from aluminium to copper) result in the lower resistance in the rotor, which reduces the rotor loss, but the 18 slots three pole-pair rotor do not react to the fourth and fifth harmonics, which result in a decrease in the rotor current, therefore, the rotor loss is significantly reduced. It should be noted that the loss is calculated based on the simulation only.

4.11 Torque ripple study

To study the best possible skew angle for the 18 slots rotor model, several skew angles have been taken into consideration. The rotor slot angle is 20 degrees, and the stator slot angle is 10 degrees. Cogging torque with skews of 5 degrees, 10 degrees and 20 degrees has been simulated using finite elements, as shown in Table 16. All the results are obtained from a healthy operating model at rated slip which is 0.05. The method of simulating the skew effect is the same method mentioned in Chapter 3 for the skew effect simulation of a conventional induction machine.

Table 16: Torque ripple compare

	Without Skew	**10-degree skew**	**20-degree skew**
Average torque	27.57 N·m	27.14 N·m	27.63 N·m
MAX torque	32.64 N·m	30.46 N·m	30.32 N·m
MIN torque	22.79 N·m	24.37 N·m	24.31 N·m
Torque ripple	35.75%	22.44%	21.7%

In Figure 4 - 51, the current in the rotor has been compared to show the skew effect, although the amplitude is smaller than the one without skew, the harmonics have been decreased.
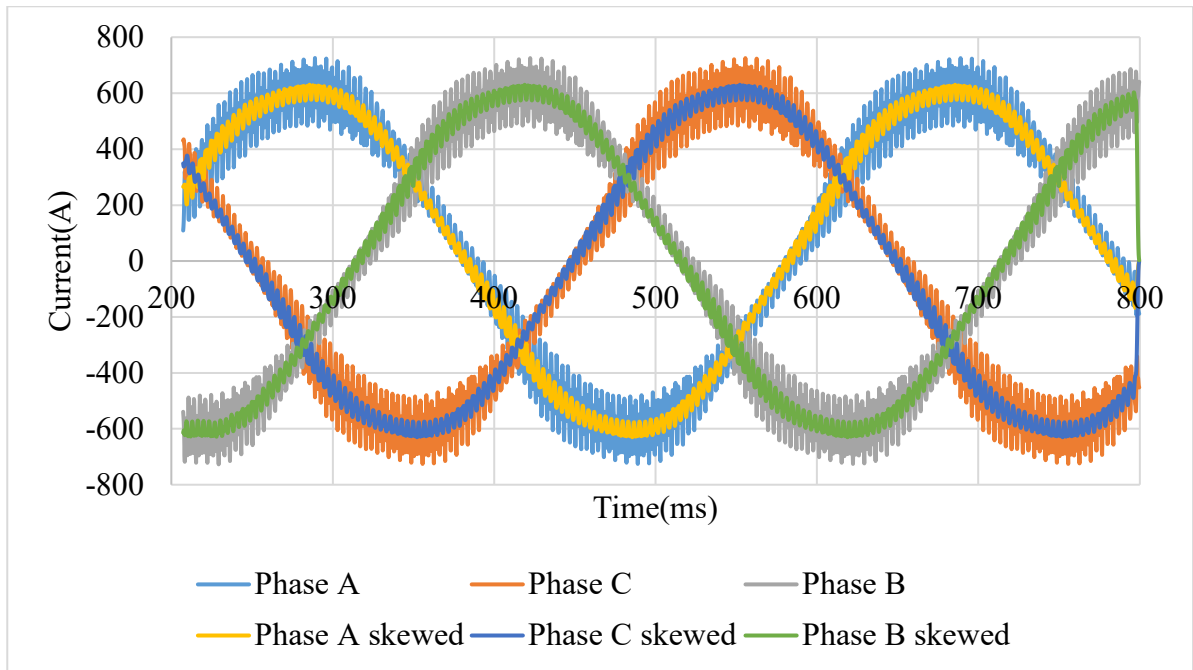
Figure 4 - 52: Rotor current with and without skew effect

4.12 Efficiency

According to the "Standard IEC 60034-30-1" valid since March 2014, there are four levels for induction machine to perform with 3000 W power (the proposed is 3040 W, it is believed to be around the same standard) efficiency, which are

- IE1 Standard efficiency $79.1\% \leq \eta \leq 83.5\%$
- IE2 High efficiency $83.5\% \leq \eta \leq 86.2\%$
- IE3 Premium efficiency $86.2\% \leq \eta \leq 89.7\%$
- IE4 Super-premium efficiency $89.7\% \leq \eta \leq 100\%$

The efficiency is a significant criterion to evaluate an induction machine. Simulations were performed to determine the efficiency at the rated speed, in this case, is 0.05 slip.
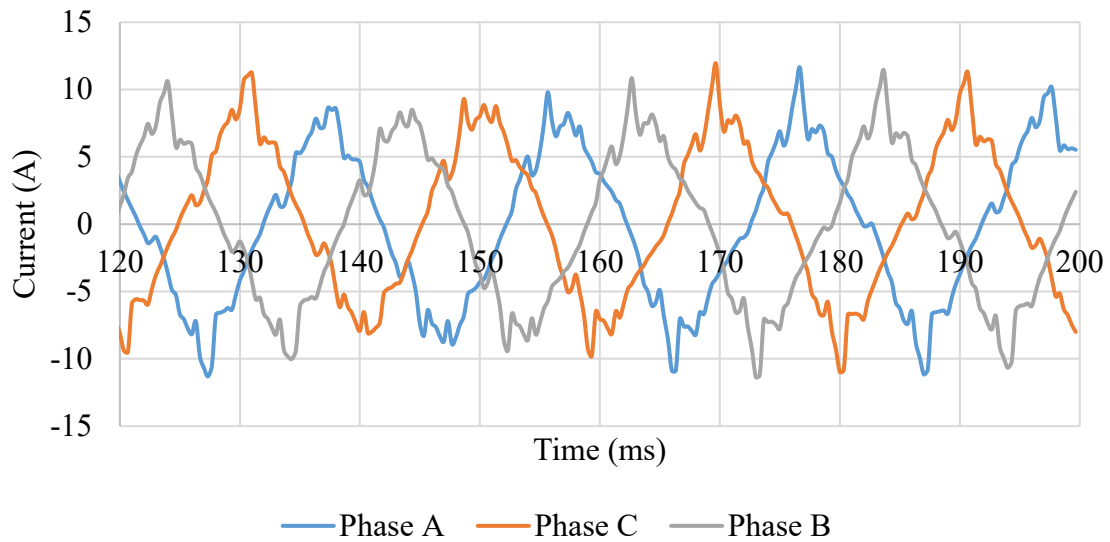
Figure 4 - 53: The voltage source current in the steady state. Rated voltage of 50 Hz applied at all points.
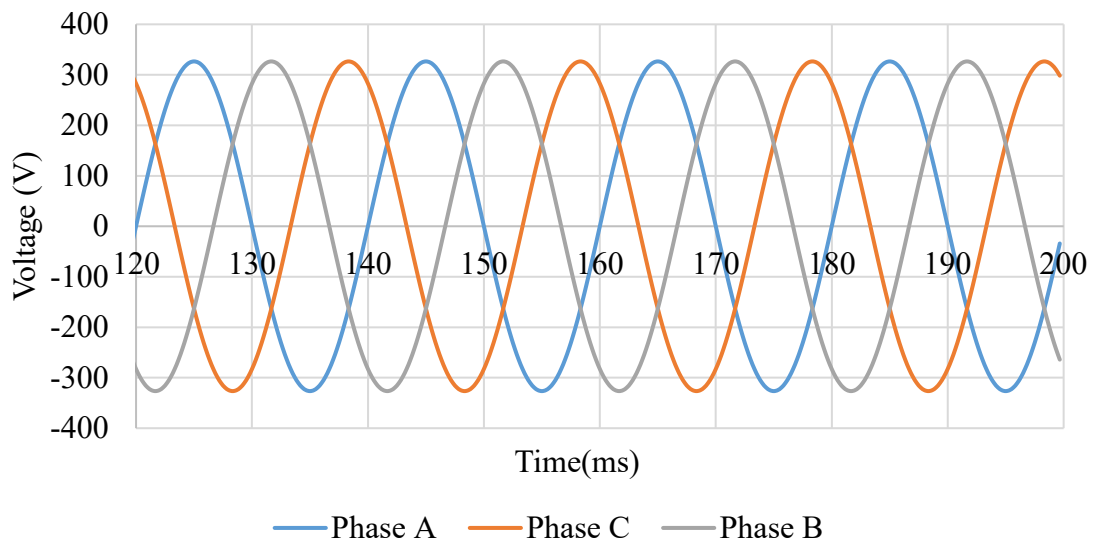
Figure 4 - 54: The voltage source voltage in the steady state. Rated voltage of 50 Hz applied at all points.

As seen in Figure 4 - 52 and Figure 4 - 53, the voltage and the current of the power source has been shown. By multiplying the instantaneous voltage and current, the instantaneous power input of the proposed motor has been shown in Figure 4 - 54.
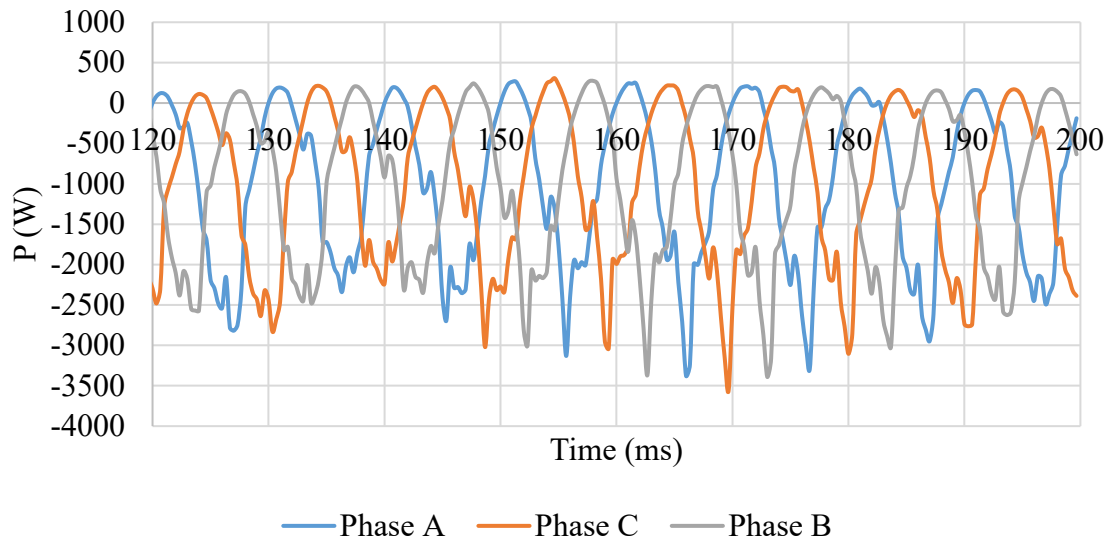
Figure 4 - 55: The power output from the power source. Rated voltage of 50 Hz applied at all points.

The average input powers for each phase are -1044 W -989 W and -1007 W for Phase A, C and B respectively. As a result, the input power should be

$$P_{in} = 1044\ W + 989\ W + 1007\ W = 3040\ W$$

The output power can be calculated as

$$P = T\omega$$

The simulation is done by the voltage-controlled 50 Hz 400 V RMS value line to line voltage. The average torque for the 0.05 slip is 27.82 N·m. As a result,

$$P_{out} = T\omega = 27.82 \times 950 \div 9.88 = 2675.2\ W$$

As a result, efficiency is

$$\eta = \frac{P_{out}}{P_{in}} = \frac{2675.2}{3040} = 88\%$$

, which is premium efficiency.

4.13 Summary

This chapter focused on the problems found in the triple three-phase induction machine. It starts with the principle of the fault-tolerant induction machine, which is utilising the redundancy of the windings and inverters to create an induction machine with several segments which are electrically, thermally, and physically isolated to one and another. Then, this chapter focused on the winding configurations to achieve that principle and slot geometry for better machine

performance. In this section, the advantages and disadvantages have been discussed for several choices of the slot shape. The detailed parameters of the slots shape have been demonstrated as well. The stator winding connection for the conventional induction machine and the triple three-phase induction machine has been drawn in two figures to show that the latter one has distinct advantages over the former one as well as to visually confirm that the triple three-phase induction machine has no overlap between any two segments.

The second part of this chapter focused on the healthy performance of the triple three-phase induction machine. It first showed the results of the model with voltage control under healthy conditions, which means the motor is simulated with no fault condition. The results show that the torque ripple is relatively larger than expected, which leads to the study of the torque ripple. There are many reasons that the simulation torque ripple is higher than expected. In this chapter, only three of them have been introduced and studied to find the most relevant cause of this phenomenon. By controlling the simulation with only one of the possible causes changed and then comparing the impact of this cause to others, the cause that affects the results most is the most relevant cause, which is the skew effect in this case. In this part of the chapter, two methods to simulate the skew effect on the rotor side were demonstrated. Due to the time limitation, the 3D simulation has not been considered, which leaves the option to construct an n-slice model. The N-slice model is a method that, by dividing the machine in Z direction into n slice of machines and connecting each part as a complete machine, the constructed model will show the skew effect with reduced performance compared to the 3D simulation. By increasing the number of slices the result will be infinitely close to the effect in practice.

In the third part, most efforts had been put into the performance of the triple three-phase induction motor in fault conditions. The performance under the fault condition is much better than the one in a conventional induction machine. However, it also has been found that the torque-slip curve has a tip during the speed range of 700rpm to 800rpm in both one and two segments open circuit condition. In this case, the harmonic component and their contribution to the torque has been studied. In this part of the chapter, the 4th and 5th harmonics are found to provide significantly high negative torque to the torque slip curve in total. To study the effect of each harmonic, a method called 'current sheet model' has been introduced. This method is shown by creating a sheet of current around the rotor so it can react to different harmonics independently, which will help to understand the performance of the motor.

The fourth part focused on proposing a new rotor to avoid the tip in the torque-slip curve. Many ideas have been considered, but in this project, the winding rotor has been chosen to optimise

performance. The winding configuration has been demonstrated to show that this particular winding would help to eliminate the effect of the harmonic other than the triple space harmonics. In this part, the phase diagram of different harmonics has been constructed and found that, except the triple harmonics, other harmonics are adding up to zero, which shows those harmonics will not impact the performance of the motor. Furthermore, the simulation of a three-phase 54 slots fully pitched rotor results has been compared to the performance of the triple three-phase induction machine with a standard cage rotor. It has been found that the proposed rotor provides a smooth controlled torque-slip curve, similar to a healthy induction motor. In the same time, the torque-slip curve avoids being negative at particular speeds of the torque-slip curve. Because the simulation is operated in current control, in this part of chapter, the relationship between torque and stator current has been deduced and found that the torque is positive proportional to the square of the stator current. In this chapter, it also has been discussed to have a short-pitched rotor to reduce the effect of the 15th and 21st harmonics. The results find that the short-pitched rotor compromises the performance of the motor for about 5%, but show little improvements in fault conditions. As a result, the short-pitched rotor is not considered in this project.

In the fifth part, the 54 slots rotor has been discarded due to the limitation in the size of the rotor and manufacture technical difficulty. Instead, a three-phase 18 slots fully pitched rotor has been taken into consideration. The newly proposed rotor has all the merits of the 54 slots one but easier in casting and manufacturing. The performance of the new rotor has been compared with the 54 slots rotor and it is found that the rotor resistance is smaller than the old one. In the next part the saturation, torque ripple and efficiency have been studied to ensure the performance of the 18 slot rotor is acceptable in all aspects.

4.14 Reference

1.   Wendling, P., et al. Two techniques for modeling an induction motor with skewed slots with time-stepping 2D-3D finite element method. in IEEE International Conference on Electric Machines and Drives, 2005. 2005.

2.   Nasar, I.B.S.A., The Induction Machines Design Handbook, ed. S. Edition. 2010, United State of America: CRC Pressof Taylor&Francis Group , an Informa business. 827.

Chapter 5 Prototype Construction

The components of the triple three-phase induction machine have been sourced from a number of companies.

The Stator lamination stack and case is from an existing ABB induction motor. The stator winding is assembled by a winding specialist company to achieve the best performance possible. The rotor lamination stack and rotor conductors are manufactured within the university workshop, which has extensive experience of building machine prototypes.

The final assembly was undertaken in the university research laboratory, where the machine was tested in the no-load condition, locked rotor condition, a range of loads and with a range of faults. The performance will be presented in the next Chapter. This Chapter will focus on the process of manufacture and the knowledge obtained in the process.

5.1 Stator processing

The stator in this project is adapted from an existing induction machine so that the results obtained can easily be compared to a conventional induction machine. Hence, another machine from the same manufacturer with the same specification has been bought, as can be seen in Figure 5 - 1.

Figure 5 - 1: The newly bought conventional induction machine

In order to achieve the fault-tolerant ability, the stator winding needs to be stripped out first. As seen in Figure 5 - 2, the end winding has been cut in order to strip the winding out, in the

meantime, as the manufacturer was not able to provide the number of turns along with this model, the author took time to count the number of turns, which was found to be 115.
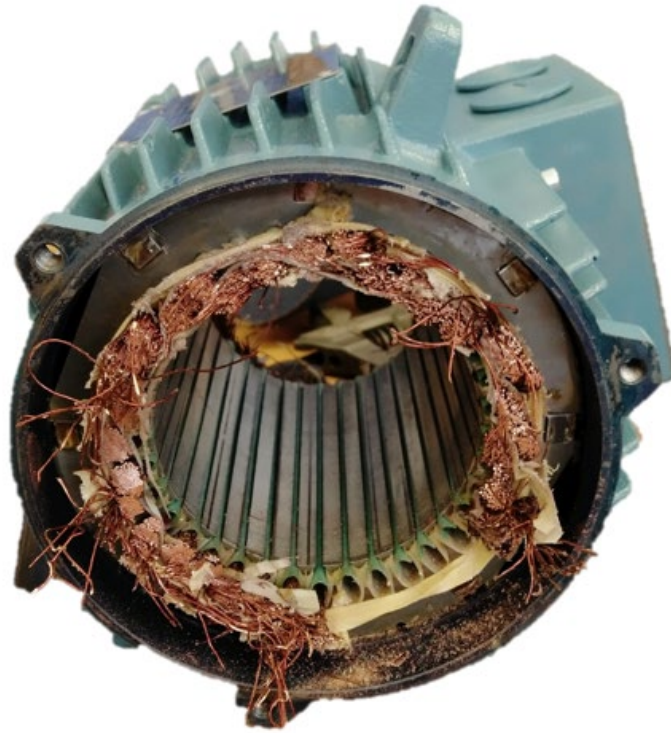
Figure 5 - 2: The stator winding that end winding has been cut

It is essential to clean the stator to ensure there are no conductors left in the stator or any damaged laminations. The stator has been cleaned, as seen in Figure 5 - 3.
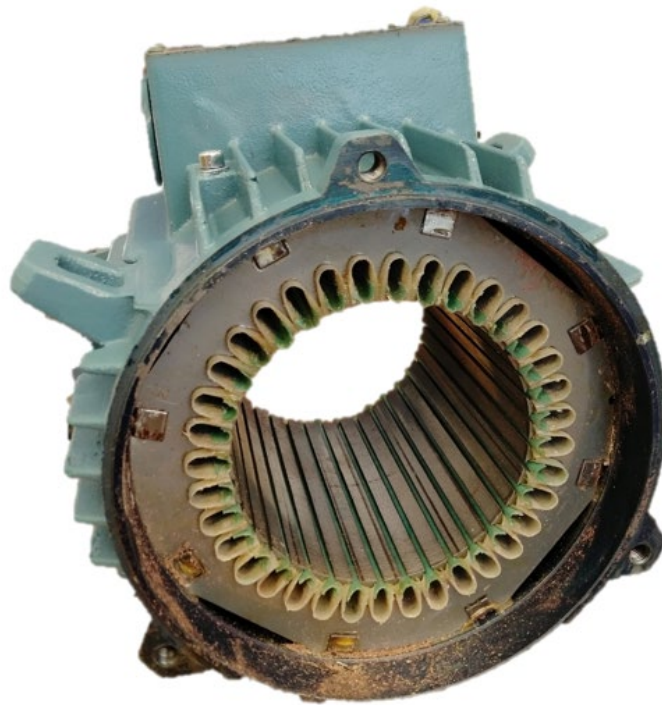
Figure 5 - 3: The stripped and cleaned induction machine stator

The stator winding was undertaken by a specialist winding, Sulzer, based in the UK, who rewound the machine with 0.56 mm 24SWG copper wire and 115 conductors in each slot. The rewound stator is shown in Figure 5 - 4, and in detail in Figure 5 - 5.

Figure 5 - 4: The re-wound stator

Figure 5 - 5: The winding configuration of the stator in detail

The conventional induction machine is shown in Figure 5 - 6, with an over-lapping winding for all phases. In contrast, the triple three-phase induction machine has three independent segments, which are physically, thermally, electrically independent from each other.

Figure 5 - 6: The conventional induction machine winding configuration

5.2 Rotor manufacture

The rotor was manufactured by specialist technicians in the university workshop. The thickness of the silicon steel sheet has been chosen to be 0.5mm. The stack length of the rotor is 151mm. Usually, the laminations are glued together with epoxy resin for a better stack factor. However, in this case, the laminations are fixed by have both sides screwed. the core should be kept at a certain pressure, usually $0.8{\sim}1.0 \text{ N} \cdot \text{m/m}^2 (8{\sim}10 \text{ kg/m}^2)$. Due to the large frictional force (such as the friction between the punch, the grooved rod, the shaft or the base) during press-fitting. The electrical steel sheet is further flattened after being pressed; the ageing shrinkage of

the punching sheet during operation causes the pressure between the core sheets to decrease. Therefore, the press-fit pressure is higher than 0.8 to $1.0N \cdot m/m^2$. In order to prevent the outer pressure core from being loosened by handling and collision, the actual stacking pressure is higher. Generally, the core for punching is 2 to $2.5N \cdot m/m^2$, and for the unpainted or oxidised sheet, the core can be 2.5 to $3.0N \cdot m/m^2$.[1]

The reason that this technique has been utilised is that the rotor is applied with a 20 degree skew effect. The glued silicon-sheet would make it impossible to separate the unwanted part with the rotor. In this way, the stacking factor is 97%. The 3D model has been shown in Figure 5 - 7.
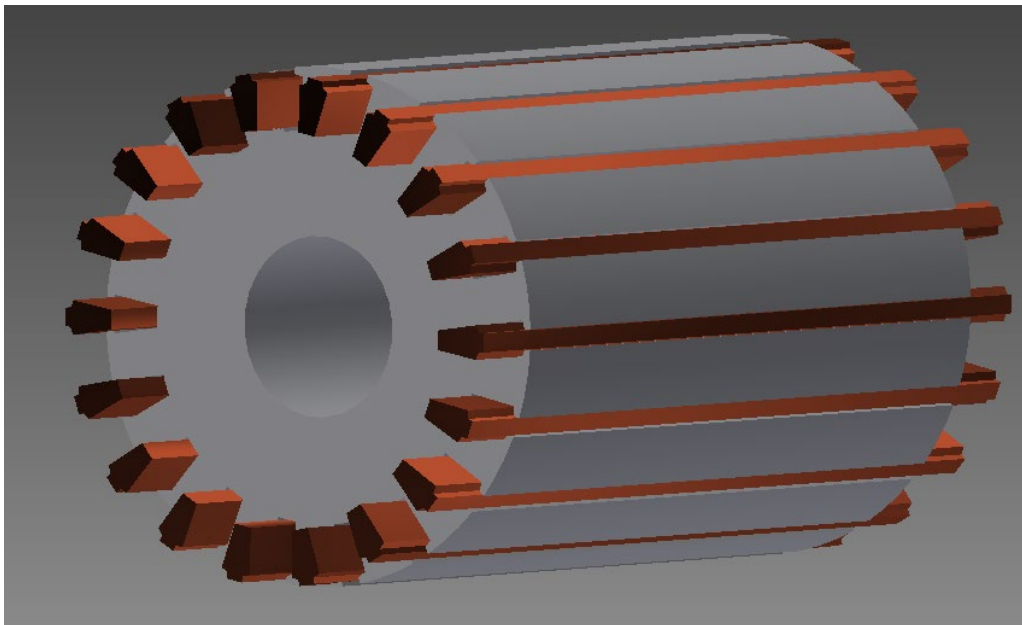
Figure 5 - 7: The 3D model of the proposed rotor

A "Fanuc RoBocut" wire erosion machine was used to cut both the lamination profile and the rotor conductors, as seen in Figure 5 - 8. The dielectric fluid, as seen in Figure 5 - 9, is used for electrical spark relief and heat dissipation to prevent thermal expansion of the material, which is a distinct advantage over the conventional machining and laser machining.

Figure 5 - 8: Fanuc RoBocut α-oic
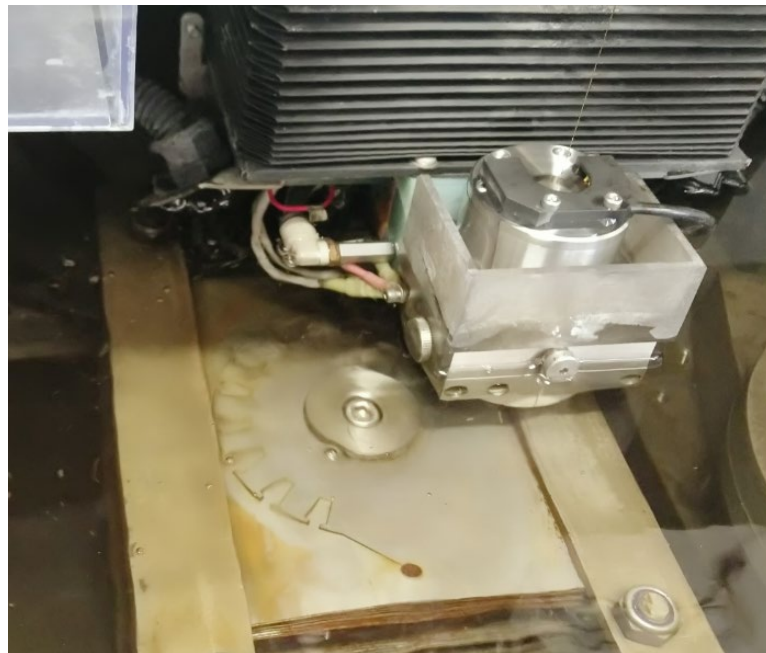
Figure 5 - 9: The machining process of the rotor

A 3D model of the rotor shaft is shown in Figure 5 - 10.
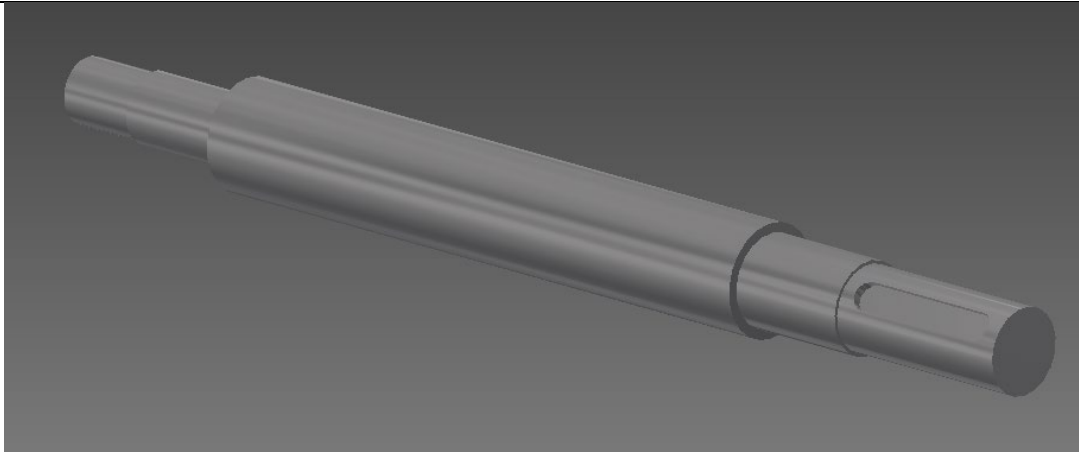
Figure 5 - 10: The 3D model of the shaft

The material that been used for manufacturing the shaft is stainless steel 304(1. 4301). Two materials that frequently used in electrical machine shaft has been compared in Table 17.

Table 17: The properties comparison between two materials for the rotor shaft

	Stainless steel 304	Aluminium 6082 T6
Density	8,000 Kg/m^3	2,710 Kg/m^3
Melting Point	1450 °C	575 °C
Thermal Expansion	17.2 x 10^{-6} /K	23.1 x 10^{-6} /K
Tensile Strength	720 MPa	280 MPa
Modulus of Elasticity	193 GPa	71 GPa

It can be seen that the stainless steel is heavier and hard to weld, but it shows great potential in deformation resisting under heat or under external force. In this project, a heavier rotor shaft would add a bit of the inertia of the complete rotor, but the speed of the rotor is no more than 1000 rpm, which means the starting torque would not be affected very much. The machining process of the rotor shaft would be using a lathe; the welding ability is not the priority here. However, the testing of the machine will involve a dyno machine, a lower modulus of elasticity would result in skew between both ends. In this case, the measuring results are not accurate. As a result, the shaft material is chosen as stainless steel 304.

Figure 5 - 11: The shaft being manufactured on a Colchester Lathe

The finished work has been shown in Figure 5 - 12, The first stage of assembling the rotor is separating the unwanted part of the silicon-steel sheet from the rotor. There is a bolt going through the middle to camp the lamination together.

Figure 5 - 12: The process of stripping the silicon-steel sheet from the rotor

As it has been discussed in Chapter 4, the rotor needs to be skewed by 10 degrees to achieve enhanced performance with less torque ripple and smooth stator current. As seen in Figure 5 - 12, skew has been applied to the rotor.

The rotor is then combined with the shaft, as it can be seen in Figure 5 - 13.
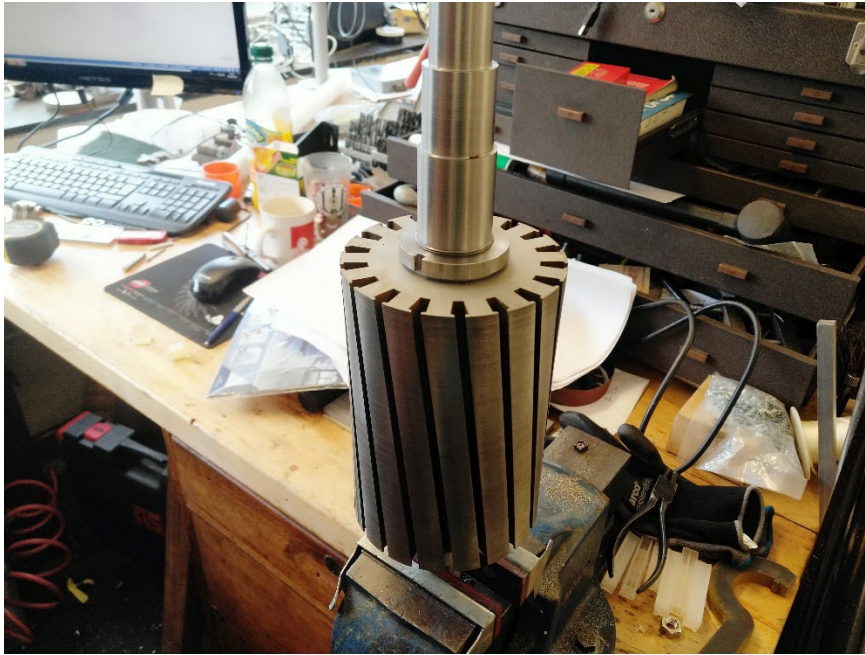
Figure 5 - 13: The complete rotor

5.3 Rotor winding manufacture

The final stage is inserting the conductors into the rotor. As mentioned in Chapter 4, in this project a wound rotor is necessary to enhance performance during the fault condition. The winding configuration can be seen in Figure 5 - 14.
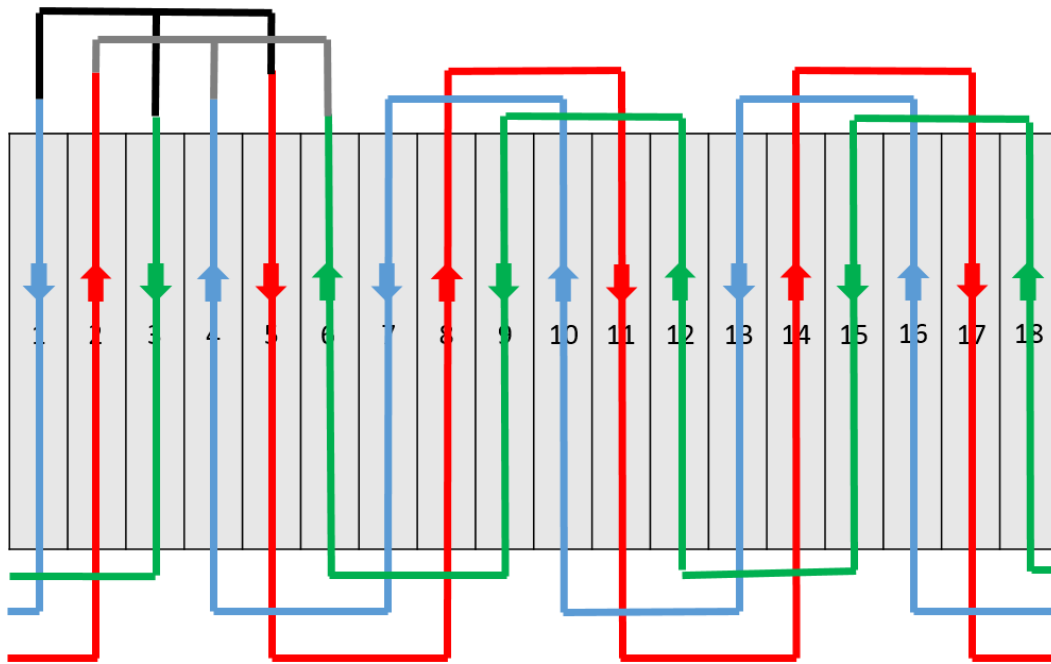
Figure 5 - 14: The rotor winding configuration

Although, the rotor winding configuration is fixed, there are many options in terms of rotor winding material and winding types.

The most common material for the induction rotor winding is aluminium and copper. The mainstream structure of an induction motor are squirrel cage motor and wound rotor motor. In the manufacture of industrial induction motors, squirrel cages are usually cast from aluminium. Aluminium has good electrical conductivity and a low melting point (660.4 ° C). The cost is also advantageous, so the cast aluminium rotor is the most popular option for induction motor. However, if the rotor is made of copper with higher conductivity, the efficiency of the motor will increase significantly.

The problem for that case is that the copper has a high melting point (1083 ° C), which makes the copper core challenging to cast.

The solution to this problem is often to turn to manufacture of a copper bar rotor by soldering. The manufacturing process is as follows: firstly insert the copper strip into the rotor slot and then solder the end windings on both sides (the end winding is usually manufactured by centrifugal casting, the centrifugal casting process can remove impurities and bubbles).

In this project, the end winding is screwed onto the copper rotor bars. Since the rotating speed is no more than 1000 rpm, screwing the end windings into the rotor bar provides more than enough robustness to the motor. The 3D model of the end windings can be seen in Figure 5 -

15. To complete the rotor, several different end windings are used to complete the winding connection, as seen in Figure 5 - 14.

The proposed rotor is shown in Figure 5 - 16. It can be seen that the rotor is skewed by 10 degrees and all slots are filled with copper bars. The insulation between the rotor bars and the silicon-steel sheet is formed by a Nomex slot liner. This particular kind of slot liner is the most widely used for both AC and DC motors. Its superiority reflects in thermal, mechanical, electrical, and chemical. According to their website, this slot liner remains good electric insulation under 220℃, and start to melt under 300℃. It's also capable of functioning under tough condition, such as mill drives and industry. Besides that, the Nomex slot liner is corrosion resistant and compatible with many types of common industrial liquid, such as varnishes and refrigerants.

Figure 5 - 17 also shows that there are three layers for the end winding connections in the rotor and they are insulated by two insulating boards. These boards hold the end-windings axially apart and prevent them from moving away from their designed position. Contact between end-windings could cause severe short circuit currents, which would lead to rotor faults.
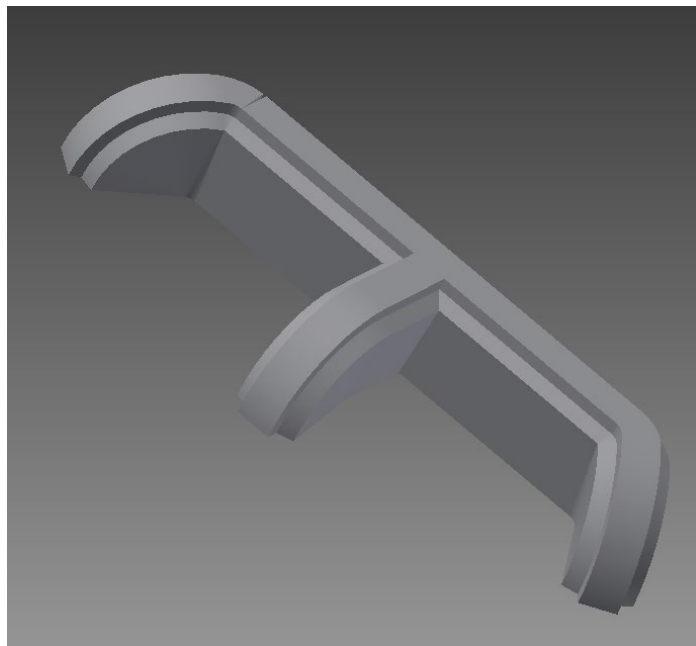
Figure 5 - 15: The 3D model of the end winding

Figure 5 - 16: The Top view of the proposed rotor
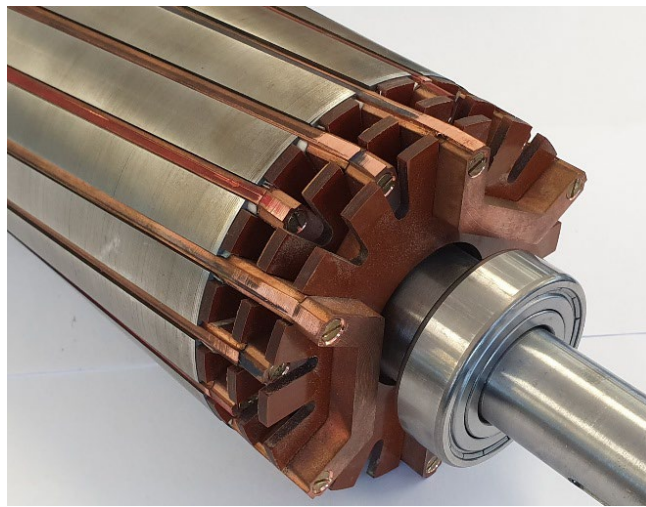
Figure 5 - 17: The side view of the proposed rotor

5.4 Test rig establishment

The test rig was assembled in the research lab with the help of technicians. The proposed motor was installed on to the bed plate by the couplings and supplied from a variable frequency three phase ac supply. A permanent magnet synchronous machine (PMSM) has been installed on the other side of the rest rig. This PMSM is working as a load machine, which is powered by another drive. There is a torque transducer connecting both machines, which is also connected to a monitor to display the torque and rotation speed in real time. An overview of the test rig can be seen in Figure 5 - 18.
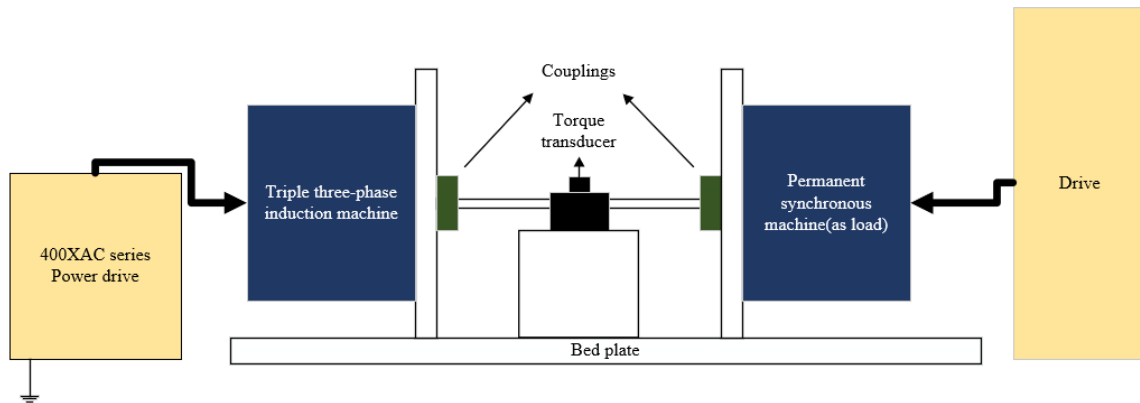
Figure 5 - 18: The schematic diagram of the test rig

Figure 5 - 19 shows, there is a connection unit that helps the triple three-phase induction machine to accomplish different winding connections and reproduce the fault condition.
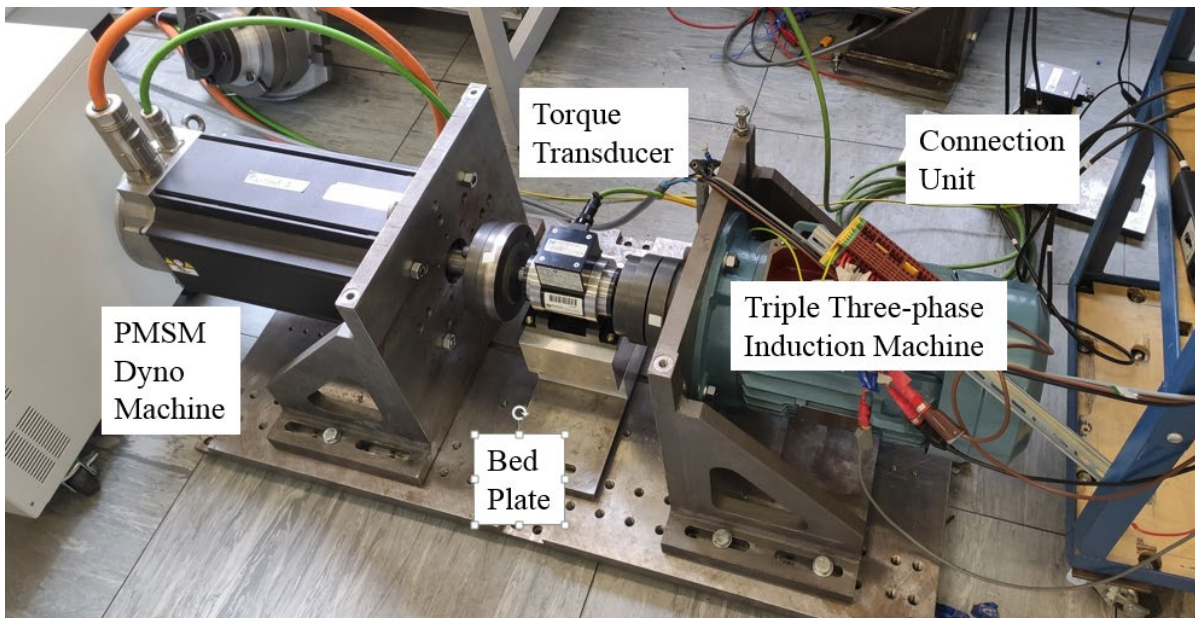
Figure 5 - 19: The overview photo of the test rig

As seen in Figure 5 - 19, there are 18 terminals for each segment have three phases with two ends connected with a connection unit.

Figure 5 - 20: The 400XAC series Power drive
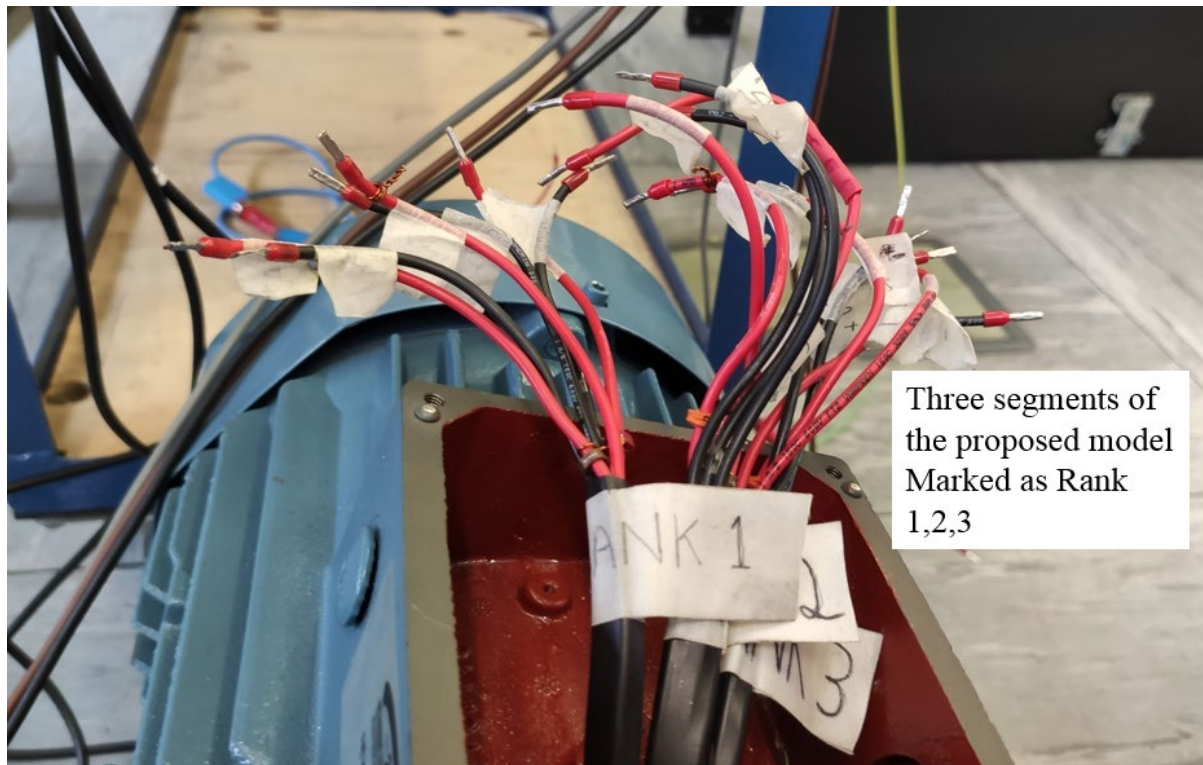
Figure 5 - 21: The terminals of the three segments in the proposed motor

As seen in Figure 5 - 22, the current probes, voltage probe and sliding rheostat has been displayed. The sliding rheostat is used for changing the resistance of each phase to help to understand the performance of the proposed motor under fault condition. The probes are connected to an oscilloscope, as seen in Figure 5 - 23.
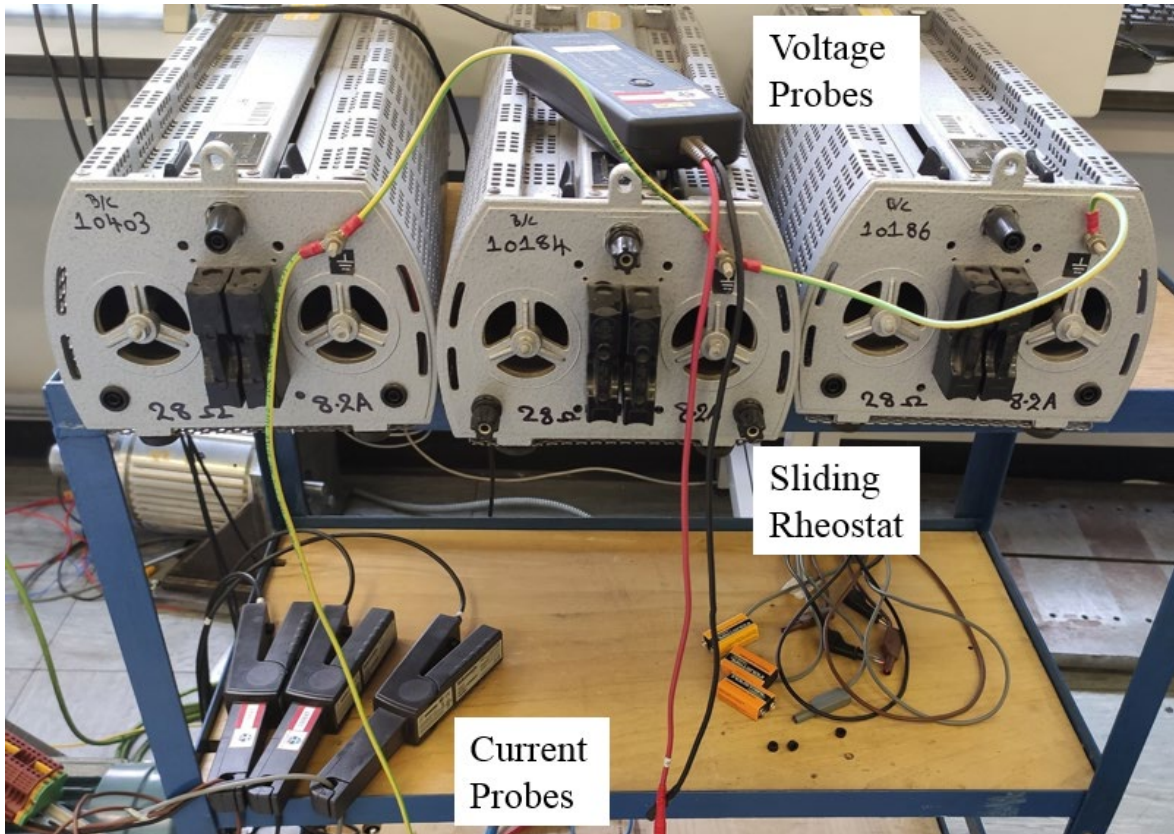
Figure 5 - 22: The equipment utilized to measure the performance of the proposed motor
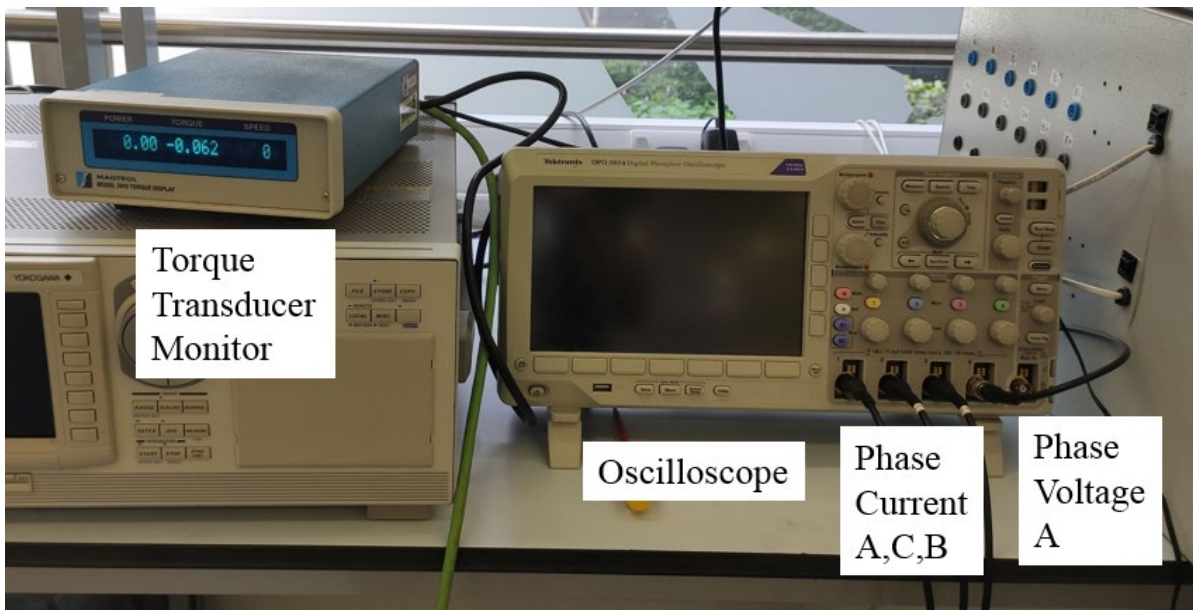
Figure 5 - 23: The equipment to monitor the performance of the proposed motor

The dyno machine is controlled by the drive system based on the direct torque control method, the drive can be seen in Figure 5 - 24. The dyno machine is used for speed control and torque consumption. A permanent magnet synchronous machine has been chosen in this project.

Figure 5 - 24: The drive system for the dyno machine

5.4 Conclusion

In this chapter, the author tries to paint a picture of how the proposed motor has been made and the test rig is established. Firstly, by removing and striping the end windings out of the stator

the conventional induction machine stator can be used directly and re-wound. Due to the winding of the triple three-phase induction machine is distributed winding, the rewinding job has been accomplished by a independent contractor. Secondly, with the help of the workshop, The rotor is casted from a stack of silicon-steel sheet into the designed shape. In the meantime, the rotor shaft is being machined on the lathe. By combining the rotor core, the shaft and the bearings, the rotor casting is completed. Thirdly, the rotor conductors and end windings is manufactured to achieve the designed electrical characteristic. Fourthly, the proposed rotor is assembled with the stator and the complete machine has been connected to a dyno machine to test the dynamic characteristic of the triple three-phase induction machine.

5.5 Reference

1.   Libert, F. and J. Soulard. Manufacturing Methods of Stator Cores with Concentrated Windings. in 2006 3rd IET International Conference on Power Electronics, Machines and Drives - PEMD 2006. 2006.

Chapter 6 Experimental Test Results

6.1 Locked-rotor test

For an asynchronous machine, the locked rotor test involves locking the rotor in a stationary position. Consider the equivalent circuit shown in Figure 6 - 1.
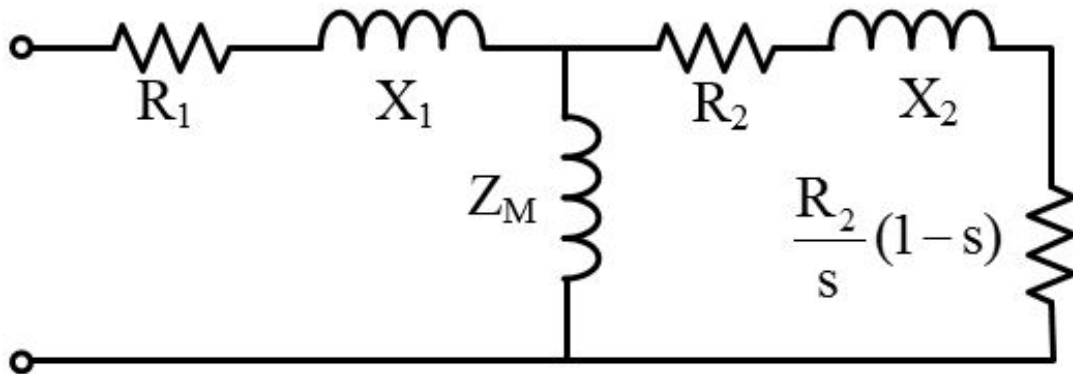
Figure 6 - 1: Equivalent circuit of the three lanes fault tolerant induction motor

In the locked rotor test, the rotor speed is zero, which means that the

$$\text{slip} = \frac{1000\text{-}0}{1000} = 1 \tag{6 - 1}$$

In this case, the transformed resistance from the rotor is

$$\frac{R_2}{s}(1\text{-}s) = 0 \tag{6 - 2}$$

Therefore, when the motor is operating under the locked rotor condition the equivalent circuit is simplified, which will help to calculate the fundamental parameters of the induction machine, as shown later in Figure 6 - 4.

In order to prevent the stator current from being too large during the locked rotor test, it is necessary to reduce the voltage to produce rated current at rated frequency. To avoid overheating the stator winding, the tests should be completed as quickly as possible, and repeated several times to increase the accuracy of the test. The active power, reactive power, current and power factor for each voltage condition are also recorded for calculation purposes. All parameters are RMS phase quantities.

Table 18: The locked-rotor test measurements for the prototype motor

Voltage(V)	Current(A)	Active Power(W)	Reactive Power(VAR)	Power factor	Assumed Temperature(°C)
17.1	5.6	53	78	0.557	20
16.8	5.52	52	75	0.565	20
16.5	5.43	50	73	0.561	20
16	5.26	47	69	0.559	20
15	4.92	41	60	0.561	20
13	4.26	30	46	0.545	20
11	3.59	22	32	0.564	20
10	3.27	18	26	0.562	20
9	2.94	14	21	0.538	20
7	2.304	8.9	13.4	0.552	20
5	1.64	4.5	6.7	0.555	20

The initial voltage applied was source employed was 17.1V, which gives the motor rated current of 5.6A.

Based on the recorded data, the voltage/current characteristic and the voltage/power characteristic are used to determine the resistance of the stator, as shown in Figure 6 - 2 and Figure 6 - 3. As seen in Figure 6 - 2, the voltage/current characteristic suggests that the voltage and the current are linearly related, indicating a constant impedance.
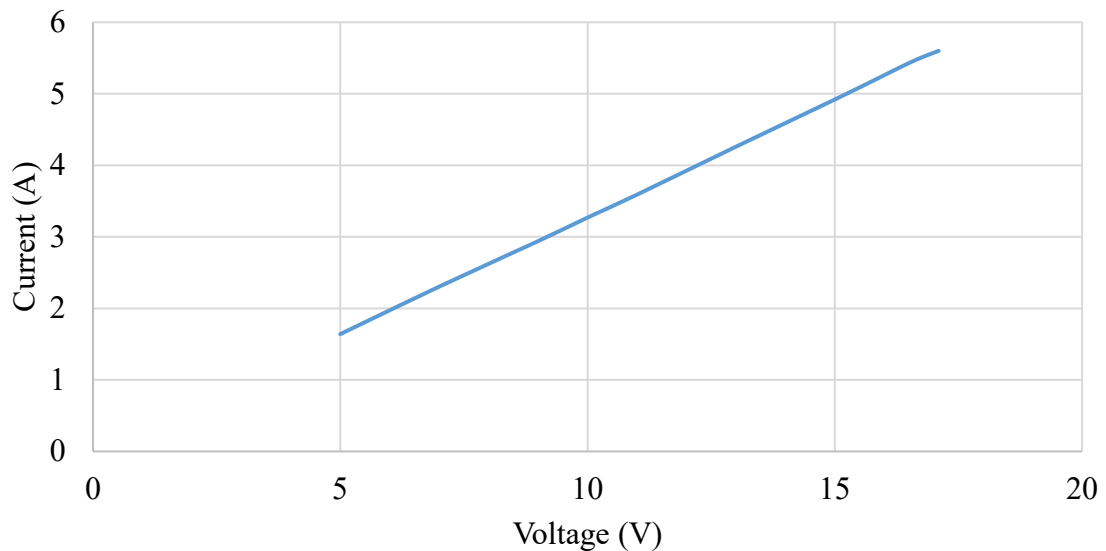
Figure 6 - 2: The voltage/current characteristic for the locked rotor test
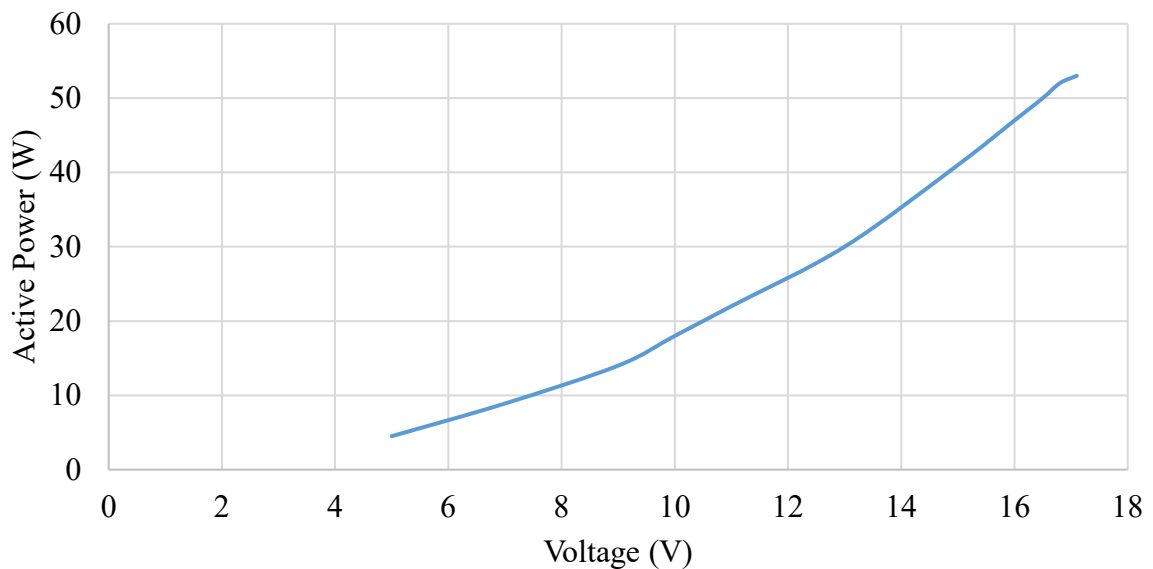
Figure 6 - 3: The voltage/power characteristic for the locked rotor test

When the rotor is locked the output mechanical power is zero and the mechanical friction loss is zero. The input active power is completely dissipated into the stator resistance. Hence,

$$P_{in} = 3I_1^2 R_1 + 3(I_2^{'})^2 R_2 \tag{6 - 3}$$

where P_{in} is the power input the stator, I_1 is the stator current, $I_2^{'}$ is the rotor branch current.

When the motor is locked, the slip is one, which means that the total mechanical power additional resistance is zero. It is known from the asynchronous motor equivalent circuit that the stator and rotor current is large, the excitation impedance is large and, as a result, the excitation branch is almost open circuit, which leads to the zero excitation current passing through the magnetizing inductance.

As a result, the locked rotor equivalent circuit is shown in Figure 6 - 4.
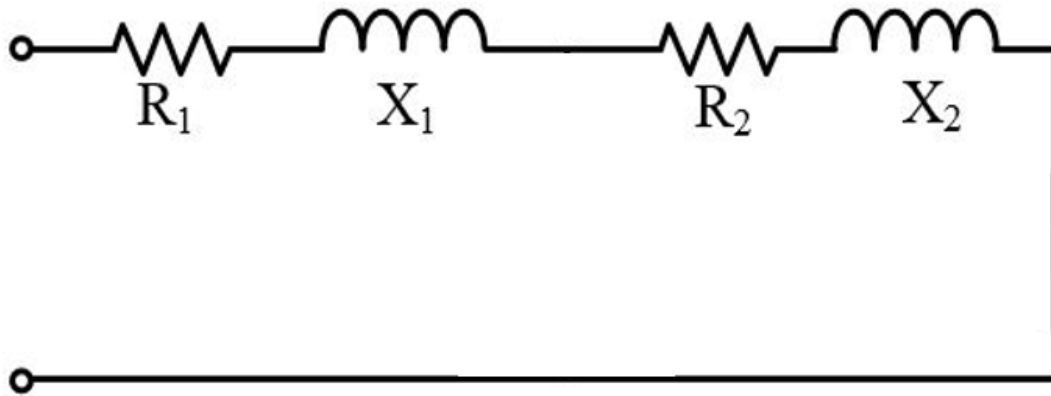
Figure 6 - 4: The simplified equivalent circuit for the locked rotor test

According to the voltage/current characteristic, assuming that the three segments are identical, the active power and the current for each segment is 1/3 of the measured value. Therefore, the $|Z_k|$, which is the absolute value of the impedance of one segment under locked rotor condition, can be calculated as

$$|Z_k| = \frac{U_k}{I_k/3} \qquad (6\text{ - }4)$$

Each set of data in Table 18 presents a value of $|Z_k|$, and the average is 9.12 Ω.

For the total resistance of the circuit R_k, according to the previous formula, the resistance of each segment can be calculated as

$$R_k = \frac{P_{ink}/3}{3(I_k/3)^2} \qquad (6\text{ - }5)$$

The average of R_k is 5.12 Ω, which is $(R_2 + R_1)$ in the equivalent circuit as shown in Figure 6 - 4. The inductance of the circuit is then calculated by,

$$X_k = \sqrt{|Z_k|^2\text{-}R_k{}^2} = 7.54 \,\Omega \qquad (6\text{ - }6)$$

Stator resistance R_1 is measured by a multimeter, which is 2.97 Ω. Then R_2 is calculated by,

$$R_2 = R_k\text{-}R_1 = 2.15 \,\Omega \qquad (6\text{ - }7)$$

In a medium-size induction machine, it can be assumed that $X_1 \approx X_2$, as a result,

$$X_1 \approx X_2 \approx \frac{X_k}{2} \approx 3.77\Omega \qquad (6\text{ - }8)$$

6.2 No-load test

In order to validate that the correct stator winding number of turns, the iron core quality, the alignment of the stator and rotor and an even airgap, the no-load test is then employed here for the induction machine testing.

The no-load test can also help to determine the parameters of the induction machine. In the no-load test, the speed is very close to the synchronous speed. In this test, the speed is around 998 rpm while the synchronous speed is 1000rpm. As the speed of the rotor is infinite close to the synchronous speed, the slip is very small, which means,

$$\frac{R_2}{s}(1\text{-s}) \approx +\infty \qquad\qquad (6 - 9)$$

As a result, the branch with the rotor transformed resistance is considered to be open circuit, thus the simplified equivalent circuit is shown in Figure 6 - 5.
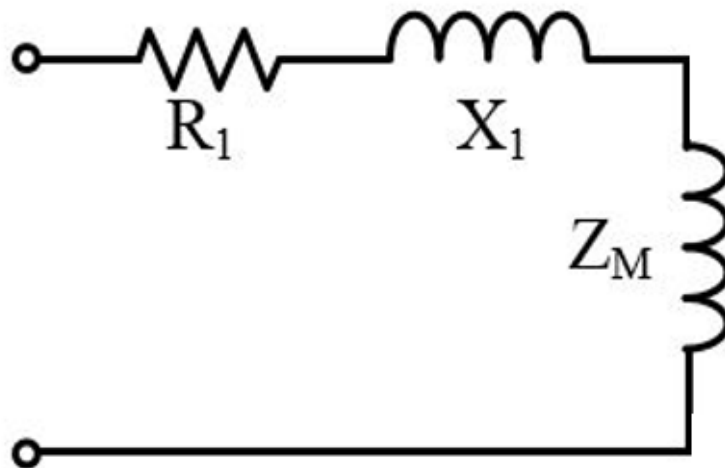
Figure 6 - 5: The simplified equivalent circuit for the no-load test

In this circuit, the stator resistance is a known value from multimeter measurement. And the stator reactance has been acquired by the locked rotor test. Consequently, the only unknown value is the excitation impedance Z_m. As shown in Table 19, the phase RMS voltage, the phase RMS current, the power source active and reactive power have been displayed. Ignoring the resistance of the excitation branch, the X_m can be calculated and are shown in Table 19.

Table 19: Datasheet for the no-load test of the proposed motor

No-load voltage	No-load current (A)	Input Active Power (W)	Reactive Power (VAR)	$\|X_m\|$ (Ω)
U_n = 76.98V	9.82	16	552	3.83
$0.85U_n$ = 65.3 V	7.49	14	488	4.73
$0.78U_n$ = 59.9V	6.76	13	403	4.88
$0.7U_n$ = 54.4 V	6.08	11	329	4.97
$0.64U_n$ = 49 V	5.42	10	264	5.06
$0.56U_n$ = 43.5 V	4.79	9	207	5.11
$0.49U_n$ = 38.1 V	4.18	8	158	5.14
$0.42U_n$ = 32.7 V	3.54	7	114	5.27
$0.36U_n$ = 27.3 V	2.96	6	80	5.25
$0.28U_n$ = 21.8 V	2.32	4	49	5.43
$0.21U_n$ = 16.3 V	1.75	4	28.2	5.34

The rated voltage of the conventional induction machine is 400 V (RMS line to line voltage). In this case, the triple three-phase induction machine with all three segments are connected in parallel with each other. The voltage should be 133.33 V (RMS line to line voltage). When the machine is with star connection, the phase voltage should be 76.98 V (RMS phase voltage).

Taking the rated voltage as an example, U_n = 76.98 V, I_n = 9.82 A, as the manufacture datasheet states, the no-load line current of the conventional induction machine is 3.8A. Therefore, for three paralleled connection, line current of each segment is 3.8A, the total line current is 11.4 A. However, the current in the no-load test is 9.8 A, which is 86% of the expected current. This difference can be caused by the special winding configurations of this fault-tolerant induction machine. The winding configuration aims to reduce the mutual coupling between segments. However, in the meantime, it inevitably increases the self-inductance. As shown in Figure 6 - 5, the higher X_1, which is the stator inductance, the smaller current can be achieved.

Under the no-load condition, taking rated voltage as an example, the impedance is calculated by

$$Z_n = U_n/I_n = 7.84 \ \Omega \qquad\qquad (6 - 10)$$

All reactance of this phase can be calculated by

$$|X_{km}| = \sqrt{(Z_n^2 - R_s^2)} = \sqrt{8.95^2 - 1.92^2} = 7.60 \ \Omega \qquad (6 - 11)$$

The stator reactance is 3.77Ohms, as a result, the excitation reactance is

$$|X_m| = |X_{km}| - X_s = 8.74 - 3.77 = 3.83 \ \Omega \qquad (6 - 12)$$

The testing results are shown in Figure 6 - 6, Figure 6 - 7, and Figure 6 - 8.
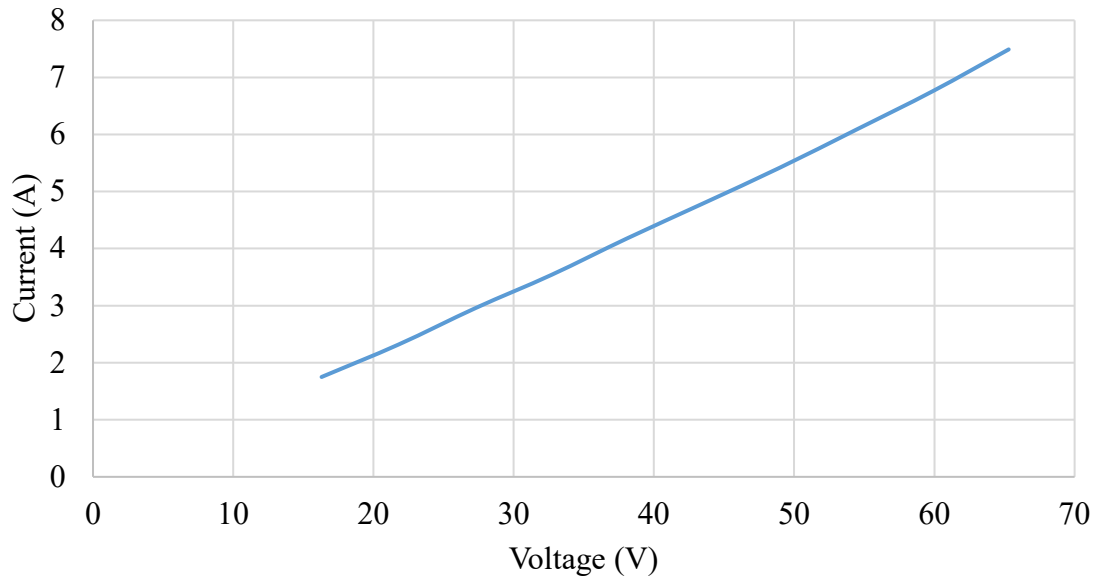
Figure 6 - 6: The voltage/current characteristic curve under no-load testing
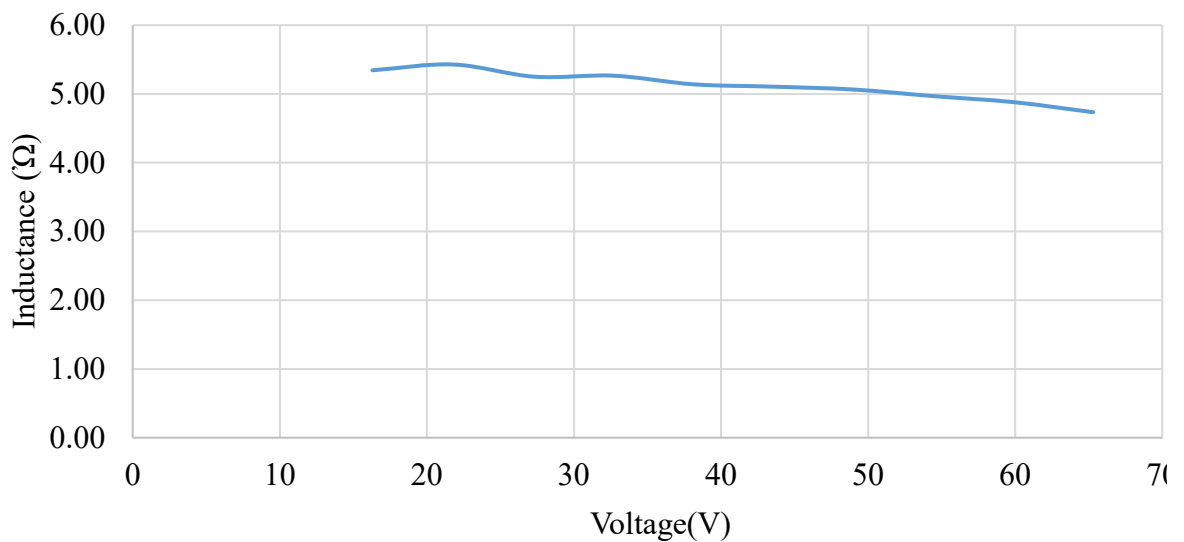
Figure 6 - 7: The excitation reactance of the proposed motor under no-load testing
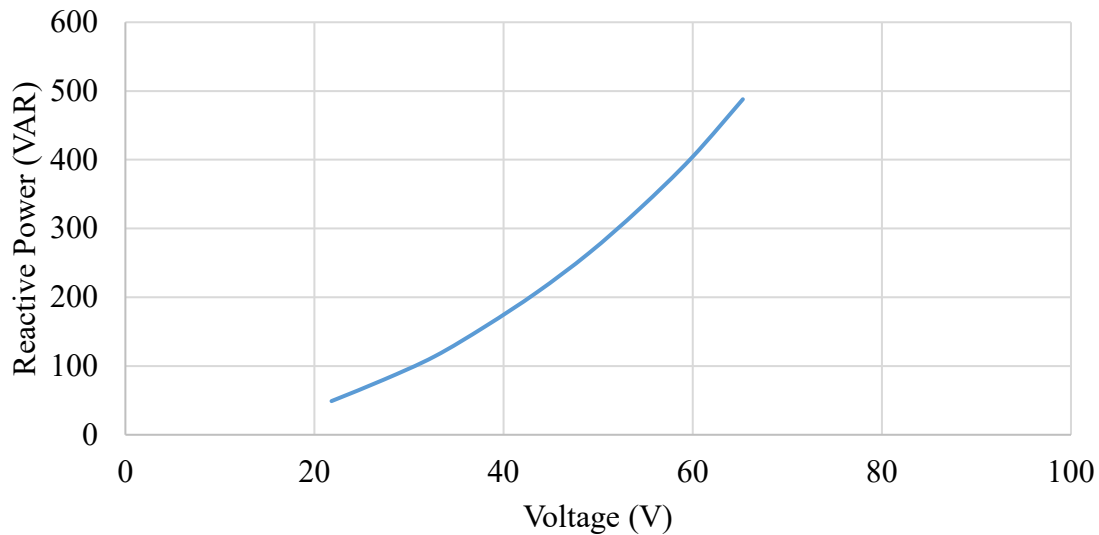
Figure 6 - 8: The reactive power under no-load testing

As shown in Figure 6 - 8, the relationship between the reactive power and voltage is a second-order positive correlation. The reactive power can be expressed as (6 - 13).

$$Q = \frac{U^2}{R}$$

(6 - 13)

The no-load current, as shown in Figure 6 - 6, is positive proportion to the voltage increasing. The current under the no-load condition can be expressed as

$$I_n = \frac{U_n}{R_1 + X_1 + X_m}$$

(6 - 14)

The R_1 and X_1 are constant, and their value have been calculated in the last section. The value of X_m is expected to be a constant with the varying voltage. The X_m is presented in Figure 6 - 7.

Hence, the equivalent circuit can be presented as in Figure 6 - 9.
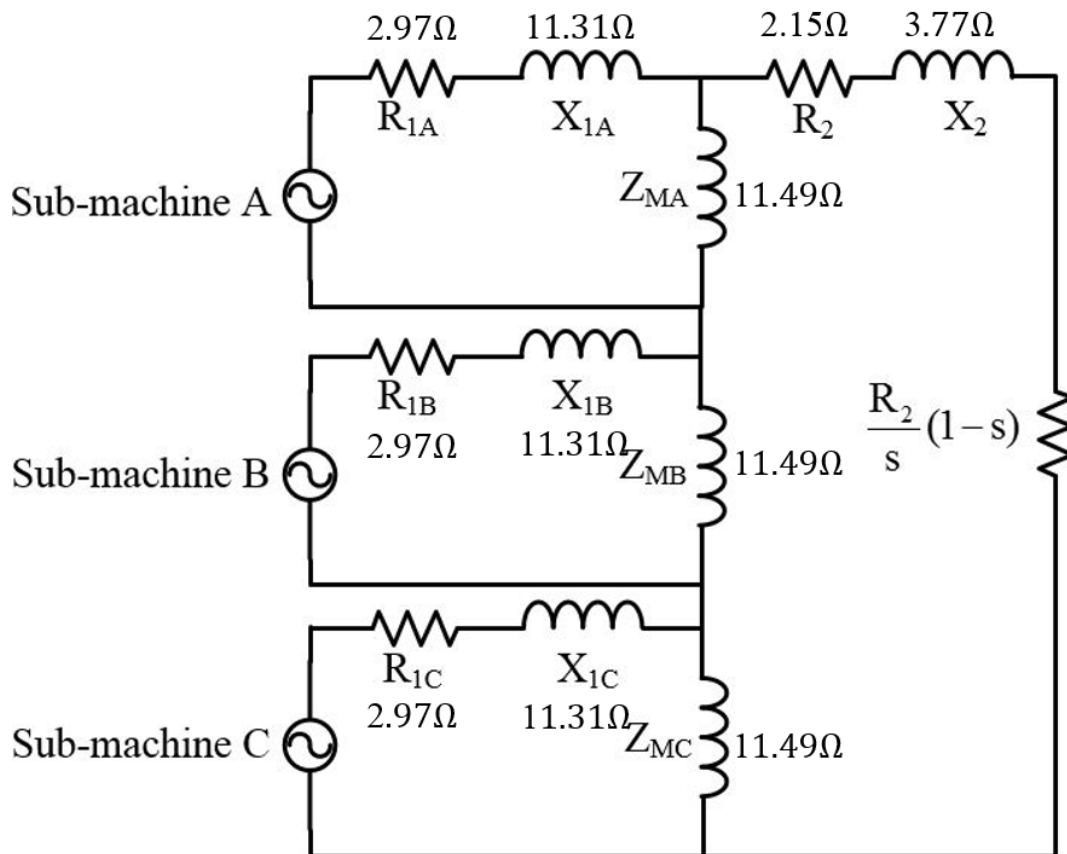
Figure 6 - 9: Equivalent circuit for all three segments of the induction motor.

There are three segments in the stator, which have been marked as Sub-machine A, B, and C, which is the segment A, B and C mentioned in the previous text. The final results are shown in Figure 6 - 9.

6.3 Torque performance calculation

As the equivalent circuit of the proposed motor has been derived from the tests above, the torque slip curve can be calculated to validate the accuracy of the parameters and set a baseline for further tests. All calculations are made on a per-phase basis. Under the healthy condition, the torque performance of the motor can be calculated by using an appropriate multiplying factor.

It is worth mentioning that the equivalent circuit shown in Figure 6 - 9 is a more detailed version of Figure 6 - 1, presenting the segmental stator design in practice. However, in the torque performance calculation, the simplified version in Figure 6 - 1 is employed, in which the stator is seen as a whole system.

The torque output of the induction motor can be expressed as,

$$T_m = \frac{m}{\omega_s} \frac{V_s^2 \frac{R_2'}{s}}{\left(R_1 + c\frac{R_2'}{s}\right)^2 + \left(X_1 + cX_2'\right)^2} \tag{6 - 15}$$

, where m is the number of phases in the stator, ω_s is the angular synchronous speed of the rotor in rad/s, s is the slip, c is a correction factor,

$$c = 1 + \frac{X_1}{X_m} \tag{6 - 16}$$

R_r' is the rotor resistance that is equivalent in the stator side equivalent circuit.

$$R_2' = \frac{m_s}{m_r}\left(\frac{N_s k_{ws}}{N_r k_{wr}}\right)^2 R_2 \tag{6 - 17}$$

$$X_2' = \frac{m_s}{m_r}\left(\frac{N_s k_{ws}}{N_r k_{wr}}\right)^2 X_2 \tag{6 - 18}$$

Where m_s, m_r are the phase number of the stator and rotor, the N_s and N_r are the number of coils per phase of the stator and rotor, and k_{ws} and k_{wr} are the winding factor of the rotor and stator respectively. In the meantime, the $\left(\frac{N_s k_{ws}}{N_r k_{wr}}\right)^2$ is called current factor, expressed as k_i.

Hence, k_i is calculated as 4.31, the ω_s is 52.36 rad/s, c is 2.06, R_r' is 27.77 Ω, and X_r' is 58.01 Ω. The torque performance can be predicted and shown in Table 20.

Table 20: Analytical prediction of the torque performance of the proposed machine.

Speed (RPM)	slip	Torque (N·m)
0	1	13.54078
100	0.9	14.43901
200	0.8	15.38023
300	0.7	16.31624
400	0.6	17.14638
500	0.5	17.67587
600	0.4	17.55539
700	0.3	16.22809
800	0.2	12.99423
900	0.1	7.407417
950	0.05	3.844503
1000	0	0
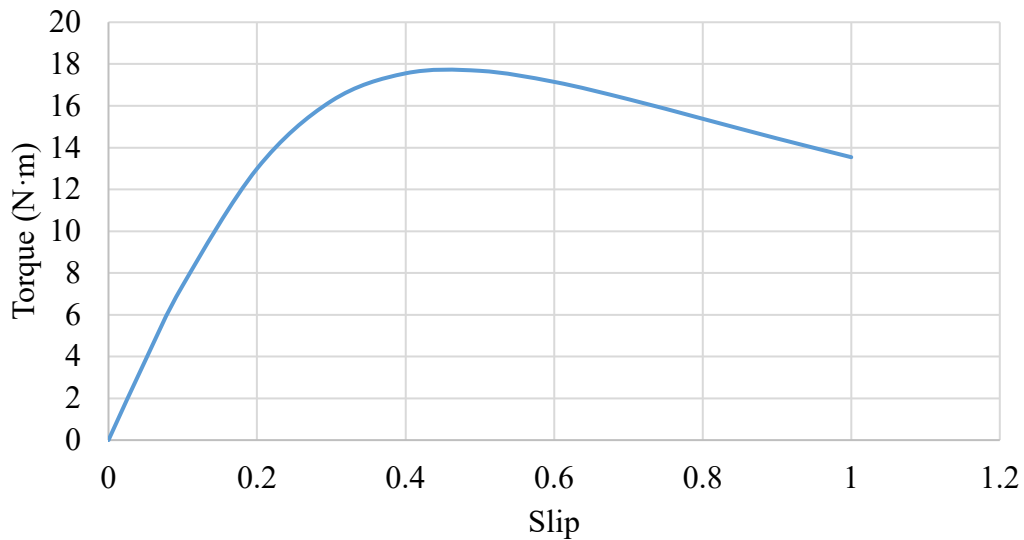
Figure 6 - 10: The predicted torque slip curve of the proposed machine under the healthy condition.

As shown in Figure 6 - 10, the torque slip curve shows that the induction motor reaches maximum torque around 0.45 slip (expected at lower slip), which is considered a low speed for an induction motor. The efficiency of the induction motor is highly related to the slip. For example, when the motor operates at 0.2 slip, the efficiency is around 80%. As a result, the lower the speed, the lower the efficiency that the motor can achieve. The slope of the motor approaching the maximum torque is directly related to the rotor resistance, which has mentioned in Chapter 2. The high rotor resistance is caused by the screwing of the end-winding in the rotor part.

6.4 Healthy condition motor test

To test the motor performance under the healthy condition, the motor is connected to a three-phase voltage supply. The test rig set-up is shown in Figure 6 – 11. The voltage source is set to 231 V, which is the RMS phase voltage of the star-connected motor. All three segments are connected in series and the terminals are connected to the power supply. The speed is controlled by the dyno. The testing results are shown in Table 21.
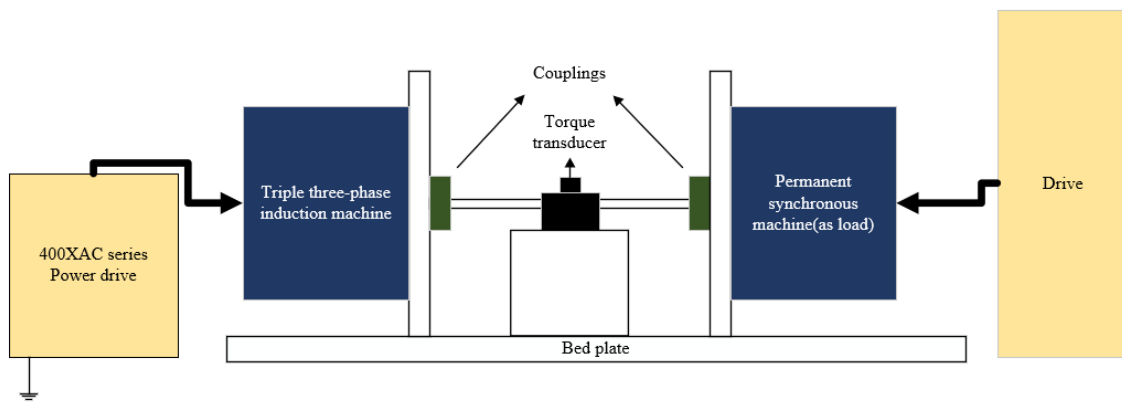
Figure 6 – 11: The schematic of the test rig.

Table 21: The test results under healthy condition with all segments connected in series

Speed (RPM)	Torque (N·m)
1000	0.7
950	5.3
900	9.56
850	12.84
800	15.32
750	16.72
700	17.36
650	17.96
600	17.96
550	17.78
500	17.86
450	17.34
400	17.02
350	16.52
300	16.16
250	15.78
200	15.34
150	14.84

The test results and analytical prediction are compared in Figure 6 - 12. The analytical prediction is obtained in Figure 6 - 10. The test results are consistent with the analytical prediction, although the slope of two curves is slightly different. This can be caused by the skin

effect of the rotor bars during the locked rotor test, which leads to a slightly higher calculation of rotor resistance.

The test results and FEA prediction are compared in Figure 6 - 13. The FEA results are not very compatible with the testing results. Due to the unpredictable contact resistance of the end winding, the FEA doesn't consider the rotor resistance. However, they all have similar maximum torque output, which means that the simulation and the test are under a similar H field from the stator side.
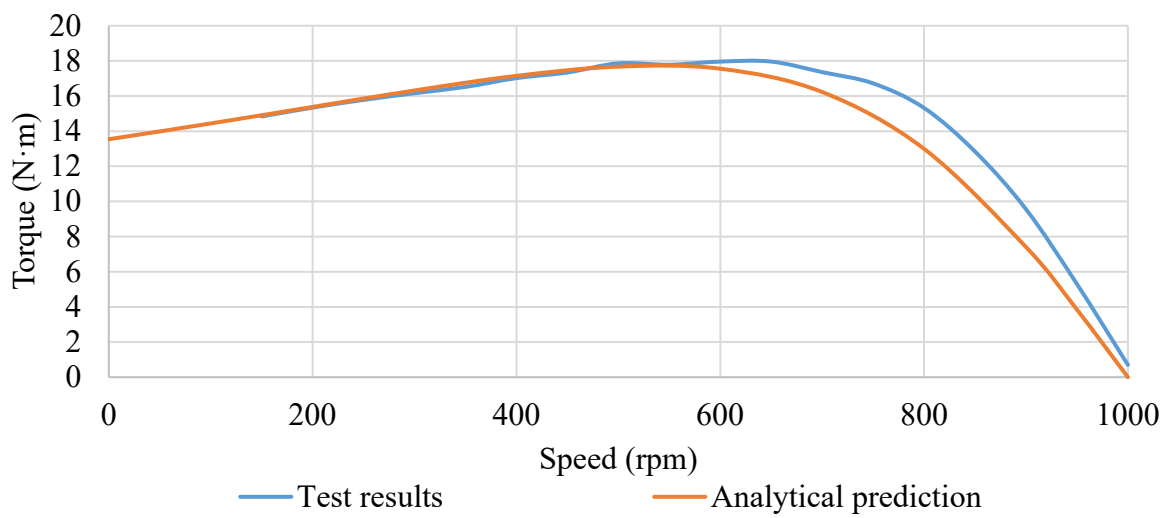
Figure 6 - 12: The torque slip curve comparison between the test result and the analytical prediction under the healthy condition.
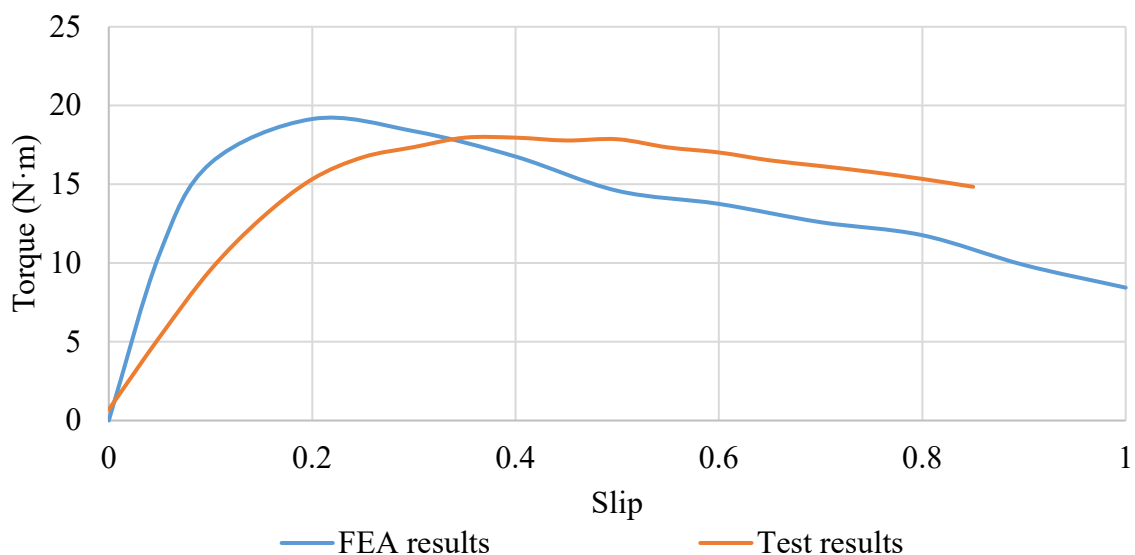
Figure 6 - 13: The torque slip curve comparison between FEA results and test results under healthy condition.

6.5 One segment short circuit condition

The one segment short circuit tests are carried out with the conventional machine and the proposed machine. Figure 6 - 14 shows the measured results with one lane short circuit. The torque slip curve of the proposed machine remains similar in shape but the magnitude is reduced to 4/9. This result validates that the proposed machine can produce torque under a short circuit.

As shown in Figure 6 - 14, the torque of the conventional cage rotor under one segment short circuit is, overall, larger than the proposed motor. However, the torque slip of the conventional motor is only recorded to the speed of 500 rev/min, which is the point when the power supply reaches its power limit. The stator current is 9.14 A, with an input of 50 Hz, 154 V RMS phase voltage. The proposed machine has been tested through the whole speed range. The maximum current is 6.77A, with the same input voltage condition as that employed in the conventional induction machine test. This proves that the conventional induction motor has less efficiency compared with the proposed motor under the short circuit condition.

In terms of the torque performance, the proposed machine is expected to be smaller than the conventional motor, and with a more controlled and steadier feature. As mentioned in Chapter 4, the cage rotor reacts to all sequences of the harmonics, whilst the proposed rotor only reacts to the fundamental harmonic which is the third harmonic and the multiple harmonics of three. By avoiding the impact of other harmonics, the proposed motor is able to operate under the fault conditions without the significant disturbance in the torque slip curve. However, with fewer harmonics for the rotor to react to, the total torque output is smaller.

As shown in Figure 6 - 14, there is a tip between 800 rev/min to 700 rev/min in the slip curve of the conventional induction machine, which is consistent with the simulation results in Chapter 3. This torque tip will occur under the two segments open circuit condition, however, it will be even worse, as the tip will reach the negative torque area. It can be seen that there is no data after 500rpm in the cage rotor short circuit condition. It is because, under this fault condition, there is too much current in the stator which tripping the alarm system of the drive prevents the experiment from continuing.
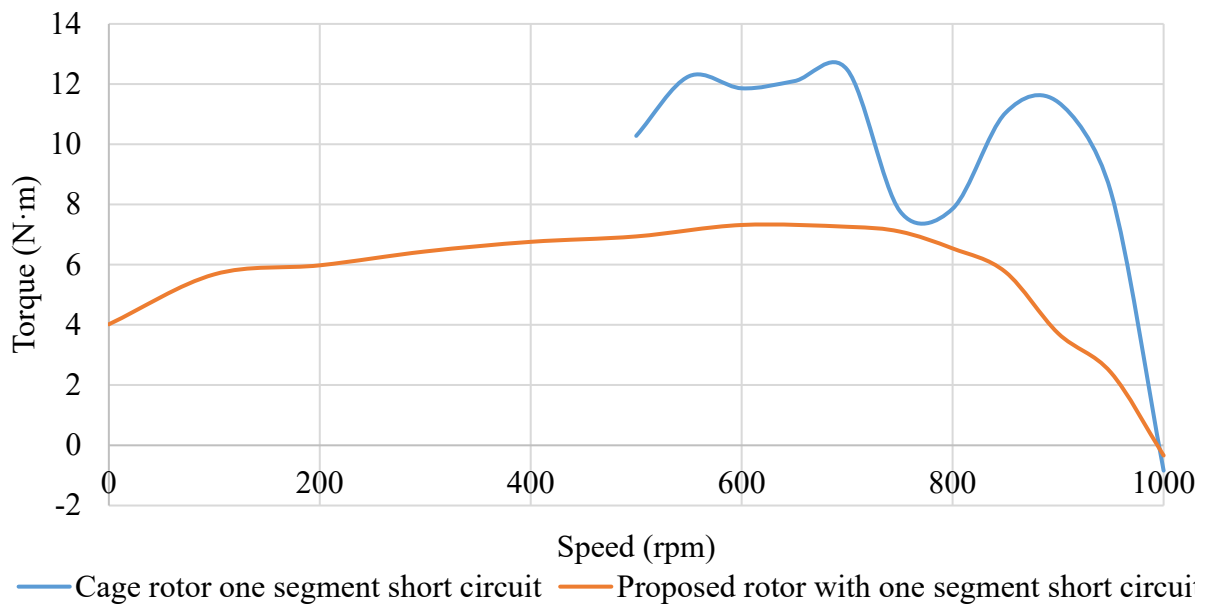
Figure 6 - 14: Experimental torque-speed curve comparison between the conventional and the proposed rotor under one segment short-circuit condition excited by 50 Hz rated voltage.

As presented in Figure 6 - 15, the torque of the proposed motor under a short circuit condition is smaller than the one under the healthy condition. The short circuit torque is about 4/9 of the one under the healthy condition, which is comparable with the discussion in Chapter 4.
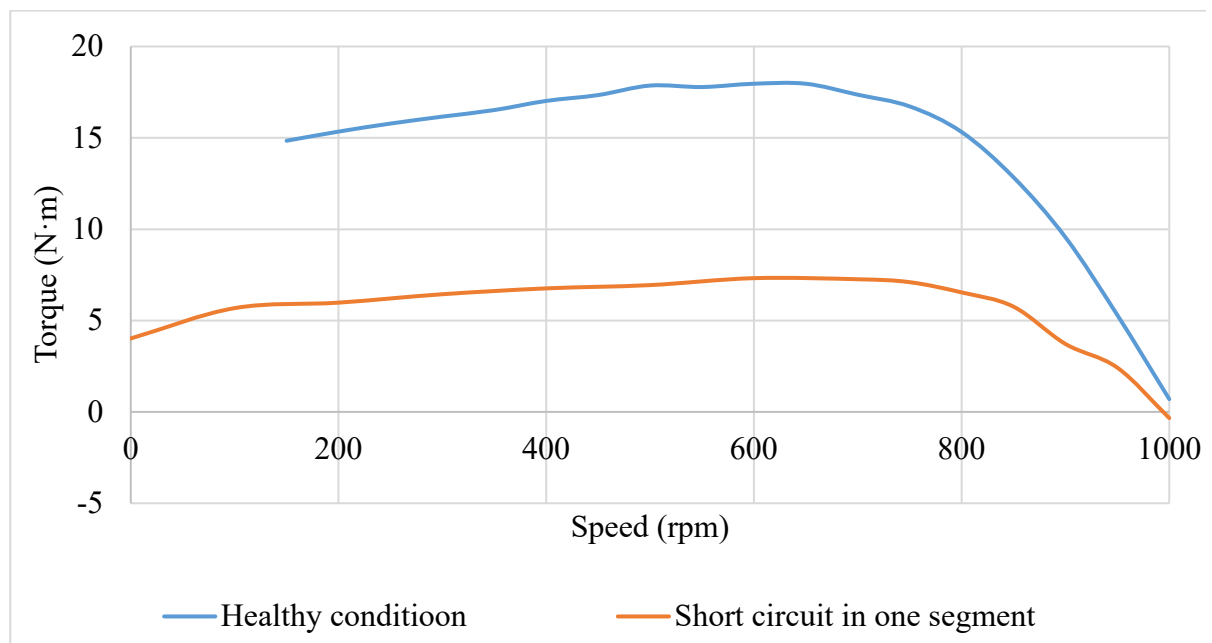
Figure 6 - 15: The experimental torque-speed curve comparison between the healthy condition and the one segment short circuit condition of the proposed machine with the rated voltage applied on each segment for all points.

Table 22 shows the difference between analytically predicted and experimental torque output of the proposed machine under one segment short circuit condition. It is noticeable that the peak torque measured is about 10% smaller than that predicted by the equivalent circuit. This needs further investigation: it is postulated that whilst the additional space harmonics do not produce torque, they do produce magnetic flux, which increases the leakage inductance of the machine and maybe the cause of this effect. The main rotor fields linking the shorted stator segment which would drive a current and create a drag torque.

Table 22: The torque comparison between the healthy condition and one segment short circuit.

Speed(RPM)	Healthy (N·m)	$\frac{4}{9}$ of the healthy torque (N·m)	One segment short circuit (N·m)
1000	0.7	0.311	-0.338
950	5.3	2.355	2.42 (2.6%)
900	9.56	4.24	3.72 (12.2%)
850	12.84	5.689	5.76 (1.2%)
800	15.32	6.808	6.54 (3.9%)
750	16.72	7.431	7.1 (4.5%)
700	17.36	7.716	7.26 (5.9%)
600	17.96	7.982	7.32 (8.3%)
500	17.86	7.938	6.94 (12.6%)
400	17.02	7.564	6.76 (10.6%)
300	16.16	7.182	6.44 (10.3%)
200	15.34	6.818	5.98 (12.3%)
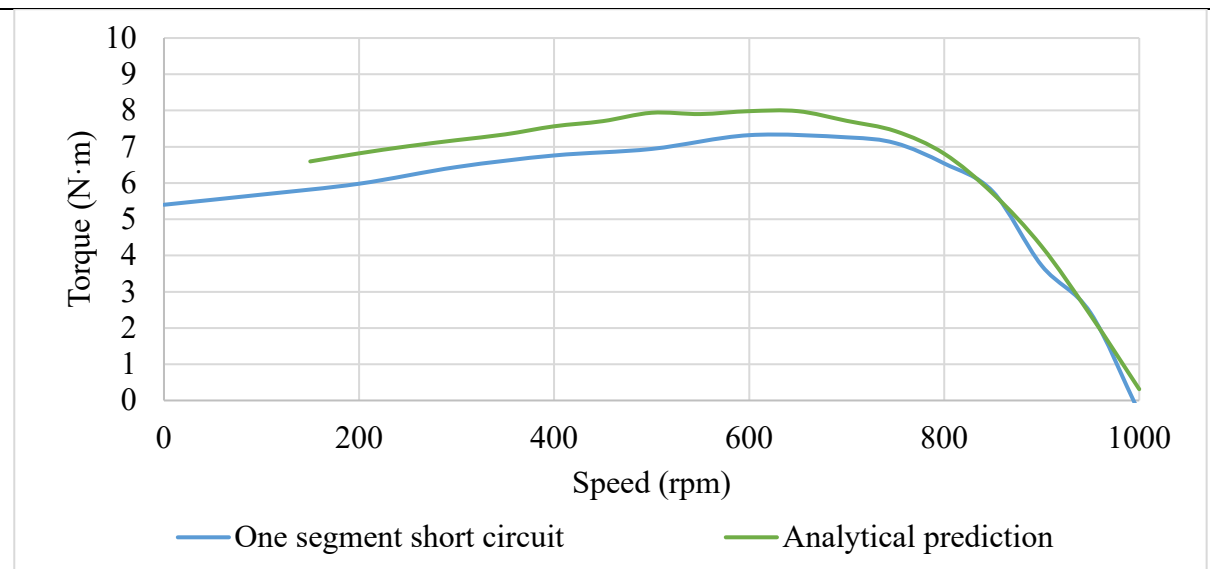
Figure 6 - 16: Experimental torque-speed curves of the proposed machine under one segment short-circuit condition with the rated voltage applied on each segment for all points.

As seen in Figure 6 - 16, the two lines represent the test results under one segment short circuit and the analytical prediction from the previous test and equivalent circuit, respectively. In the meantime, the two lines have a high degree of similarity, which means that the torque characteristics of the motor in the case of short circuit are consistent with the principle described above. In other words, the success of this experiment not only proves that the proposed motor presented in this thesis can be operated under extreme conditions but also verifies the relationship between the torque and the supplied current of the motor under the premise of eliminating interference harmonics.

6.6 Conclusion

This chapter focuses on the testing work of the proposed motor, which includes the calculation of the equivalent circuit of the proposed machine, analytical prediction of the machine torque performance, and the comparison of the torque-slip curves between the proposed machine and the conventional induction machine under healthy and fault conditions.

This chapter starts with a locked rotor test, also known as the short circuit test. Through this test, some parameters of the single-phase equivalent circuit are obtained. Following the locked rotor test, the no-load test has been carried out to find out the rest parameters in the single-phase equivalent circuit. With all the parameters obtained from the locked rotor and no-load tests, the analytical torque-slip curve of the proposed motor under the healthy condition is obtained.

Afterward, the test results of the proposed machine under the healthy condition are presented. The result has been compared with the analytical prediction and with the FEAs. It has been found that the analytical prediction is consistent with the test result. However, the FEA result is not comparable to the experimental result as the contact resistance of the rotor end winding is unpredictable and hasn't been considered in FEAs.

The experimental results of the proposed machine under the short circuit condition are presented in the end. The motor performs well in the short-circuit condition. Comparing to the cage rotor, the overall torque-slip curve of the proposed motor is lower, which is expected due to the loss of other harmonics. The proposed motor cannot work with a cage rotor smoothly but can work with the proposed rotor in a smoothly controlled manner. Furthermore, it is experimentally shown how, for the first time, an induction machine with multiple lanes can continue to produce torque in the event of a single lane short-circuit.

Chapter 7 Conclusion and Future Work

This thesis has investigated the performance of the triple three-phase induction machine under one segment, and the two segments open circuit as well as the short circuit between phases. To fully understand the performance, this thesis has utilised a current sheet model to quantify the harmonics' contribution to the torque performance. Furthermore, a new rotor has been proposed to optimise the performance of the triple three-phase induction machine. The future work has been attached to this chapter as well.

7.1 Triple three-phase induction motor

A triple three-phase induction stator has been proposed in this thesis. As established in the previous text, the triple three-phase induction machine divides the stator into three segments. In addition, any two of them are electrically, physically and thermally isolated. Compared to a conventional induction machine, the reliability is significantly enhanced. Additionally, the efficiency and torque density has been proved to be higher than the conventional motor under the healthy condition.

In this thesis, considering the comparison between the triple three-phase induction machine and the conventional induction machine, the stator structure, the number of turns, and the paralleled path and type of wire gauge have been kept the same. The torque slip curve was first compared with the performance of a conventional induction machine, and the figures have been confirmed to be appropriate. Furthermore, the same motor was simulated under one segment and two segments open circuit conditions, where it has been found that in the medium speed part of the torque slip curve, the performance is poor, even showing some negative torque.

7.2 The current sheet model

A current sheet model has been proposed to study the essence of the poor torque performance found in the triple three-phase induction machine. The current sheet model utilised a few small current slots to produce the same MMF in the air gap without harmonics distortion. In this project, only the first ten harmonics have been taken into consideration. Each harmonic has been simulated individually to obtain the torque slip curve for that specific harmonic. All the harmonics have been placed onto the same figure according to their different synchronous speeds. Moreover, all the harmonics' linear superposition is compared with the motor simulation results under two segments open circuit condition; the curves are similar to each other.

Besides that, the performance has been studied and found that the fourth and fifth harmonics provide positive torque from speed zero rpm to approximately 700 rpm and negative torque from 700 rpm to 1000 rpm. In this case, due to the large amplitude of those two harmonics, the torque of the two segments open circuit condition reached negative at about 800 rpm, which indicates that the fourth and fifth harmonics are the reason that the triple three-phase induction machine performs poorly during the medium speed.

7.3 The proposed new rotor

The purpose of the new rotor is to avoid the impact of the fourth and fifth harmonics. The new rotor winding is designed to link the six-pole field and all integer harmonics of it. Because it is three-phase, star-connected, triple harmonics are removed, so the only spatial harmonics left are the fundamental three pole pairs, along with 15, 21 and 33 pole pairs. After the study of the harmonics spectrum, those harmonics show little impact on the torque performance of the triple three-phase induction machine. As a result, modifying the rotor from a cage rotor to a winding rotor should keep the rotor only responsive to the three-pole pairs harmonic.

Many winding configurations have been simulated and discussed. Many of those winding connections have been proved to either reduce the torque performance or to be too complicated to cast in the manner of manufacturing technique. In the last section, this thesis concluded that a fully pitched 18 slot rotor is the best compromise in this situation.

7.4 Future work

- The proposed motor has been tested under a short circuit condition and the healthy condition. For this motor to be operated under open circuit condition, however, the power source has to be a current-controlled one; the simulation has verified this conclusion. Due to the insufficient experiment equipment, the motor performance under open circuit condition has only been simulated in the FEA software. The future work shall include the motor performance under one and two segments open circuit condition.

- The torque performance is reduced because the essential principle of the new motor is to make the fourth and fifth harmonics not respond to the rotor. By doing so, a part of the energy is lost. The reason those two harmonics provide negative torque is that the magnetic field rotates in the direction that does not provide positive torque for them. If some methods could be found to take advantage of that part of energy, the torque would greatly increase, as would the efficiency under the fault condition.

Appendix

1. Multifunction script for analysing the H field spectrum (.m)

```matlab
clear all
clc
close all

theta_s  = linspace(0,1080,1080);
d_theta = deg2rad(theta_s);
v = 0;
omega    = 2*pi*50;
%MMF      = zeros(1,numel(theta_s));
% t         = 1/(2*50)/2;
% n          = 0;
x = linspace(0,2*pi,numel(theta_s)/3);
%t=linspace(0,0.6,200);

MMFA_healthy_pole = sin(x);
MMFB_healthy_pole = sin(x-2/3*pi);
MMFC_healthy_pole = sin(x-4/3*pi);

Total_MMFA = [ zeros(1,numel(theta_s)/3) MMFA_healthy_pole
zeros(1,numel(theta_s)/3) ];
Total_MMFB = [ zeros(1,numel(theta_s)/3) MMFB_healthy_pole
zeros(1,numel(theta_s)/3) ];
Total_MMFC = [ zeros(1,numel(theta_s)/3) MMFC_healthy_pole
zeros(1,numel(theta_s)/3) ];

C_1 = 0;
C_2 = 0;

Q = zeros(1,20);
P = zeros(1,20);
% Q = 0;
% P = 0;
S_1 = 0;
S_2 = 0;
t = 0; % initial time
x = 0;
H_peak1 = zeros(50,1);
H_peak2 = zeros(50,1);
H_t1 = zeros(540,1080);
H_t2 = zeros(540,1080);
r = 0.0517625;
F_theta = zeros(20,1080);
F_theta1 = zeros(20,1080);
F_theta2 = zeros(20,1080);
% F_theta = zeros(1,1080);
MMF_harmonics = zeros(20,1080);
spectrum = zeros(20,2);
while t <= 0.1
%
%     t = t + 0.001;
%

    MMFA = Total_MMFA * sin(omega*t);
```

```matlab
    MMFB = Total_MMFB * sin(omega*t-2*pi/3);
    MMFC = Total_MMFC * sin(omega*t-4*pi/3);


    MMF  = 2451.68266*(MMFA + MMFB + MMFC);
    harmonics_number = linspace(1,20,20);

%    checking the mmf
    figure(3)
    plot(deg2rad(theta_s),MMF)
    grid on
    title('original MMF')
%
    coefficients = fftv5(MMF);
    a_n = 2*real(coefficients(2:end));
    b_n = -2*imag(coefficients(2:end));
    a_0 = real(coefficients(1));



    for n = 1:540
%          n = 2;
        MMF_harmonics(n,:) =
a_n(n)*cos(n*deg2rad(theta_s)/3)+b_n(n)*sin(n*deg2rad(theta_s)/3);
%         [max_MMF,index] = max(MMF_harmonics,[],2);
%         H_peak = (max_MMF*n)/2*r;
%         H_t(n,:) = H_peak(n) * sin(n*deg2rad(theta_s) - omega*t);

    end

%    [max_MMF(1000*t,1),index] = max(MMF_harmonics(1,:),[],2)

    if t == 0
%        Q = a_n(1:20);
      Q = a_n(1:50);

    end

    if t == 0.005
%        P = b_n(1:20);
      P = b_n(1:50);
      v = 1;
    end

  if t>=0.005
  for v = 1:50


    syms C_1 C_2
    S_1 = P(v) - C_1 + C_2;
    S_2 = Q(v) - C_1 - C_2;
    [C_1,C_2] = solve(S_1,S_2,'C_1','C_2');
    C_1 = vpa(C_1);
    C_2 = vpa(C_2);
%     C_1 = 100;
%     C_2 = 200;

    F_theta(v,:) = C_1*cos(omega*t-
v*deg2rad(theta_s)/3)+C_2*sin(omega*t+v*deg2rad(theta_s)/3);
    F_theta1(v,:) = C_1*cos(omega*t-v*deg2rad(theta_s)/3);
    F_theta2(v,:) = C_2*sin(omega*t+v*deg2rad(theta_s)/3);
    [max_MMF1,index] = max(F_theta1,[],2);
```

```matlab
    [max_MMF2,index] = max(F_theta2,[],2);
    H_peak1(v) = (max_MMF1(v)*v)/(2*r);
    H_peak2(v) = (max_MMF2(v)*v)/(2*r);
    H_t1(v,:) = H_peak1(v) * sin(v*deg2rad(theta_s) - omega*t);
    H_t2(v,:) = H_peak2(v) * sin(v*deg2rad(theta_s) - omega*t);


    v = v+1;
    end
   end


   t = t + 0.001;

%     figure (1)
%     plot(deg2rad(theta_s),sum(F_theta))
%     grid on
%     axis([0 20 -1.5 1.5])
%     title('F_theta')

%     H = H_t1(1,:);
%
    figure (1)
    plot(d_theta,H_t2(1,:))
    figure (1)
    plot(deg2rad(theta_s),F_theta)

% %


  % Modified compass figure with higher radial limit
%
%     figure(1);
%
%     compass(a_n(1),b_n(1))

%     max_lim = 0.5;
%
%     x_fake=[0 max_lim 0 -max_lim];
%
%     y_fake=[max_lim 0 -max_lim 0];
%
%     h_fake=compass(x_fake,y_fake);
%
%     hold on;
%
% %     h=compass(a_n(1),b_n(1));
%
%     set(h_fake,'Visible','off');
%


%     checking the reconstructed waveform
    figure(4)
    plot(deg2rad(theta_s),sum(MMF_harmonics)+a_0)
    grid on
%     axis(0,20,-1.5,1.5)
    title('harmonics sumup')
% % %
     %c = c+1;
%     spectrum(:,1) = max(MMF_harmonics,[],2);
%     spectrum(:,2) = min(MMF_harmonics,[],2);

%      figure(4)
```

```
%        stem(harmonics_number,spectrum)


%        figure(3)
%        plot(theta_s,MMF_harmonics(1,:))
%        grid on
%        axis([0,600,-0.35,0.15])
%
%        cosines coefficients(only the triple harmonics matters)
%        figure(1)
%        stem(1:numel(a_n),a_n)
%        grid on
%        axis([0,30,-1000,1000])
%        title('cosine harmonics coefficients')
% %
%        % sine coefficients(only the triple harmonics matters)
%        figure(2)
%        stem(1:numel(b_n),b_n)
%        grid on
%        axis([0,30,-1000,1000])
%        title('sine harmonics coefficients')
% % %

%        figure(2)
%        plot(theta_s,MMF,...
%        theta_s,MMFA,...
%        theta_s,MMFB,...
%        theta_s,MMFC)
%        grid on
%        legend('Total','PhaseA','PhaseB','PhaseC')
%        axis([0,1080,-1.5,1.5]);
%        title('perfect MMF')
%
    pause(0.1);

    if t == 0.001

        break
%
    end
end
% % %
% xlswrite('1.xlsx',H_t1(1,:))
```

2. Current sheet construction script (.vbs)

'this script is designed to draw n coils in the air gap to form a current sheet with current flowing in each coil along axial direction. This script is editing from the work of Sichao Yang.

'only coils are made, no waveform of the current input is defined

```
Call getDocument().setDefaultLengthUnit("Millimeters")

steps = 360

seg = 1

model_deg = 360 / seg

pi = 3.14159265358979
  'INPUTS
'***********************************************************

cond = "Name=Copper: 100% IACS"

StackLength = 161

'these two combined define the size of the coil
outerR = 52.95          'the radius of the original stator
innerR = outerR-1
ag = 0.25               'air gap
'***********************************************************

if model_deg = 360 then

    Call getDocument().getView().newCircle(0, 0, outerR)

    Call getDocument().getView().newCircle(0, 0, innerR-0.25*ag)

    Call getDocument().getView().selectAt((outerR+innerR)/2, 0, infoSetSelection, Array(infoSliceSurface))

    REDIM ArrayOfValues(0)
```

ArrayOfValues(0)= "SA"

Call getDocument().getView().makeComponentInALine(StackLength, ArrayOfValues, "Name=Virtual Air", infoMakeComponentUnionSurfaces Or infoMakeComponentRemoveVertices)

REDIM ArrayOfValues(1)

ArrayOfValues(0)= "SA,Face#3"

ArrayOfValues(1)= "SA,Face#4"

Call getDocument().createBoundaryCondition(ArrayOfValues, "BoundaryCondition#1")

Call getDocument().setMagneticFieldNormal("BoundaryCondition#1")

end if

'***

Call getDocument().setParameter("", "outerR", outerR, infoNumberParameter)

Call getDocument().setParameter("", "innerR", innerR, infoNumberParameter)

Call getDocument().setParameter("", "steps", steps, infoNumberParameter)

Call getDocument().setParameter("", "MeshAllowUnconstrainedHoles", "Yes", infoStringParameter)

'***

'start drawing

Call getDocument().getView().newCircle(0, 0, innerR)

Call getDocument().getView().newCircle(0, 0, outerR)

Call getDocument().getView().newLine(0,0, outerR,0)

Call getDocument().getView().SelectAll(infoSetSelection, Array(infoSliceLine, infoSliceArc))

For T = 1 To steps

Call getDocument().getView().newLine(0, 0, (outerR + 2) * Cos(model_deg / steps * T / 180 * pi), (outerR + 2) * Sin(model_deg/ steps * T / 180 * pi))

Call getDocument().getView().selectAt((outerR + innerR) / 2 * Cos(model_deg / steps * T / 180 * pi - model_deg / steps / 180 * pi / 2), (outerR + innerR) / 2 * Sin(model_deg / steps * T / 180 * pi - model_deg / steps / 180 * pi / 2), infoSetSelection, Array(infoSliceSurface))

ReDim ArrayOfValues(0)

ArrayOfValues(0) = "slot" & T

Call getDocument().getView().makeComponentInALine(StackLength, ArrayOfValues, cond, infoMakeComponentUnionSurfaces Or infoMakeComponentRemoveVertices)

Call getDocument().getView().selectObject("slot" & T, infoSetSelection)

ReDim ArrayOfValues(0)

ArrayOfValues(0) = "slot" & T

Call getDocument().makeSimpleCoil(1, ArrayOfValues)

Next

'Deletes all construction lines on slice

Call getDocument().getView().SelectAll(infoSetSelection, Array(infoSliceLine, infoSliceArc))

Call getDocument().getView().deleteSelection

Call getDocument().getView().viewAll()

3. The current sheet model current distribution script (.vbs)

This script is editing from the work of Sichao Yang.

```
Sub main()


   Dim x As Integer


   If Cells(22, 5) = 1 Then

      Call PWL

   ElseIf Cells(22, 5) = 0 Then

      Call DC

   End If

   x = Cells(25, 5)

   Cells(25, 5) = x + 1


End Sub


Sub PWL()


   Dim Nm, pp, time_steps, frac, seg

   Dim fm, pi As Double

   Dim current(100), angle(100), dir(100)

   Dim g, m, n, Row, Column, Column_I, coil_max, model_deg, j As Integer

   Set MagNet = CreateObject("MagNet.Application")

   Set Con = MagNet.getConstants
```

Appendix

```
filepath = Cells(1, 1)

Call MagNet.openDocument(filepath)

'initial setup

MagNet.Visible = True

Application.DisplayAlerts = False

Row = 2        'the row before the value start

model_deg = 360

j = Range("E2")          'the total number of harmonics that needs to be summarised

coil_max = Range("E4")     'number of coils in airgap

Column_I = Range("E6")     'column to record current input

seg = Range("E8")

pp = Range("E14") / 2

time_steps = Range("E18")

frac = Range("E29")

For n = 1 To j

    current(n) = Cells((Row + n), Column_I)

    angle(n) = Cells((Row + n), Column_I + 1)

    dir(n) = Cells((Row + n), Column_I + 2)

Next

Call MagNet.getDocument().getParameter("", "Mech_rpm", Nm)

Call     MagNet.getDocument().setParameter("",     "PolePairs",     pp     *     seg,
Con.infoNumberParameter)

Call MagNet.getDocument().setParameter("", "TimeSteps", "[0,1/%f_e/" & time_steps & ",
1/%f_e/" & frac & "]", Con.infoArrayParameter)

fm = Nm / 60
```

Appendix

pi = 3.14159265358979

Dim coil, l As Integer

Dim t As Double

Dim x As String

Dim y As Integer

y = time_steps * 2 / frac + 1 'the total number of current data points needs to be injected into the coil

For coil = 1 To coil_max

  ReDim ArrayOfValues(y)

  l = 0

  x = "["

  t = 0

  For k = 0 To time_steps / frac

    ArrayOfValues(l) = t

    x = x & ArrayOfValues(l) & ","

    'the l here is the counter for the time value stored and the current value stored

    l = l + 1

    'n is the counter for the harmonic

    n = 1

    ArrayOfValues(l) = 0

    'this for loop can be modified to show single harmonic, show loss without certain harmonics or show loss within a range of harmonics

    Do While n <= j

```
        ArrayOfValues(l) = ArrayOfValues(l) + current(n) * Sin((fm * pp * seg) * 2 * pi * t
* dir(n) + ((coil - 1) / coil_max) * model_deg / 180 * pi * 0.5 * n + angle(n) / 180 * pi)

        n = n + 1

    Loop

    '-----------------------------------------------------------------------

    'flip the air-gap stator MMF waveform over

    ArrayOfValues(l) = -ArrayOfValues(l)

    If l < y Then

      x = x & ArrayOfValues(l) & ","

    Else

      x = x & ArrayOfValues(l) & "]"

    End If

    l = l + 1

    t = t + (1 / (pp * fm * seg) / time_steps)

  Next

  Call  MagNet.getDocument().setParameter("Coil#"  &  coil,  "WaveFormType",  "PWL",
Con.infoStringParameter)

  Call   MagNet.getDocument().setParameter("Coil#"   &   coil,   "WaveFormValues",   x,
Con.infoArrayParameter)

  Next


'For t = 2 To 8

'   Call MagNet.getDocument().disableComponent("p" & t * 2, True)

'Next

'   Call MagNet.getDocument().disableComponent("p" & pp * 2, False)

  'Call MagNet.getDocument().solveTransient2dWithMotion
```

Rem   If (CInt(j) Mod 3) <> 1 Then

Rem   j = j + 2

Rem   Else

Rem   j = j + 1

Rem   End If

Rem loop

End Sub

Sub DC()

   Dim Nm, pp, time_steps

   Dim fm, pi As Double

   Dim current(100), angle(100), dir(100)

   Dim g, m, n, Row, Column, Column_I, coil_max, model_deg, j, seg As Integer

   Set MagNet = CreateObject("MagNet.Application")

   Set Con = MagNet.getConstants

   filepath = Cells(1, 1)

   Call MagNet.openDocument(filepath)

   'initial setup

   MagNet.Visible = True

   Application.DisplayAlerts = False

   Row = 2   'the row before the value start

   model_deg = 360

Appendix

```
j = Range("E2")          'the total number of harmonics that needs to be summarised

coil_max = Range("E4")     'number of coils in airgap

Column_I = Range("E6")     'column to record current input

seg = Range("E8")

pp = Range("E14") / 2

time_steps = Range("E18")

For n = 1 To j

    current(n) = Cells((Row + n), Column_I)

    angle(n) = Cells((Row + n), Column_I + 1)

    dir(n) = Cells((Row + n), Column_I + 2)

Next

Call MagNet.getDocument().getParameter("", "Mech_rpm", Nm)

Call     MagNet.getDocument().setParameter("",     "PolePairs",     pp     *     seg,
Con.infoNumberParameter)

Call     MagNet.getDocument().setParameter("",     "TimeSteps",     "[0,1/%frequency/"     &
time_steps & ", 1/%frequency/1]", Con.infoArrayParameter)

fm = Nm / 60

pi = 3.14159265358979



Dim coil As Integer

Dim x, t As Double

t = Range("E31") / 1000

For coil = 1 To coil_max

'n is the counter for the harmonic
```

n = 1

x = 0

'this for loop can be modified to show single harmonic, show loss without certain harmonics or show loss within a range of harmonics

Do While n <= j

x = x + current(n) * Sin((fm * pp * seg) * 2 * pi * t * dir(n) + ((coil - 1) / coil_max) * model_deg / 180 * pi * n + angle(n) / 180 * pi)

n = n + 1

Loop

'--

'flip the air-gap stator MMF waveform over

x = -x

Call MagNet.getDocument().setParameter("Coil#" & coil, "WaveFormType", "ACDC", Con.infoStringParameter)

Call MagNet.getDocument().setParameter("Coil#" & coil, "Current", x, Con.infoNumberParameter)

Call getDocument().setParameter("Coil#" & coil, "CurrentPhase", "0%deg", infoNumberParameter)

Next

End Sub